

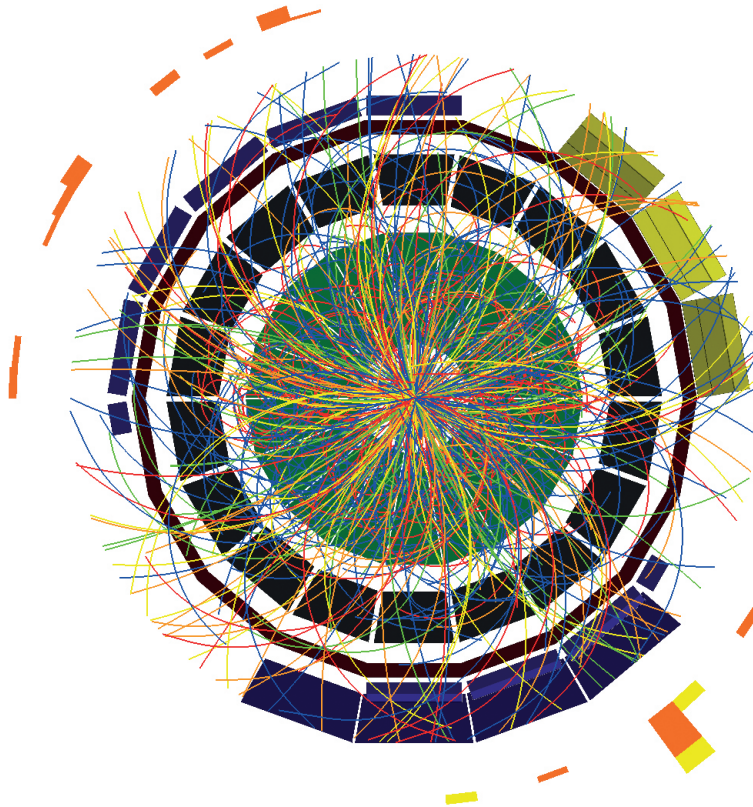
JYU DISSERTATIONS 666

---

Oskari Saarimäki

**Dijet invariant mass spectrum  
in pp and p-Pb collisions  
at  $\sqrt{s_{NN}}=5.02$  TeV**

---



UNIVERSITY OF JYVÄSKYLÄ  
FACULTY OF MATHEMATICS  
AND SCIENCE

JYU DISSERTATIONS 666

---

Oskari Saarimäki

**Dijet invariant mass spectrum  
in pp and p-Pb collisions  
at  $\sqrt{s_{NN}}=5.02$  TeV**

Esitetään Jyväskylän yliopiston matemaattis-luonnontieteellisen tiedekunnan suostumuksella  
julkisesti tarkastettavaksi yliopiston Ylistönrinteen salissa FYS1  
kesäkuun 27. päivänä 2023 kello 12.

Academic dissertation to be publicly discussed, by permission of  
the Faculty of Mathematics and Science of the University of Jyväskylä,  
in Ylistönrinne, auditorium FYS1, on June 27, 2023 at 12 o'clock noon.



JYVÄSKYLÄN YLIOPISTO  
UNIVERSITY OF JYVÄSKYLÄ

JYVÄSKYLÄ 2023

Editors

Ilari Maasilta

Department of Physics, University of Jyväskylä

Ville Korkiakangas

Open Science Centre, University of Jyväskylä

Cover image: Proton-lead collision at 5.02 TeV as seen by ALICE © 2016 CERN,  
for the benefit of the ALICE Collaboration.

Reprinted with permission from CERN.

Copyright © 2023, by author and University of Jyväskylä

ISBN 978-951-39-9662-8 (PDF)

URN:ISBN:978-951-39-9662-8

ISSN 2489-9003

Permanent link to this publication: <http://urn.fi/URN:ISBN:978-951-39-9662-8>

# ABSTRACT

Saarimäki, Oskari

Dijet invariant mass spectrum in pp and p–Pb collisions at  $\sqrt{s_{\text{NN}}} = 5.02$  TeV

In this thesis, I present the dijet invariant mass analysis in proton–proton and proton–lead collisions at the center-of-mass energy per nucleon of 5.02 TeV. The measurement of the data was conducted with the ALICE detector, which is one of the four experiments along the CERN Large Hadron Collider accelerator, which is the largest particle collider in the world.

The dijets were reconstructed from charged tracks in the ALICE central detectors in minimum bias proton–proton (pp) and proton–lead (p–Pb) collisions. I reconstructed the jets using anti- $k_T$  algorithm with radius parameter  $R = 0.4$  implemented by the FastJet [1] package and subtracted the underlying event background with the 4-momentum background subtraction method. A notable new analysis technique I developed for this analysis is the correction of the background fluctuations for the dijet invariant mass spectrum. I unfolded the measured distributions for background fluctuations together with the detector response in a similar way as in earlier jet  $p_T$  cross section measurements.

I determined the nuclear modification factor  $R_{pA}$  from the dijet invariant mass cross sections in proton–proton and proton–lead collisions. The final statistical and systematic uncertainties remained at 10–20%. The  $R_{pA}$  is compatible with no modifications from the cold nuclear matter effects within the uncertainties. This is the first measurement of the dijet invariant mass involving a heavy ion environment. I used Pythia and POWHEG+Pythia MC event generators to calculate the dijet invariant mass with nuclear parton distribution functions (nPDF), which show a slight enhancement in  $R_{pA}$ . According to nPDFs sets of EPPS21 [2], the hard parton momentum fraction distributions of the dijet events could be attributed to the anti-shadowing domain, which is  $x \sim 0.01$ – $0.1$  for gluons. However, the final uncertainties in the measurement are too large to make definite conclusions.

**Keywords:** jet, dijet, invariant mass, heavy ion, p–Pb, ALICE, CERN, LHC

## TIIVISTELMÄ (ABSTRACT IN FINNISH)

Tässä väitöskirjassa esittelen dijettien invariantin massan spektrin analyysin protoni–protoni ja protoni–lyijy törmäyksissä massakeskipiste-energialla 5.02 TeV. Analysoin työssäni ALICE-kokeen mittaamaa dataa, joka on yksi neljästä koeasemasta CERN:n suuren hadronitörmäytin (LHC, Large Hadron Collider) varrella. LHC on tällä hetkellä maailman suurin hiukkastörmäytin.

Dijetit rekonstruoiitiin mittaamalla varattuja hiukkasjälkiä ALICE-kokeen keskiosan ilmaisimissa protoni–protoni (pp) ja protoni–lyijy (p–Pb) törmäyksissä. Törmäykset valittiin mahdollisimman vähän vinoutuneesti (Minimum Bias collisions) tarkoittaen sitä, että analyysissä pyrittiin valitsemaan mahdollisimman edustava otos epäelastisista sirontatapahtumista. Jetit rekonstruoiitiin käyttämällä FastJet [1] paketin anti- $k_T$  algoritmia sädeparametrilla  $R = 0.4$ , ja jettien tausta poistettiin nelivektorimetodilla. Erityisen suuri panostus tähän analyysiin oli uuden tekniikan kehittäminen taustan flukтуаatioiden korjaamiseksi dijettien invariantin massan spektristä. Tämä korjaus toteutettiin unfolding metodilla samanaikaisesti detektoriefektien korjaamisen kanssa, joka on tyypillinen jettianalyysien tapa toteuttaa korjaus.

Työssäni mittasin dijettien invariantin massan ydinmodifikaatiotekijän  $R_{pA}$  protoni–lyijy törmäyksissä. Lopullinen statistinen ja systemaattinen epävarmuus on noin 10–20%. Epävarmuuksien puitteissa voidaan sanoa, että ydinmodifikaatiota ei tapahdu kylmän ydinaineen efekteistä johtuen. Tämä on ensimmäinen dijettien invariantin massan mittaus, jossa on mukana ydintörmäys. Mittasin dijettien invariantin massan spektrin myös Pythia ja POWHEG+Pythia Monte Carlo -ohjelmistoilla, joissa oli otettu huomioon ydinpartonijakaumat. Simulaatiot näyttivät hienoisien lisäprotoni–lyijy spektrissä verrattuna protoni–protoni spektriin. EPPS21 [2] ydinpartonijakaumien mukaan kovan vuorovaikutuksen partonien liikemääräosuudet on mahdollista liittää anti-varjostusalueeseen, joka on gluoneille  $x \sim 0.01$ – $0.1$ . Tästä simulaatiolla todetusta efektistä on kuitenkin vaikea tehdä lopullista johtopäätöstä, johtuen mittausten epävarmuuksien suuruudesta.

**Avainsanat:** jetti, dijetti, invariantti massa, raskasioni, p–Pb, ALICE, CERN, LHC

**Author**

Oskari Saarimäki  
University of Jyväskylä  
Jyväskylä, Finland

**Supervisors**

Adjunct Prof. Sami Räsänen  
University of Jyväskylä  
Jyväskylä, Finland

Adjunct Prof. Kim Dong Jo  
University of Jyväskylä  
Jyväskylä, Finland

**Reviewers**

Adjunct Prof. Henning Kirschenmann  
University of Helsinki  
Helsinki, Finland

Professor Olga Evdokimov  
University of Illinois  
Chicago, USA

**Opponent**

Associate Prof. Dennis Perepelitsa  
University of Colorado  
Boulder, USA

## ACKNOWLEDGEMENTS

This book has been a tremendous undertaking that could not have been possible without the support of a great many people and organizations. First, I want to thank Dr. Henning Kirschenmann and Prof. Olga Evdokimov for reviewing this book and Dr. Dennis Perepelitsa for agreeing to travel here and be my opponent during the defense. Jyväskylä is a faraway place.

During the whole Ph.D. process (and before that), my supervisor Sami Räsänen has been the pillar of stability and a source of inspiration for me. The weekly meetings kept the wheels rolling, even when I had a hard time. I also want to thank Kim Dong Jo, who has taught a big chunk of analysis techniques, programming, general research and life philosophy over the years, for which I am really grateful. The ALICE group in Jyväskylä and worldwide has been an amazing community where I have felt welcomed. Out of our group, I have to give a special mention to Adrian, who has always invited me everywhere whenever we have been in the same place and generally has been a great friend I am happy to have.

From our group, I want to specifically thank Heidi Rytönen, who started her Ph.D. studies and defended her Ph.D. around the same time as I did. We worked together on the FIT event plane simulation studies, and it was honestly one of the best research experiences I have had during my years at the university. I also want to thank Maciej Slupecki, who chaired the FIT software meetings during our work with FIT and who was always a great help. All in all, I had a wonderful time with the Jyväskylä ALICE group, so I want to thank Andreas, Anna, Cindy, Hadi, Jasper, Laura, Maxim, and Yury. The years would not have been the same without you. I want to extend my special thanks to Hadi Hassan, whom I had many discussions with about jet physics, and he instructed me in the usage of the POWHEG event generator. At the very beginning of my jet studies in ALICE, Tomas Snellman was the first to teach me how to use ALICE software in detail, and I was able to have some preliminary studies done already during my master's. I want to thank you for that. The ALICE jet working group has supported my research throughout the Ph.D., most notably Raymond Ehlers during the last year.

During my studies, I have been supported by many people and groups also outside of the ALICE. As the readers of this book will notice, Pythia has been an essential tool for me, so I'm thankful that I got to discuss the details of the Pythia software and the Pythia-related jet physics with Dr. Ilkka Helenius and Dr. Marius Uthm; thank you! I want also to thank the professors of our particle physics community here in Jyväskylä. Prof. Kari Eskola agreed to be part of my follow-up group during the Ph.D., which ensured that I was on the right track, even if there were bumps in the road. I want to thank Prof. Tuomas Lappi wrote several recommendation letters for me. These letters bore fruit as I received three years of grant from the Magnus Ehrnrooth foundation, for which I am grateful. I also want to thank CSC, where we ran the computationally heavy FIT simula-

tions. Additionally, the whole particle physics community has grown a lot due to the Academy of Finland Center of Excellence in Quark Matter grant, which I am happy for.

I want to give big thanks for the Holvi collaboration, as the coffee discussions and conferences we have had over the years have kept my inspiration and curiosity at high levels every day. I look forward to joining the Holvi collaboration alumni group very soon. Outside of university life, Tanssisali Lutakko and the Jyväskylä live music association have made Jyväskylä a hometown for me, full of friends and great people I am happy to know. Thanks to them, I think I have grown to be a bit better person.

I have been fortunate to have great friends in and out of Jyväskylä, and I want to especially thank Aku, Aku, Erkka, Heikki, Karri, Naru, and Taneli. Thanks to you, our weekly Truuttings, weekly Siege, and all other activities have kept me sane even during the lockdown. Of course, this might never have happened if my family had not been so supportive of my scientific endeavors. My parents have done a great job raising me, and they also subscribed to Aku Ankka and Tieteen Kuvalehti, which made me read all the time. I also want to mention my grandparents, who always have promoted honest work and literature. So I want to thank you for raising me the way you have.

Lastly, but most importantly, my partner Emmi is the most important thing that has happened to me. You have made me believe in myself and pushed me forward whenever necessary. I am so much more whole and happy with you.

In Jyväskylä, June 2023,

*Oskari Saarimäki*



## AUTHOR'S CONTRIBUTION

The author has contributed to the research discussed in this book as follows:

- The dijet invariant mass analysis in pp and p–Pb collisions at  $\sqrt{s_{\text{NN}}} = 5.02$  TeV
  - Implementation of the 4-momentum background subtraction for jets. (Section 5.2).
  - Implementation of the analysis code for the dijet invariant mass study. (Section 6.1).
  - The development and implementation of a new method for calculating the background fluctuations of the dijet invariant mass. (Section 6.4)
  - Unfolding of the detector effects and background fluctuations. (Section 6.6)
  - Validating the dijet analysis by comparing the jet  $p_{\text{T}}$  cross sections in this work to earlier published ALICE results. (Section 6.8)
  - Analysis of systematic sources of uncertainties for the dijet invariant mass. (Section 7.1)
  - Comparing obtained experimental data with results from Pythia and POWHEG+Pythia MC generators for a better understanding of the physics interpretation. (Section 7.2)
- Together with my colleague Heidi Rytönen we worked on a project validating FIT event plane detection capabilities.
  - To gain a better understanding of the physics, we developed a toy MC to validate various collective flow effects. (Section 3.3.3)
  - After validating the methods with the toy MC, we performed a full ALICE FIT detector simulation with heavy ion events from the AMPT MC event generator. We used the simulation to estimate the performance of the new Fast Interaction Trigger detector in the event plane determination. (Section 3.3.5)

# CONTENTS

ABSTRACT

TIIVISTELMÄ (ABSTRACT IN FINNISH)

ACKNOWLEDGEMENTS

AUTHOR'S CONTRIBUTION

CONTENTS

|       |   |    |
|-------|---|----|
| 1     | INTRODUCTION .....  | 11 |
| 2     | THEORETICAL BACKGROUND .....                                      | 21 |
| 2.1   | Cross sections of ultrarelativistic collisions.....               | 21 |
| 2.2   | Collinear factorization.....                                      | 23 |
| 2.3   | Nuclear effects .....   | 26 |
| 2.4   | Modern heavy ion collider experiments.....                        | 27 |
| 2.5   | Monte Carlo event generators.....                                 | 30 |
| 2.5.1 | Pythia.....   | 30 |
| 2.5.2 | POWHEG .....  | 32 |
| 2.5.3 | AMPT .....  | 33 |
| 2.5.4 | GEANT .....   | 33 |
| 3     | A LARGE ION COLLIDER EXPERIMENT: ALICE.....                       | 35 |
| 3.1   | Coordinate system.....  | 35 |
| 3.2   | ALICE detector during LHC Run 2 .....                             | 35 |
| 3.3   | Overview of the ALICE upgrade for LHC Run 3.....                  | 38 |
| 3.3.1 | Fast Interaction Trigger: FIT.....                                | 40 |
| 3.3.2 | Event plane determination .....                                   | 41 |
| 3.3.3 | Flow coefficients.....  | 43 |
| 3.3.4 | Q-vector corrections.....   | 46 |
| 3.3.5 | AMPT MC generator with full FIT detector simulation.....          | 48 |
| 4     | EVENT AND TRACK SELECTION.....                                    | 52 |
| 4.1   | Visible cross section related to ALICE minimum bias trigger ..... | 52 |
| 4.2   | Vertex and track reconstruction.....                              | 53 |
| 4.3   | Vertex reconstruction efficiency.....                             | 57 |
| 5     | JETS.....   | 58 |
| 5.1   | Jet definition .....  | 58 |
| 5.2   | Background subtraction .....                                      | 60 |
| 6     | ANALYSIS.....   | 67 |
| 6.1   | Dijet invariant mass definition .....                             | 67 |
| 6.2   | Dijet invariant mass differential cross section .....             | 71 |
| 6.3   | Nuclear modification factor .....                                 | 71 |
| 6.4   | Underlying event fluctuations .....                               | 72 |

|       |  |     |
|-------|--|-----|
| 6.5   | Detector response .....  | 75  |
| 6.6   | Unfolding procedure .....                                      | 80  |
| 6.6.1 | Bayesian iterative unfolding method .....                      | 82  |
| 6.6.2 | SVD unfolding method .....                                     | 84  |
| 6.7   | Unfolding validation .....                                     | 88  |
| 6.8   | Jet $p_T$ spectrum validation .....                            | 89  |
| 7     | RESULTS.....   | 92  |
| 7.1   | Dijet invariant mass systematic uncertainties .....            | 92  |
| 7.1.1 | Tracking efficiency uncertainty.....                           | 92  |
| 7.1.2 | Unfolding uncertainty.....                                     | 94  |
| 7.1.3 | Total systematic uncertainty .....                             | 97  |
| 7.2   | Dijet invariant mass MC model comparisons .....                | 101 |
| 7.3   | Dijet invariant mass and the nuclear modification factor ..... | 103 |
| 8     | CONCLUSIONS AND OUTLOOK .....                                  | 106 |
|       | APPENDIX A JET $P_T$ ANALYSIS.....                             | 109 |
|       | APPENDIX B RAW DATA TO DETECTOR MC COMPARISONS.....            | 112 |
|       | APPENDIX C LIST OF MONTE CARLO GENERATOR SETTINGS.....         | 115 |
|       | C.1 AMPT settings .....  | 115 |
|       | C.2 Pythia settings.....                                       | 115 |
|       | C.3 POWHEG-BOX settings .....                                  | 115 |
|       | BIBLIOGRAPHY.....  | 118 |

# 1 INTRODUCTION

The Standard Model of particle physics [3] is one of the most successful theories developed so far. Even though this theory is not a complete description of forces as, for example, it lacks gravitation, precision measurements have shown time and time again that we can accurately predict the high-energy collision experiments [4], especially the quantum electrodynamic (QED) interactions [5].

The strong force is approximately two orders of magnitude stronger than the electromagnetic one [6, p.519], and offers more challenges when compared to the QED. The strong force is described with the theory of quantum chromodynamics (QCD), which studies quarks and gluons with color charges (thus “chromo” in the name). The theory of quantum chromodynamics was for the first time shown to hold true at the Stanford Linear Accelerator Center (SLAC) in 1969, where partons inside a nucleon were identified as quarks, and the asymptotic freedom of the strong interaction was confirmed [7, p.7]. Asymptotic freedom means that the strong interaction is weaker at shorter distances. The strength of the theory is represented by the strong coupling constant  $\alpha_s$ . In figure 1.1, the running of the strong coupling constant is shown as a function of the interaction strength, showing a decreasing trend at higher scales  $Q$ , typically thought as momentum exchanges of hard interactions, that is to say, smaller distances of the order  $\sim 1/Q$ . In the limit of small  $\alpha_s$  we are able to perform perturbative QCD (pQCD) calculations in powers of  $\alpha_s$ . The leading order (LO,  $\sim \alpha_s$ ) pQCD calculations can be reasonably straightforward to calculate. However, adding next-to-leading order (NLO,  $\sim \alpha_s^2$ ), next-to-next-to-leading order (NNLO,  $\sim \alpha_s^3$ ), or even higher orders makes the series expansion progressively more complicated. Each order adds tens, hundreds, or even thousands of Feynman diagrams to the calculation. When  $\alpha_s$  grows too large, approximately when  $Q < 1$  GeV [8, p.552], the pQCD methods typically fail, and one has to tackle the problems with other means, like lattice QCD calculations [9, 10]. But even at fairly low  $\alpha_s$ , the NLO corrections can be significant, indicating a slow convergence of the pQCD [11].

The running coupling of the strong interaction, as seen in figure 1.1, will result in color confinement, meaning that one cannot find bare color-charged objects in normal circumstances. A quark or a gluon in a vacuum will quickly

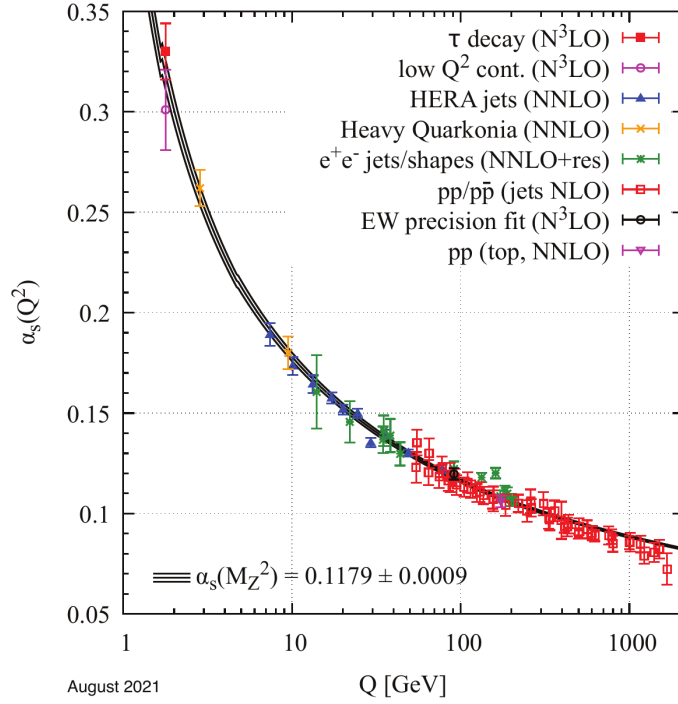
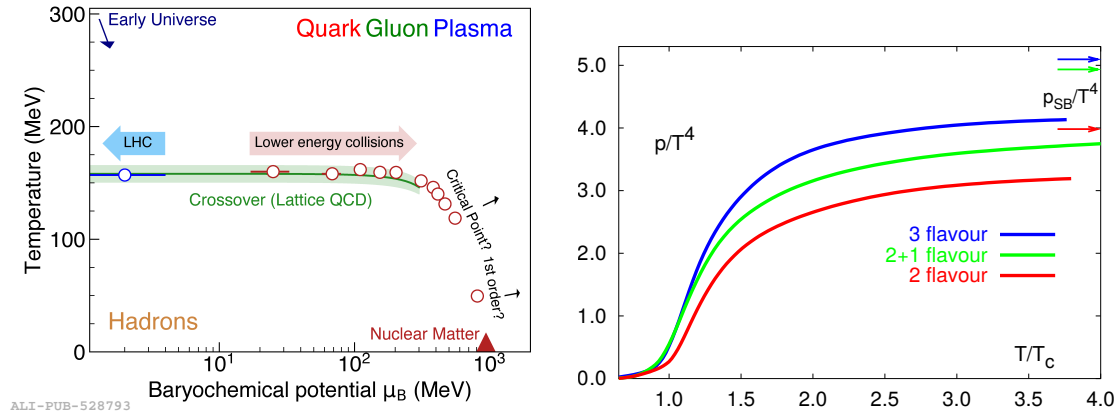


FIGURE 1.1 The strong coupling constant in a function of energy scale  $Q$  as measured by different experiments. Figure from [3, p.551], reprinted under the license CC BY-NC 4.0.

hadronize into color-neutral hadrons. One widely used model of the hadronization process is the Lund string model [19], describing the color fields as strings between colored particles. These strings are used to generate color-neutral particles at the end. However, it turns out that in extreme temperatures and densities, the matter undergoes a phase transition into a new state of matter, quark-gluon plasma (QGP). The environment corresponds to conditions at the early Universe where the temperatures exceeded a critical temperature  $T_c \approx 10^{12}$  K  $\approx$  150–160 MeV [7, 20]. In figure 1.2a, the phase diagram of the nuclear matter is shown. The green band represents the lattice QCD calculations, while the open markers are experimental results. In low temperatures, matter is color neutrally confined in hadrons. With the rising temperature, the hadronic matter has a phase transition to the QGP. The lattice QCD calculations have been used to predict a smooth crossover transition region for matter with low baryochemical potential [7, p.102]. The lattice QCD parametrizes the relation between e.g., pressure and the temperature, especially near the critical temperature, defining the equation of state (EoS) of the quark matter. Below the critical temperature, the lattice QCD EoS is matched to a hadron resonance gas [21]. In figure 1.2b, the pressure over temperature to the fourth is plotted against temperature, showing that pressure has a smooth behavior during the phase transition. The results were calculated with three different quark flavor configurations: two light flavors, three light flavors, or two light flavors and one heavy flavor. Pressure is dependent on the degrees of freedom (dof) of the particle matter [7, p.146], which are different for hadron



(a) The phase diagram of nuclear matter. The green band shows lattice calculation for the transition and the possible transition region where the QGP and hadronic matter exist simultaneously [12]. The open circles are experimental results from various studies [13–16]. Figure from [17], reprinted under the license CC BY 4.0. (b) Pressure over temperature to the fourth as a function of temperature, demonstrating the crossover behavior. The arrows indicate the continuum ideal gas limits. Calculated with a QCD lattice for three different flavor settings. Figure from [18], reprinted with permission from Elsevier.

FIGURE 1.2 Figures demonstrating the QCD phase diagram and the behavior of pressure near the critical temperature.

gas and QGP, thus creating a pressure difference between the two. If the transition would be first order, the derivative  $dP/dT$  would be discontinuous due to the change in dof, which is not seen in figure 1.2b. On higher baryochemical potential, a first-order transition is predicted, and at a critical point between the first-order transition and smooth transition, the transition could be second-order [22]. Astrophysical studies show evidence of quark matter also in low temperatures and large baryochemical potentials [23].

Heavy ion collisions provide a dense zone of matter where studies of the QGP are possible. Several accelerators were upgraded to collide heavy ions to study QGP at various energies and detectors. Detectors that collided ions include the Bevatron coupled with SuperHilac (Bevalac) at LBNL [24], Dubna Synchrotron [25], the Alternating Gradient Synchrotron (AGS) at BNL [26], and the Super Proton Synchrotron (SPS) at CERN [7]. In 2000 it was announced by CERN that there is evidence for the formation of a new state of matter in the heavy ion collisions at SPS [27–30]. Soon to follow, an ion collision dedicated Relativistic Heavy Ion Collider (RHIC) was completed at BNL in 2000 [31] with the AGS as a preaccelerator. Similarly, the CERN SPS is nowadays used as a preaccelerator for the Large Hadron Collider (LHC) [32, 33], which was fitted in the same tunnel as Large Electron–Positron collider [34] in the year 2009. CERN reserves a month each year to collide heavy ions in the LHC.

As ions are spatially sizeable objects, the collision zones differ in geometry. For example, the ions might merely scrape each other in one collision, while another might be a head-on collision. These are not equivalent collisions due to the

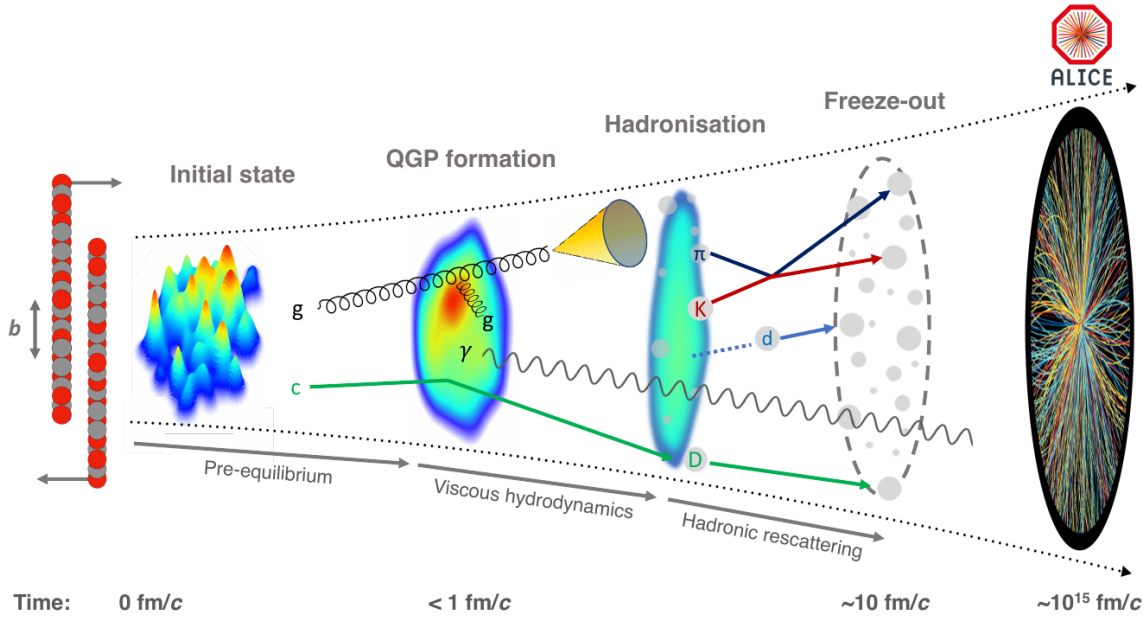


FIGURE 1.3 A visualization of the stages of QGP formation as presented in the ALICE review [17], inspiration taken from the illustrations of Chun Shen, reprinted under the license CC BY 4.0.

number of individual nucleon–nucleon collisions being very different. The heavy ion collisions can be categorized into different centrality classes by comparing the number of particles produced in the events [35–38]. A central collision, where the ions collide head-on with each other, has more nucleons interacting, thus generating more particles, i.e., higher multiplicities. Another method would be to measure the nucleons not participating in the collision with a zero-degree calorimeter [35]. The exact method for determining the centrality of a collision depends on the experiment and the physics analysis.

Central heavy ion collisions are a great way to create QGP experimentally, as the collision zone is large. The higher center-of-mass energy we can achieve in the collision, the better chance we have to detect the QGP as we need to achieve the critical temperature of the phase diagram in figure 1.2a. Coincidentally the higher colliding energy we have, the more baryochemically neutral the outcome will be in the central rapidities. This is because at lower energies, the ions have a brief time to slow down and thus have a bigger chance of reaching the mid-rapidity area [39, p.115]. On higher energies, the nucleons are so ultrarelativistic that everything that did not interact strongly during the collision travels straight into the beam pipe, only to be seen by very forward detectors like the ALICE experiment zero degree calorimeters [39, p.115] for example.

The QGP formation in heavy ion collisions is a multi-stage process with different observables and theoretical fields of particle physics studying different stages. The stages are separated into four steps in figure 1.3, which are read chronologically from left to right. The leftmost part of the figure shows the ions extremely length contracted in the laboratory frame, and the rightmost part of the figure shows the measured tracks by the experiment. Experimentally we only see

the measured final state particles, so everything from the initial state of the collision until the hadronic freeze-out requires strong interplay between theoretical models and experiments [17].

Starting from the earliest moments, the initial state of the heavy ion collision can be modeled via many methods. Monte Carlo Glauber [40] is the most common way to calculate the initial distribution of the nucleons in the ions. In the MC Glauber, one simulates spatial positions of individual nucleons most often based on the Woods-Saxon nuclear density distribution [41]. After sampling both of the ions, the simplest way to decide if individual nucleons collide is that if their distance in transverse plane  $d \leq \sqrt{\sigma_{\text{inel}}^{\text{NN}}/\pi}$  which is called the black-disk overlap function. From this information, a straightforward description of the initial state can be obtained by calculating the energy density of each individual nucleon–nucleon collision and summing them considering the transverse positions of said collisions. This is a simplified explanation of how the T<sub>R</sub>ENTo model generates initial states [42]. There are many other models for describing the initial state, like, for example IP-Glasma [43] or the EKRT [44, 45] models.

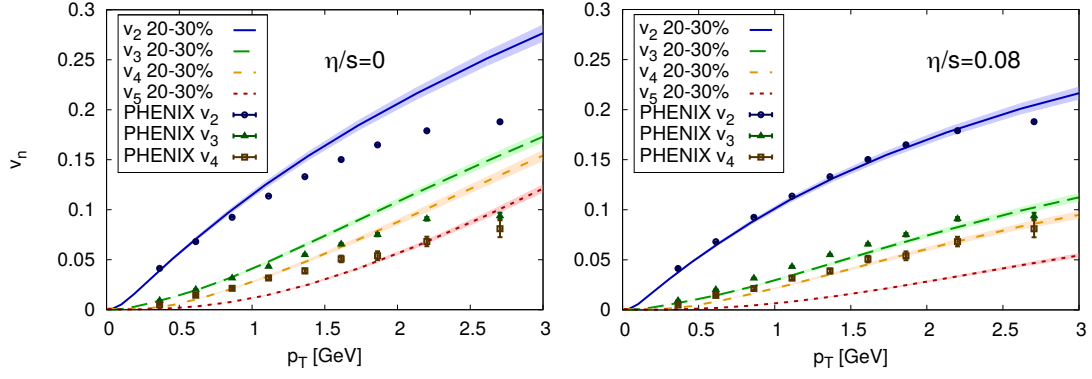
The bulk of the particle production is from soft nucleon–nucleon interactions. These softer interactions form the pre-equilibrated parton gas. Within a  $1 \text{ fm}/c \approx 3 \times 10^{-24} \text{ s}$ , the QGP forms from thermalized partons and expands as the parton gas is equilibrated, and the collective behavior of the soft particle production is generated [46, 47]. Approximately within  $10 \text{ fm}/c$ , the QGP matter cools down while expanding, and the partonic matter hadronizes [48]. Briefly during the hadronization and after the chemical freeze-out of hadrons, the hadrons interact with each other as well in a hadron gas phase, which will last until the kinetic freeze-out, after which the hadrons are physically so far from each other that the interactions between them do not matter anymore, and they stream freely out of the collision into the detectors around<sup>1</sup> [17].

Due to fluctuations and collision geometry, the thermalized QGP droplet has anisotropic pressure gradients, which induct a collective behavior for the particles which are seen in the detector. By studying this collective behavior, we can try to estimate the properties of the QGP, like viscosity. Viscosity is a property of matter which describes how much the matter resists deformations, and even the QGP has viscosity [49]. The higher viscosity a matter has, the bigger resistance to changes in the shape of the matter. For example, water has a smaller viscosity than honey, which means water flows more freely. Commonly the ideality of a fluid is measured by the viscosity over entropy density ratio  $\eta/s$ . The theoretical limit for this  $\eta/s$  ratio has been calculated universally to be at minimum  $1/4\pi$  [50], and there is theoretical evidence suggesting a minimum for the quark matter  $\eta/s(T)$  around the phase transition temperature from hadron gas to QGP [51]. As the viscosity affects how well the matter flows, the strength of flow has been captured in the flow coefficients, which characterize the azimuthal anisotropy of particle production. The collective behavior is commonly described as a Fourier series of cosine terms, where the flow coefficients are the amplitudes of each co-

---

<sup>1</sup> Short lived resonances decay to particles that are stable within the flight time to detectors.





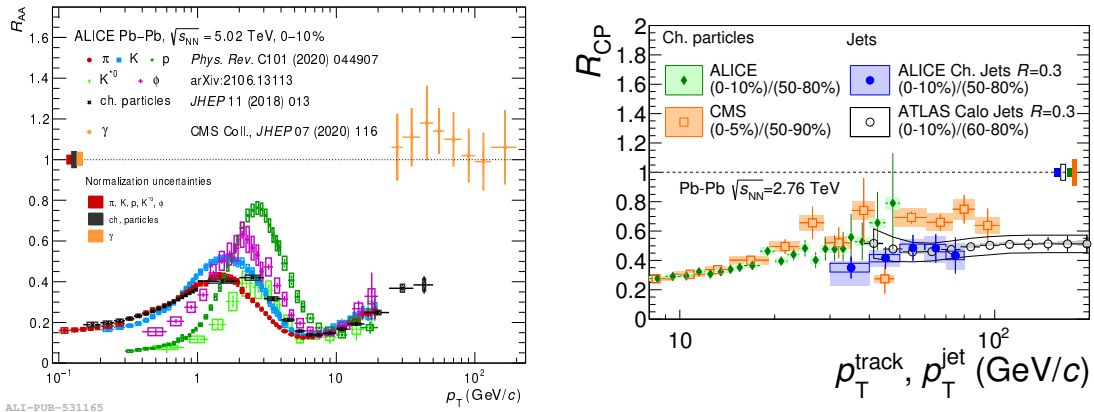
(a) Calculations for the ideal flow with no viscosity. (b) Calculations with small viscosity of  $\eta/s = 0.08$ .

FIGURE 1.4 The flow coefficients  $v_2$ ,  $v_3$ ,  $v_4$ , and  $v_5$  in gold–gold collisions at  $\sqrt{s_{\text{NN}}} = 200$  GeV as measured by PHENIX [53], and modeled by [52]. Reprinted figure with permission from [52], copyright (2023) by the American Physical Society.

sine term [46]. The higher-order coefficients describe the finer anisotropies of the event. Figure 1.4 shows two hydrodynamic simulations and the resulting flow coefficients of orders 2 to 5 are shown [52]. The left-hand side uses an ideal hydrodynamic evolution without any viscosity, and the right-hand side has a modest viscous effect with  $\eta/s = 0.08$ , which is close to the ideal value of  $1/4\pi$ . This shows how viscosity dampens the flow coefficients, especially for higher-order flow coefficients. By comparing the models to measurements by PHENIX [52], one can conclude that the viscosity should not be much smaller or much higher than 0.08. Recently there have been studies where the temperature dependency of  $\eta/s$  has been studied with a parametrized form of  $\eta/s$ , which has a temperature dependency [45].

The largest energy-momentum transfers are the first interactions in a collision. Due to the time–energy uncertainty relation, one can argue that reactions with the highest energy transfer, in colliders measured by transverse momentum  $p_T$ , happen first at  $\sim 1/p_T$  [17, p.90]. The high-energy partons traverse through the whole evolution of the collision and, given a high enough energy, do not thermalize. The energy of the partons is partially lost to the medium in the process [59–66]. High-energy partons then fragment and form well-collimated showers of particles called jets. This is signified in figure 1.3 as a yellow cone representing the spread of particles in the jet. As the hard interactions happen in the very early stages of the heavy ion collision, the medium modifications of the parton have been studied to be dominated by two effects: modification of vacuum radiation in the early times of the collision and medium-induced radiation in the later time [67]. In addition, the parton will excite the particles of the thermalized medium, creating a so-called backreaction of the medium. The backreaction has also been noticed to be an important aspect of jet modification [68, 69].

Studying jet modification experimentally can be conducted, for example,



(a) ALICE measured charged hadron  $R_{AA}$  for central Pb–Pb collisions for identified particles [17, 54–56] Also included is the CMS isolated photon  $R_{AA}$  for comparison [57]. Figure from [17], reprinted under the license CC BY 4.0.

(b) A combined figure of Pb–Pb collision nuclear modification factor  $R_{CP}$ , which compares central results to peripheral results, measured by ALICE. Figure from [58], reprinted under the license CC BY 4.0.

FIGURE 1.5 Various nuclear modification factor measurements.

with 2-particle correlations [73, 74], or with the use of jet reconstruction algorithms [1], and this thesis concentrates on the latter. High-energy hadrons or reconstructed jets can be used to measure nuclear modification factor  $R_{AA}$ , which describes the strength of the nuclear effects. The nuclear modification factor can be written as

$$R_{AA} = \frac{\text{AA yield}}{\text{pp yield} \times \text{binary collisions}}, \quad (1.1)$$

where the binary collisions refer to the average number of individual nucleon–nucleon collisions in a single heavy ion collision. No nuclear effects, i.e.,  $R_{AA} = 1$ , thus refers to a situation where the heavy ion collision would be equal to a collection of individual proton–proton collisions. Figure 1.5a shows a collection of nuclear modification factor measurements for hadrons and direct photons. From the figures, one can see how the  $R_{AA} < 1$  for all hadrons, meaning that the production of hadrons is suppressed in the heavy ion collisions. This suppression is attributed to the jet quenching effect, where the high-energy partons lose energy to the medium. On the other hand, for direct photons, the  $R_{AA} = 1$  is within the experimental uncertainties. Photons do not interact strongly so the mean free path of the photons in QGP is much higher, of the order of 500 fm [75]. As such, they escape the QGP mostly without interacting. This observation confirms that the normalization of the  $R_{AA}$  is correct <sup>2</sup>.

The nuclear modification factor can also be calculated by comparing central heavy ion collisions to peripheral collisions, labeled as  $R_{CP}$ , and normalizing each centrality class accordingly [58]. The collision zone in central collisions is larger and thus will have a more significant jet quenching effect. In figure 1.5b, the

<sup>2</sup> As the nucleus is composed of both protons and neutrons, direct photon production is affected by the isospin effects, which are small [57].

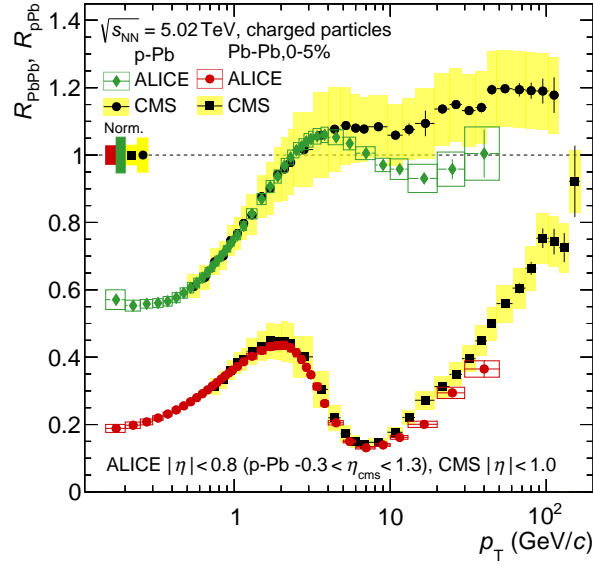


FIGURE 1.6 A comparison of nuclear modification factor between p–Pb and Pb–Pb collisions for charged hadrons, as measured by ALICE [70], and CMS [71, 72]. Figure from [70], reprinted under the license CC BY 4.0.

central-to-peripheral modification factor is shown for charged particles and jets in a wide transverse momentum range, showing a clear suppression for both. Comparing hadron  $R_{CP}$  to jet  $R_{CP}$  is not straightforward, as jets are a sum of many hadrons. One could expect a smaller suppression for jets as some of the medium-induced radiation could be recovered inside the jet cone, but as the comparison is not meaningful, a definite conclusion cannot be made without a mapping of the hadron population to that of jets [17].

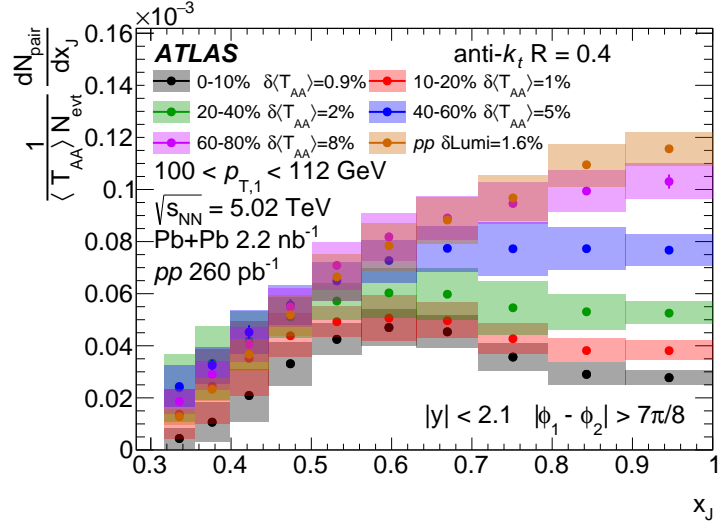
Besides the Pb–Pb collision, LHC has collided also p–Pb and Xe–Xe [71, 76–83] collision systems. Relatively recently, it has been found that the highest activity p–Pb collisions and even pp collisions have shown signals of QGP like the double ridge structure in two-particle correlation studies [84–86]. Even such, the jets have not shown modification in small systems [17]. Minimum bias p–Pb collisions are thought to happen without the formation of the QGP, as there are either very small or nonexistent signals usually associated with the formation of QGP. On the other hand, the system does have an ion, which might affect the results due to the so-called cold nuclear matter (CNM) effects, thus p–Pb is an interesting collision system for reference. Bound nucleons have a modified nuclear parton distribution function that incorporates effects that are not present in a free proton [2, 87, 88], such as gluon shadowing and anti-shadowing [89, 90]. The nuclear modification factor of charged hadrons for central Pb–Pb and MB p–Pb is shown in figure 1.6, including measurements from ALICE [70] and CMS [71, 72]. It shows how the p–Pb does not show significant modification for hadrons with transverse momentum over 2 GeV. Other similar studies can be found in [70–72, 91].

Because of momentum conservation, high-energy jets are most of the time born with a paired jet which is roughly back-to-back in the transverse plane to the first one. The two-jet system is called a dijet, and dijets have been used in ultrarelativistic collisions to search for very high mass resonances [92, 93], but also to act as a way to quantify jet suppression [94–96]. In heavy ion collisions, the jets have a surface bias [97], which means that there is a higher chance of absorption for jets that are born near the center of the collision zone than near the surface [98]. In figure 1.7, a momentum imbalance of the subleading to leading jet has been measured in many centrality classes. The more central the collision is, the bigger suppression is seen. In the left figure, the leading jet has a transverse momentum of  $100 < p_{T,1} < 112$  GeV and on the right  $398 < p_{T,1} < 562$  GeV. The results show that the imbalance is more pronounced for lower leading  $p_T$ .

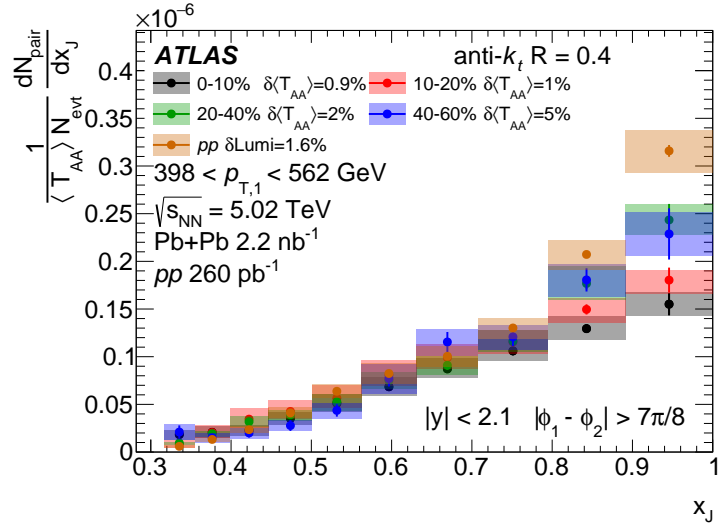
A dijet can be written as the sum of the 4-momenta of the two jets, and this object has an invariant mass of  $M_{jj}$ . Ideally, this represents the outgoing partons of the hard interaction, and because of the momentum conservation, the square of the mass is the partonic center-of-mass energy  $\hat{s}$ . Using this information, I can write  $\hat{s} = x_1 x_2 s_{NN} = M_{jj}^2 \approx 4p_T^2$ , where the  $x_1$  and  $x_2$  are the momentum fractions carried by the interacting partons,  $\sqrt{s_{NN}}$  is the center-of-mass energy per nucleon pair of the collision, and where the approximation holds for massless azimuthally back-to-back jets with  $\Delta\eta = 0$  between them. Rearranging the equation gives

$$\sqrt{x_1 x_2} = \frac{M_{jj}}{\sqrt{s_{NN}}}, \quad (1.2)$$

which shows that the dijet invariant mass is a tool to probe the earliest moments in the collision as the hardest interaction happens the first. This thesis aims to establish the analysis framework and the tools needed to measure dijet invariant mass in the pp and p–Pb collisions and lay the groundwork for future dijet invariant mass analysis.



(a) The imbalance when the leading jet has a transverse momentum of  $100 < p_{T,1} < 112$  GeV.



(b) The imbalance when the leading jet has a transverse momentum of  $398 < p_{T,1} < 562$  GeV.

FIGURE 1.7 The transverse momentum imbalance between the leading and subleading jets is presented in two leading jet  $p_{T,1}$  ranges by ATLAS. Figures from [96], reprinted under the license CC BY 4.0.

## 2 THEORETICAL BACKGROUND

This chapter outlines the basic framework of what the analysis in this thesis is based on, with a focus on jet physics, heavy ion experiments, and Monte Carlo generators. To understand the main result of this thesis, the differential cross section of the dijet invariant mass, I will start by explaining theoretical cross sections related to jets and ultrarelativistic collisions in general.

### 2.1 Cross sections of ultrarelativistic collisions

The total interaction cross section can be written as [99, 100]

$$\sigma^{\text{total}} = \sigma^{\text{elas}} + \sigma^{\text{inel}} \quad (2.1)$$

$$= \sigma^{\text{elas}} + \sigma^{\text{single diff}} + \sigma^{\text{double diff}} + \sigma^{\text{central diff}} + \sigma^{\text{non-diff}}, \quad (2.2)$$

where  $\sigma^{\text{elas}}$  is the elastic collision cross section of the incoming hadrons, where the initial and final state of the interaction is the same. The inelastic cross section  $\sigma^{\text{inel}}$  includes everything else. The inelastic cross section is further divided into single diffractive, doubly diffractive, central diffractive, and non-diffractive portions. Diffractive events have no color exchange between the colliding nuclei. Instead, the force in diffractive events is carried by an exchange of a pomeron, which is a color-neutral object. In the simplest form, this can be understood as a double gluon exchange. The contributions to the total cross section are visualized in figure 2.1, where each class is schematically drawn. Here one can see how each diffractive and elastic interaction is drawn with double gluons, while the non-diffractive interaction has only a single gluon, indicating a net color exchange. In the figure, the  $X$  represents any number of particles the interaction produces. The position of the  $X$  and the red bar indicates the rapidity where the new particles are produced,  $A$  and  $B$  being the beams, and the center point between the  $A$  and  $B$  being the middle-rapidity. For example, a double diffractive event would have particles produced in forward and backward regions of rapidity but also an identifiable gap somewhere in the mid-rapidity region. The central diffractive, on

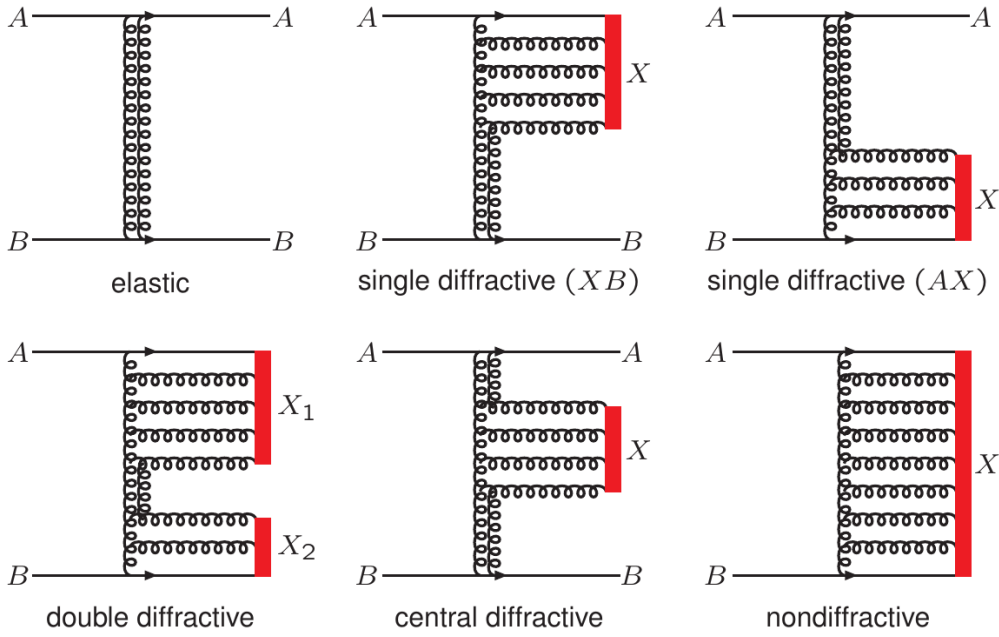


FIGURE 2.1 Visualization of different types of collisions, as imaged in the Pythia comprehensive manual [100], reprinted under the license CC BY 4.0. The double gluon lines mark a color-neutral pomeron exchange, A and B represent the interacting particles, and X can be any number of outgoing particles. The location of the red line indicates the rapidity of the outgoing particles.

the other hand, is the other way around, having a production of particles in the middle of the detector while the projectiles are not destroyed by the interaction in large rapidities.

Diffractive events are classified experimentally by observing gaps in the produced particle rapidity spectrum [101]. ALICE has used Pythia6 [102] and PHOJET [103] MC event generators tuned specifically to match the rapidity gaps and rapidity distributions of measured data to reflect the realistic spread of output particles of the collision. The matching minimum bias trigger is emulated in MC collisions which yields a visible cross section for the ALICE detector. In addition, the inelastic cross section of the MC run is also calculated during the simulation. By comparing these cross sections, trigger efficiency can be calculated. For the ALICE detector, there are several different minimum bias triggers, which have an approximate trigger efficiency of 80%. This will be covered in more detail in section 4.1

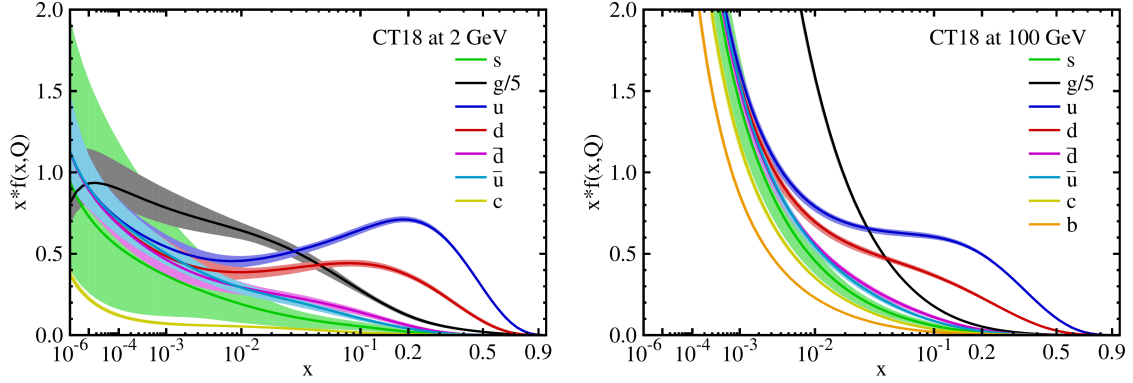


FIGURE 2.2 Parton distribution functions from the CTEQ-TEA collaboration NLO PDF CT18 set. The left figure is calculated at  $Q = 2$  GeV and the left figure at  $Q = 100$  GeV. The legend refers to different quark flavors up, down, strange, and charm. The up and down have separated antiquark components because up and down valence quarks behave distinctly. Figure from [104], reprinted under the license CC BY 4.0.

## 2.2 Collinear factorization

Using the collinear factorization, the inclusive cross section for producing a hadron  $h$  can be written as


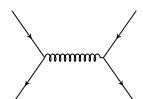
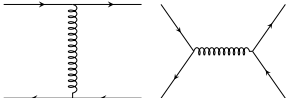
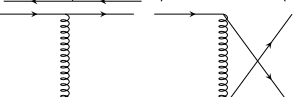
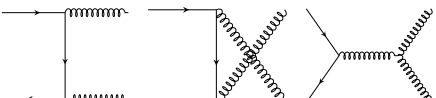
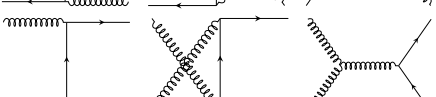
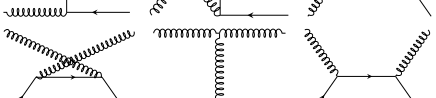
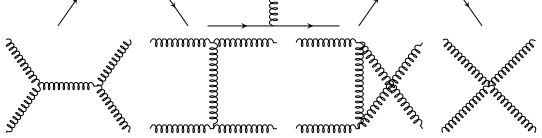
$$\begin{aligned}
 d\sigma_{pp \rightarrow hX} \approx \sum_{a,b,c} \iiint dx_1 dx_2 dz f_a(x_1, Q^2) \otimes f_b(x_2, Q^2) \\
 \otimes d\hat{\sigma}_{ab \rightarrow cX}(x_1, x_2, Q^2) \\
 \otimes D_{c \rightarrow hX}(z_c), \quad (2.3)
 \end{aligned}$$

where the production has been separated into three parts [11, 105].  $f_a(x, Q^2)$  are the parton distribution functions (PDF) for finding a partonic flavor  $a$  inside the proton at the energy transfer of  $Q^2$  where the parton has a fraction of the momentum  $x = p_{\text{proton}}/p_{\text{parton}}$ . There are two PDFs in the equation, one for each projectile. Then we have the perturbative cross section  $d\hat{\sigma}_{ab \rightarrow cX}$  where the parton flavors  $a$  and  $b$  produce a parton flavor  $c$ , and any other particles. Finally, the  $D_{c \rightarrow hX}(z_c, Q^2)$  is the fragmentation function for hadron  $h$  to be born out of the parton with flavor  $c$  with the momentum fraction  $z_c = p_h/p_c$ . The assumption behind the factorization is that the particles interacting in the hard interaction  $d\hat{\sigma}_{ab \rightarrow cX}$  travel from infinitely far away to interact, and after interacting, again travel to infinity. This is a good assumption if the scale of the hard interactions is large enough so that the interaction distance  $r \sim 1/Q \ll 1$  fm. If this is true, the phenomena can be separated into short-distance physics, the hard interaction, and long-distance physics, PDFs and fragmentation.

The general idea of PDFs is to map the structure of a free proton, as a function of  $x$ , in a given interaction hardness. This is not calculable from the perturbative QCD, but instead, they need to be determined experimentally. The most



TABLE 2.1 Leading order pQCD processes along with the partonic cross sections and the Feynman graphs for each process [106]. The labels  $i$  and  $j$  refer to different quark species.

| Process                                   | $\hat{\sigma} \times \hat{s} / \alpha_s^2$  | Feynman diagrams   |
|---|---|--|
| $q_i \bar{q}_j \rightarrow q_i \bar{q}_j$ | $\frac{4}{9} \frac{\hat{s}^2 + \hat{u}^2}{\hat{t}^2}$   |   |
| $q_i \bar{q}_i \rightarrow q_j \bar{q}_j$ | $\frac{4}{9} \frac{\hat{t}^2 + \hat{u}^2}{\hat{s}^2}$   |   |
| $q_i \bar{q}_i \rightarrow q_i \bar{q}_i$ | $\frac{4}{9} \left( \frac{\hat{s}^2 + \hat{u}^2}{\hat{t}^2} + \frac{\hat{t}^2 + \hat{u}^2}{\hat{s}^2} - \frac{2\hat{u}^2}{3\hat{s}\hat{t}} \right)$ |    |
| $q_i q_i \rightarrow q_i q_i$             | $\frac{4}{9} \left( \frac{\hat{s}^2 + \hat{u}^2}{\hat{t}^2} + \frac{\hat{s}^2 + \hat{t}^2}{\hat{u}^2} - \frac{2\hat{s}^2}{3\hat{t}\hat{u}} \right)$ |    |
| $q_i \bar{q}_i \rightarrow gg$            | $\frac{8}{3} (\hat{t}^2 + \hat{u}^2) \left[ \frac{4}{9\hat{t}\hat{u}} - \frac{1}{\hat{s}^2} \right]$  |    |
| $gg \rightarrow q_i \bar{q}_i$            | $\frac{3}{8} (\hat{t}^2 + \hat{u}^2) \left[ \frac{4}{9\hat{t}\hat{u}} - \frac{1}{\hat{s}^2} \right]$  |   |
| $gq \rightarrow gq$                       | $(\hat{s}^2 + \hat{u}^2) \left[ \frac{1}{\hat{t}^2} - \frac{4}{9\hat{s}\hat{u}} \right]$  |  |
| $gg \rightarrow gg$                       | $\frac{9}{2} \left( 3 - \frac{\hat{u}\hat{t}}{\hat{s}^2} - \frac{\hat{u}\hat{s}}{\hat{t}^2} - \frac{\hat{s}\hat{t}}{\hat{u}^2} \right)$             |  |

direct constraints to proton PDFs are from deep inelastic scattering (DIS) measurements, particularly from HERA [107]. In the end, PDFs are constructed using a global analysis of all available data that can be described with collinear factorization. As an example, figure 2.2 shows free proton PDF at two different scales  $Q = 2 \text{ GeV}$  and  $Q = 100 \text{ GeV}$  by the CTEQ-TEA collaboration [104]. The valence quark peaks around  $x = 0.2$ , seen more clearly in the left figure, indicating that at high  $x$  values, it is more probable to interact with valence quarks than gluons or sea quarks. Notably, how the gluon distribution is scaled by  $1/5$ , making it vastly dominant in the small  $x$  values, meaning most of the small  $x$  physics is conducted between gluons. Besides the CTEQ-TEA PDFs, there are many alternative parametrizations for the free proton PDF, for example, NNPDF [108], PDF4LHC [109], and HERAPDF [110].

The hard QCD cross section  $d\hat{\sigma}$  can be calculated from the first principles using perturbative QCD. At leading order pQCD calculations, there are a total of eight different processes [106] that are listed in table 2.1. At higher orders, the calculation gets rapidly more complicated. Presently the PDF analysis is done in next-to-leading order (NLO) precision or, in some cases, in NNLO precision [104, 108–110].

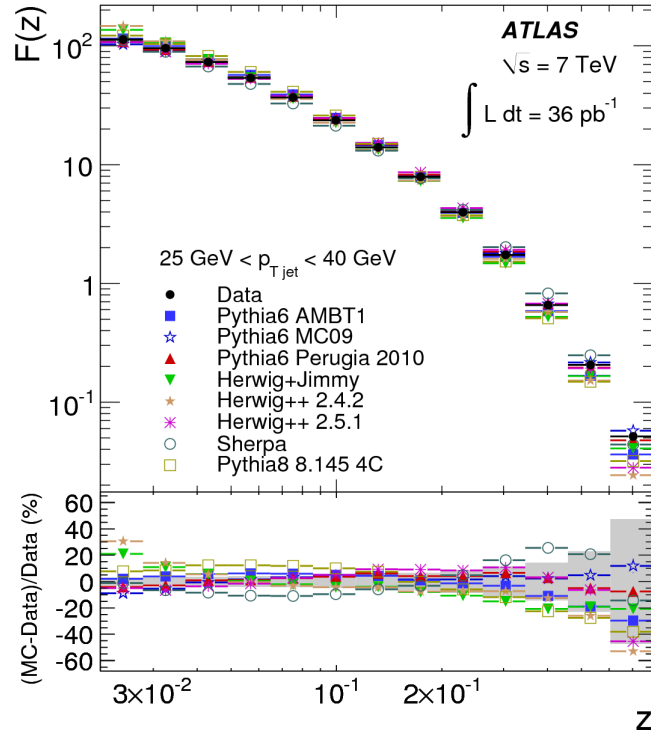


FIGURE 2.3 Measurement of the jet fragmentation in pp collisions by ATLAS using the jet radius parameter  $R = 0.6$  with anti- $k_T$  algorithm. Figure from [113], reprinted under the license CC BY-NC 4.0.

The fragmentation function describes the way hadrons are produced out of a parton. Fragmentation functions cannot be calculated from first principles, but instead, they are calculated with a global analysis from  $e^+e^-$  collisions [111, 112]. Even so, the variation of the fragmentation function on the other hand can be predicted given a large enough scale of the fragmentation  $Q$ . Experimentally the fragmentation has been studied by measuring the spread of the jet constituents in relation to the jet momentum

$$z = \frac{\vec{p}_{\text{jet}} \cdot \vec{p}_{\text{con}}}{|\vec{p}_{\text{jet}}|^2}, \quad (2.4)$$

and in figure 2.3 an example distribution of the relation between a number of charged constituents and  $z$  normalized by the number of jets is seen measured by ATLAS [113], and compared to different MC event generators. This is not the same thing as the fragmentation function itself as the measurement of the  $F(z)$  requires jet reconstruction and has no discrimination between gluons and quarks.

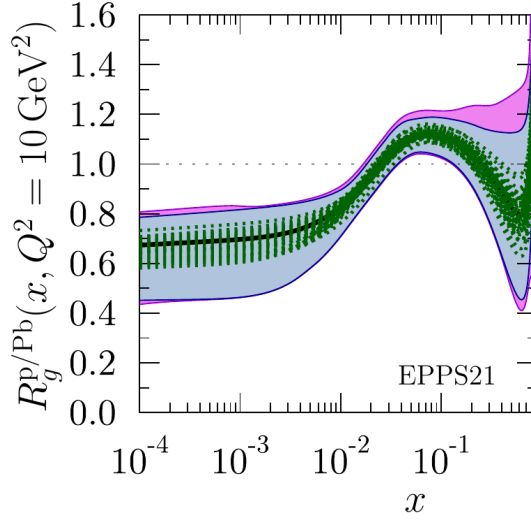


FIGURE 2.4 The nuclear modification of lead ion bound protons for gluons according to EPPS21 nuclear parton distribution function set. The black curve is the central result, green curves represent the nuclear error sets, the purple band is the nuclear uncertainty, and the purple is the total uncertainty. Figure from [2], reprinted under the license CC BY 4.0.

### 2.3 Nuclear effects

The collinear factorization in equation (2.3) is defined for the pp collision system. In order for it to be applicable in heavy ion environment, it is modified to phenomenologically include nuclear effects [105, 114]

$$\begin{aligned}
 d\sigma_{AB \rightarrow hX} \approx \sum_{a,b,c} \iiint dx_1 dx_2 dz f_{a/A}(x_1, Q^2) \otimes f_{b/B}(x_2, Q^2) \\
 \otimes d\hat{\sigma}_{ab \rightarrow cX}(x_1, x_2, Q^2) \\
 \otimes \tilde{D}_{c \rightarrow hX}(z_c)
 \end{aligned} \quad (2.5)$$

where the PDFs and the fragmentation function have now been changed. The PDFs are modified into nuclear PDFs, incorporating the effects of nuclear presence into the PDF. The ratio of the nPDF and PDF is defined as the theoretical nuclear modification factor

$$R_a^A(x, Q^2) = \frac{f_{a/A}(x, Q^2)}{f_a(x, Q^2)}. \quad (2.6)$$

In figure 2.4, the modification of gluonic distribution inside a proton is shown for EPPS21 nPDFs [2]. There is a significant suppression for very small Bjorken  $x$ , but for a region around  $x \sim 0.1$ , there is also an enhancement seen. The suppression is called the nuclear shadowing effect, while the enhancement is called anti-shadowing. The exact nature of the shadowing and anti-shadowing is not clear, but the effect is qualitatively understood [90], and many models besides EPPS21 have been developed, including nCTEQ15 [87] and nNNPDF [88].

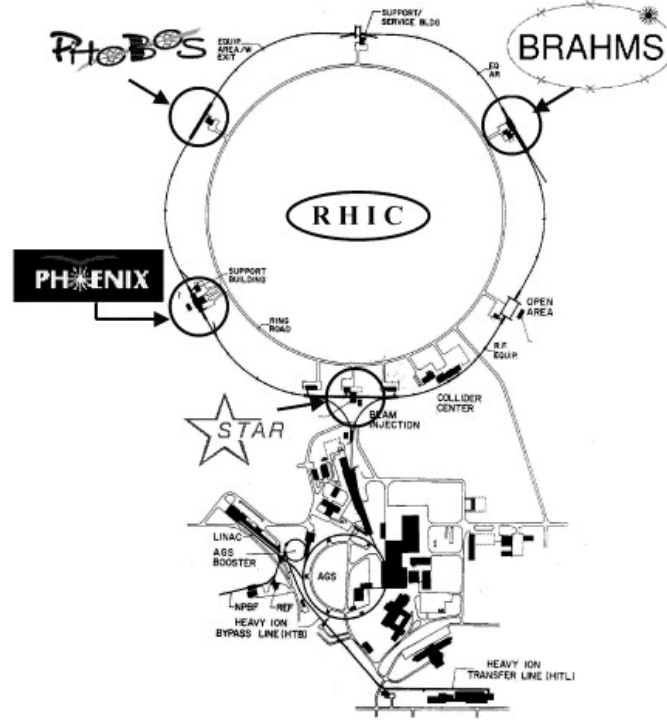


FIGURE 2.5 A schematic figure of the RHIC facilities showing the main experiments along the collider. The RHIC preaccelerator AGS is located in the bottom part of the picture. Figure from [118], reprinted with permission from Elsevier.

The modified fragmentation function is changed phenomenologically so that the medium interactions can change the properties of the hard parton  $c$  [105]

$$\tilde{D}_{c \rightarrow hX}(z_c) \approx \sum_{c'} P_{c \rightarrow c'}(p_{c'} | p_c) \otimes D_{c' \rightarrow hX}(z_{c'}), \quad (2.7)$$

where the new term  $P_{c \rightarrow c'}$  describes the effects which the parton  $c$  experiences during the traversal through the medium. It is usually called the quenching weight as it induces a fractional energy loss [114–117].

## 2.4 Modern heavy ion collider experiments

Relativistic Heavy Ion Collider (RHIC) was built in Brookhaven as a dedicated heavy ion collider in 2000 [118, 120]. RHIC has been colliding various ions such as uranium, zirconium, ruthenium, copper, gold, oxygen, hydrogen, deuterium, and aluminum ions with different combinations, also with protons [3, p.547]. RHIC accelerates the beams up to 510 GeV per nucleon center-of-mass energies. The main experiments participating were BRAHMS [121], PHENIX [122], PHOBOS [123], and STAR [124], last of which is the only one active today. The RHIC complex is shown in figure 2.5 where the preaccelerators, LINAC and AGS, are drawn on the bottom of the figure, after which the beam is directed to RHIC,

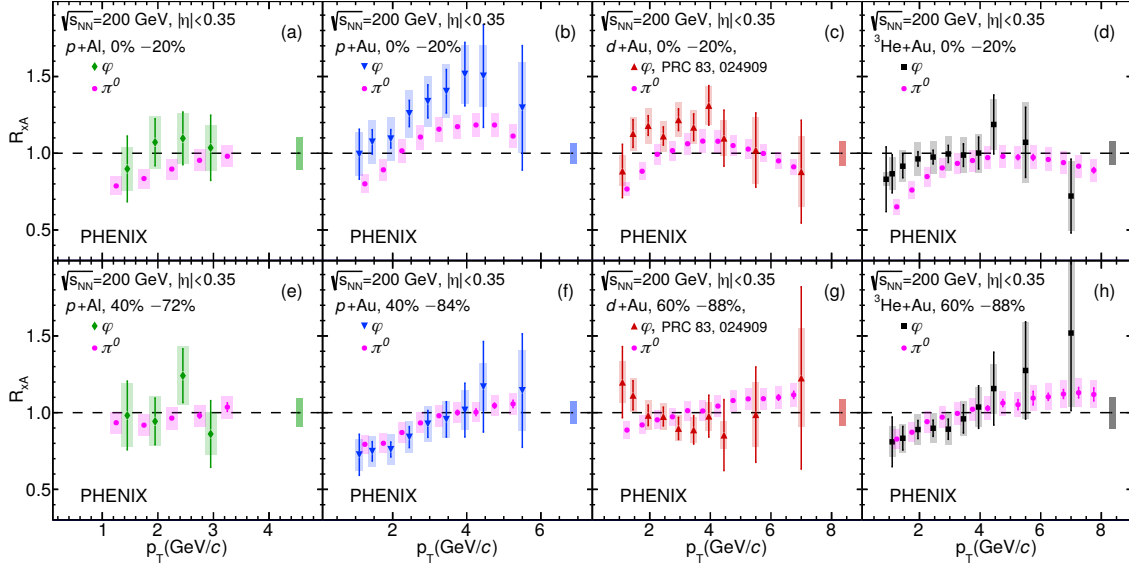


FIGURE 2.6 The nuclear modification factor of  $\phi$  and  $\pi^0$  mesons in various collision systems was measured by the PHENIX experiment at RHIC. Reprinted figure with permission from [119], copyright (2023) by the American Physical Society.

where the four experiments have been situated. Through the many experiments of RHIC, the evidence of QGP in the relativistic heavy ion collisions was strengthened [125–128]. The versatile set of projectiles used in RHIC has enabled measurements of the nuclear modification factor for various combinations. For example, in figure 2.6 are the nuclear modification factors of  $\phi$  and  $\pi^0$  mesons in several different collision systems and centralities measured by PHENIX [119]. As the  $\phi$  meson contains strange and antistrange quarks, this measurement also tests the possible strangeness-enhancement associated as a QGP signal. According to the study, there may be QGP formation, but the volume and lifetime of the medium may be insufficient for observing nuclear modification [119]. Of the four experiments, only STAR continues to this day, having been upgraded during the years [129]. sPHENIX [130] is a new experiment that has been under construction to replace PHENIX.

It is clear that, especially after the successful SPS and RHIC heavy ion programs, there was high interest in relativistic heavy ion collisions at the highest center-of-mass energies [131]. The LHC, which was approved by the CERN Council in 1994 [32], was one of the most promising places to conduct a new ultrarelativistic heavy ion experiment. As one of the experiments participating in the LHC, A Large Ion Collider Experiment (ALICE) was approved in 1997, and the physics measurements of the LHC started in 2009. Other large experiments at the LHC are A Toroidal LHC Apparatus (ATLAS) [132], Compact Muon Solenoid (CMS) [133], and LHC beauty (LHCb) [134], all of which are located around the LHC, shown in the schematic picture of figure 2.7. The beam is first accelerated with linear accelerators shown at the very bottom of the figure. From there, the beam goes through a series of preaccelerators: proton synchrotron booster, proton synchrotron, and super proton synchrotron, before it is injected into the LHC

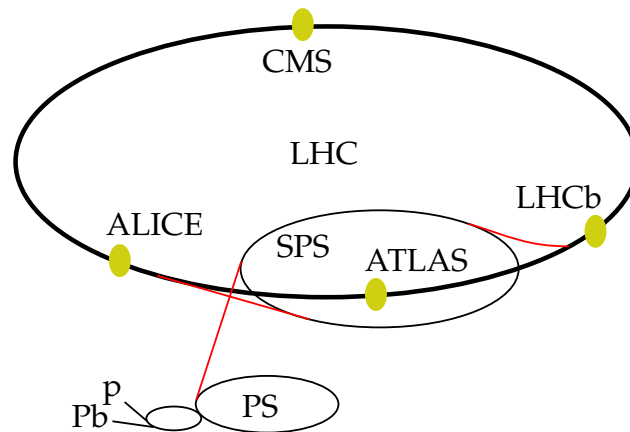


FIGURE 2.7 A schematic figure of the Large Hadron Collider (LHC), showing the main preaccelerators Proton Synchrotron (PS), Super Proton Synchrotron (SPS), and the biggest experiments ALICE, CMS, LHCb, and ATLAS. Figure from [135], adapted under the license CC BY-SA 2.5.

itself. LHC collides protons most of the available time, but a month per year is reserved for heavy ion physics. Depending on the year Pb–Pb, p–Pb, and short runs of Xe–Xe have been collided. In addition to heavy ions, some beam time has been used to generate proton–proton collisions with the same  $\sqrt{s}$  as the lead–lead and proton–lead  $\sqrt{s_{NN}}$ , often called as collisions at the reference energy. These reference pp collisions are needed for comparisons with heavy ion collisions, for example, to calculate the nuclear modification factor or particle ratios. Otherwise, a higher energy pp results need to be interpolated to the same energy as the heavy ion collisions. ATLAS and CMS are experiments focused on various physics goals, with the possibility to measure data on the highest interaction rate for a high number of events [132, 133]. The large central acceptance of the ATLAS and CMS experiments enables the study of jets as a function of rapidity. Figure 2.8 shows the full jet  $R_{pA}$  for minimum bias events for eight different rapidity classes. This shows that the jet  $R_{pA}$  has only a weak  $p_T$  and rapidity dependency. The LHCb, on the other hand, is an experiment focused on the heavy bottom quark [134] and offers unique capabilities due to the possibility to measure also fixed target collisions in LHC.

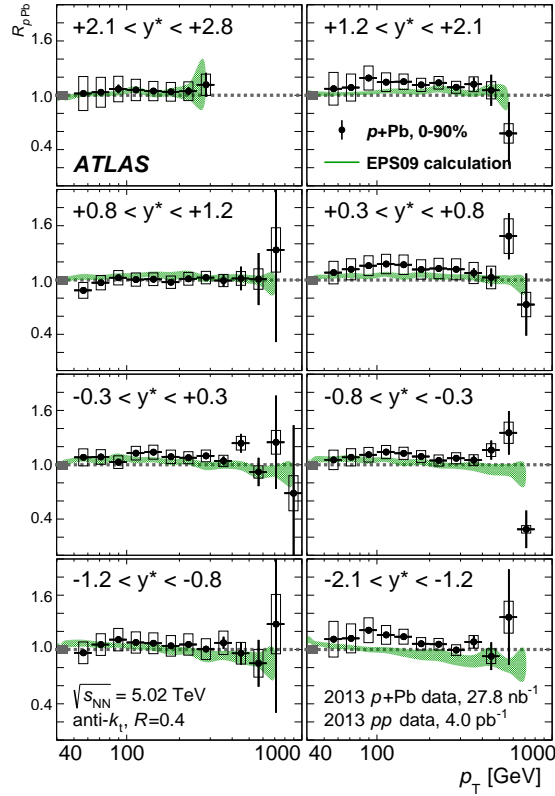


FIGURE 2.8  $R_{pA}$  of full jets, including charged and neutral particles, in several different rapidity regions measured by ATLAS. Figure from [136], reprinted under the license CC BY 4.0.

## 2.5 Monte Carlo event generators

Event generators are used for many purposes. Some generate full event simulations, trying to model the complete collision (Pythia [100], AMPT [137]), while others are built around more specific phenomena, like NLO calculations of parton interactions (POWHEG [138, 139]), or parton modification in a QGP matter (JEWEL [140]).

### 2.5.1 Pythia

Pythia event generator is a multipurpose generator made mostly for ee and pp collisions [100]. In addition, neutrons, pions, and most other light hadrons can also be collided, but all combinations are not possible. Pythia includes all diffractive, non-diffractive, and elastic processes, as shown in figure 2.1. These processes can be set on or off as desired. For example, generating minimum bias events with everything included is done with the `SoftQCD` setting turned on. Generating only non-diffractive hard jet events listed in the table 2.1 is turned on by `HardQCD`. All subprocesses of `SoftQCD` and `HardQCD` can also be turned on or off one by one, in which case Pythia generates events for each process in

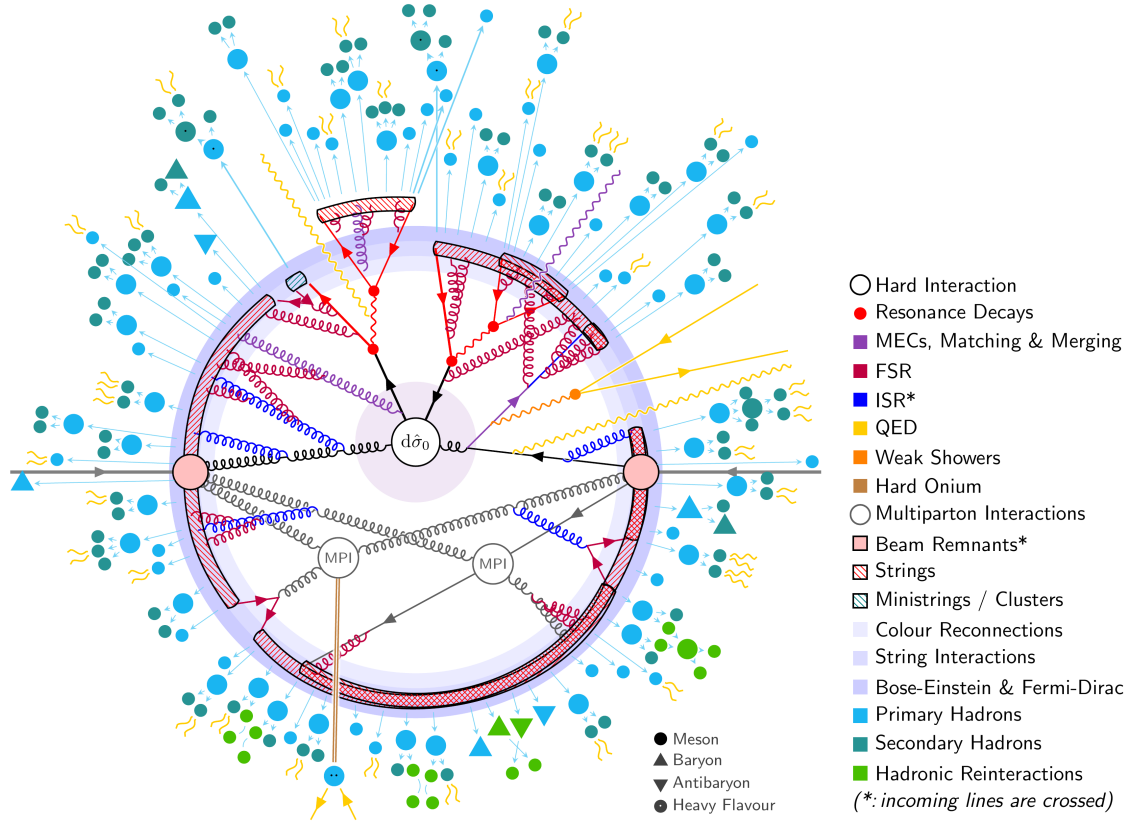


FIGURE 2.9 A schematic figure describing the different parts of the event generation simultaneously. Figure from the Pythia manual [100], reprinted under the license CC BY 4.0.

proportion to their respective cross sections. For jet studies, the `HardQCD` setting is particularly convenient, as it can generate events with a minimum partonic transverse momentum  $\hat{p}_{T,\min}$ . This will significantly speed up the calculation of increasingly rare high  $p_T$  jet events, which are this work's main object of study. This will generate a disproportionate amount of rare events, which need to be scaled according to the cross section of generated events, which is automatically calculated by Pythia. To ensure a good selection of jets across the spectrum, this  $\hat{p}_{T,\min}$  setting is many times used with several different cutoffs together with an upper limit  $\hat{p}_{T,\max}$  to avoid overlap [100].

A schematic figure of a Pythia-generated non-diffractive event is shown in figure 2.9. Pythia generates events in stages, starting with the hard interaction. Because of the uncertainty principle, the time scale of a hard interaction is smaller as the momentum transfer is higher. The interacting partons are sampled from parton distribution functions of the corresponding incoming particles, and the interaction, and outgoing particles, are from the perturbative QCD itself. This may birth short-lived resonance particles, usually  $Z$ ,  $W^\pm$  or top quarks, which are decayed together with the hard interaction.

The Pythia generates particle showers both in the initial state, before the hard interaction, and in the final state, after the hard interaction. The initial state



is handled first and the final state after, and together these are called the parton showering. While the final state radiation describes the decay rate of the final state partons  $a$  to partons  $b$  and  $c$ , the initial state radiation is generated chronologically after the hard event by backward-evolution, giving a production rate of parton  $b$  from an earlier branching of  $a$ . On top of this, there might be multiple interactions between the partons of the colliding hadrons in a single pp collision, which is called multiple parton interactions (MPI). Pythia generates a variable amount of additional  $2 \rightarrow 2$  interactions as MPI, describing most of the underlying event. MPI can also generate hard scatterings, but such events are rare due to the power law falloff of the high  $p_T$  particles. This offers important parameters for multi-jet events.

The hadronization of a Pythia event is handled using the Lund string model [141, 142]. Because of the color confinement of the QCD, each color-charged object creates color strings between the colored objects. These strings receive energy from the end-point particles, which are used to turn the string into a number of hadrons given the energy the string has. On top of the Lund string model, Pythia uses a color reconnection algorithm that determines the topology of the strings [143, 144]. During this, the color strings are updated with a desired scheme, for example, trying to reduce the total length of the strings.

Finally, there is also a possibility to turn on hadronic rescatterings, but this is turned off by default as it adds a significant slowdown. In this rescattering framework, the hadrons themselves can interact with each other, decay, recombine, and reannihilate. The effects of the hadronic rescattering have been noted to be limited in pp collisions [145]. After the hadronization and possible hadronic rescatterings, the event is ready and delivered.

The many stages of Pythia event generation include many phenomenological parameters. These parameters have been tuned according to a complex global analysis over a large amount of measured experimental data. These are called Pythia tunes, and the choice of the tune can depend on the subject of one's study. The default tune for minimum bias and hard processes in pp collisions at LHC energies is Monash 2013 [146], which is the default tune in Pythia.

### 2.5.2 POWHEG

The Positive Weight Hardest Emission Generator (POWHEG) is a next-to-leading order MC generator [138, 139]. POWHEG generates the hardest radiation first using exact NLO calculations. POWHEG does not provide the parton showering, so that has to be simulated with another program, such as Pythia parton showering. This needs to be done with some care as the default Pythia is a LO MC generator that takes the missing orders into account via approximation during the showering. If POWHEG were combined with a default Pythia showering, the NLO additions over LO would be included twice, thus overcounting. POWHEG starts the generation of the event from the hardest interaction with full NLO accuracy, and then showering MC is used to generate subsequent softer radiation. This is enforced by requiring an upper limit on the scale of the radiation, which

would be the hard interaction transverse momentum [138].

### 2.5.3 AMPT

A multi-phase transport (AMPT) model [137, 147] was developed to describe the full evolution of heavy ion collisions. The initial state of AMPT is generated by the Heavy Ion Jet Interaction Generator (HIJING) two-component model [148, 149]. The AMPT then calculates the parton cascade using Zhang’s Parton Cascade (ZPC) algorithm [150] in a way that partons can interact with each other given that they are close enough. Finally, the hadronization is handled either by the Lund string fragmentation [141, 142], or by the quark coalescence model [151]. The Lund fragmentation works similarly to Pythia, but the quark coalescence model is used when the string melting setting is on. Quark coalescence combines the nearest partons into mesons or baryons depending on what is the invariant mass and quark content of the selected set of partons. This is called string melting as the hadrons that would have been produced by the string fragmentation are converted to their valence quarks and antiquarks. String melting has been performing better, especially when modeling the elliptic flow of heavy ion collisions [147, 152]. This was an important factor for us during the event plane studies for the ALICE FIT detector, which is introduced in detail in section 3.3.5.

### 2.5.4 GEANT

To make comparisons between the data reconstructed from the detector signals and theoretical models, the measured spectrum needs to be corrected for the finite efficiency and the acceptance of the detector. We use the detector description and simulation tool GEANT [153, 154] to simulate the interactions between particles and detector-related material. To simulate the detector response, ALICE has built the full ALICE detector within the GEANT program using CAD. The response can be calculated by feeding simulated particles into the simulated ALICE detector from any MC model, like, for example, Pythia or AMPT, which were introduced above. The primary particles from the MC provide the particle information which GEANT uses to calculate particle–matter interactions. The interactions are calculated with many theoretical and experimental models, such as ionization, pair production, bremsstrahlung, and so on. As an example, the mass-stopping power of muons is illustrated in figure 2.10, which shows how positive muons lose energy according to the energy of the muon. A wide range of models is needed to account for the possible interactions in high-energy physics experiments like ALICE. The interactions between particles and detectors are used to reconstruct tracks in the same way as during data taking.

For my work, Pythia has generally been the most used MC generator for testing and modeling purposes. In addition, POWHEG events were used alongside Pythia as a model comparison for the main measurement, which I present

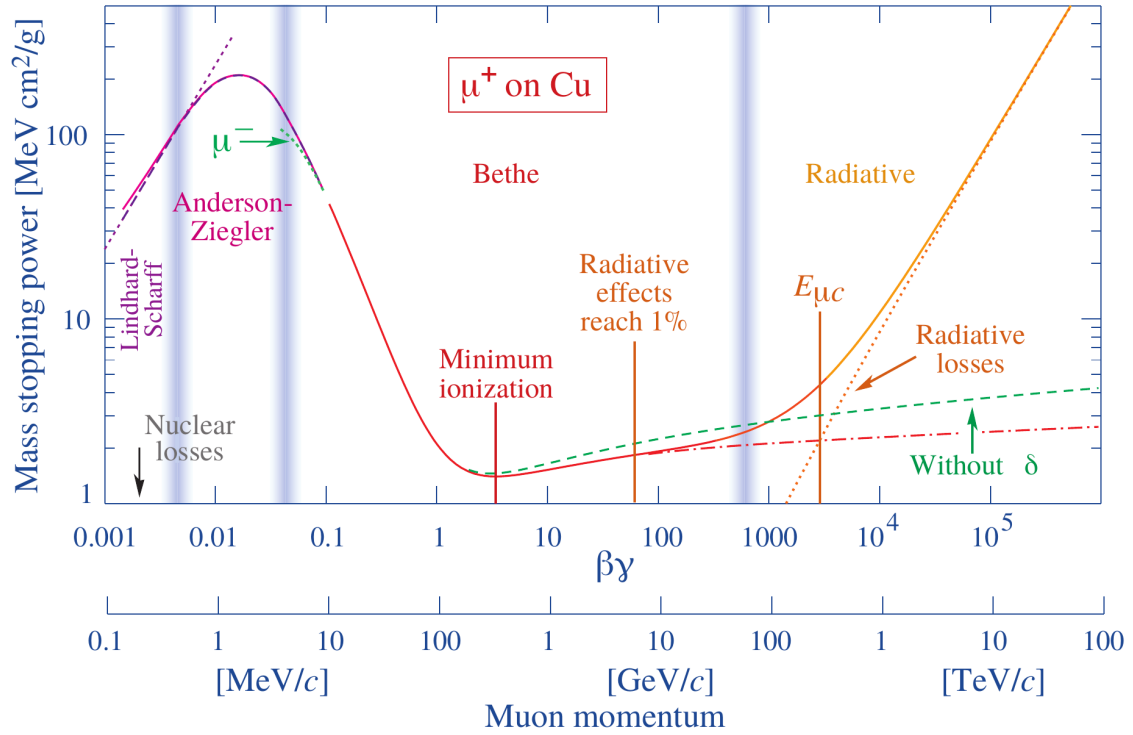


FIGURE 2.10 The mass-stopping power for positive muons in copper material as a function of  $\beta\gamma = p/Mc$ . Several different dominating effects are listed in different momentum regions of the graph. Data from [155, 156], and the figure from [3], reprinted under the license CC BY-NC 4.0.

in section 7.2. ALICE also uses mostly Pythia as a source of MC particles for the purposes of the GEANT detector simulation, which is used during the unfolding, which I explain in section 6.6. Additionally, we studied the reconstruction of the event plane with AMPT and GEANT in section 3.3.5.

## 3 A LARGE ION COLLIDER EXPERIMENT: ALICE

### 3.1 Coordinate system

ALICE uses a coordinate system with the beam axis defining the  $z$  direction, where positive  $z$  points towards the ATLAS experiment and negative  $z$  towards the CMS experiment, as seen in figure 2.7. These directions are dubbed the A-side and the C-side of the ALICE detector.  $x$ -axis points towards the center of the LHC ring, which leaves the  $y$ -axis pointing towards the sky. The detector acceptances are defined using pseudorapidity, which uses the same sign definitions as the  $z$ -axis. The azimuthal angle is defined to be zero at  $x$ -axis and  $\pi/2$  at  $y$ -axis [157].

### 3.2 ALICE detector during LHC Run 2

The ALICE detector [39] was built as a dedicated ultrarelativistic heavy ion collision experiment as a part of the Large Hadron Collider. The most characteristic aspect of a heavy ion collision is the extremely high number of particles produced which is one of the key points the detector has been designed for. Figure 3.1 is a schematic of the ALICE detector as it was during the LHC Run 2, between the years 2015 and 2018. The events analyzed in this thesis have been measured during this time period. A set of detector acceptances and locations important for the work in this thesis has been listed in table 3.1. After 2018 the LHC Run 2 ended, and the detector complex and the participating experiments entered a time period called the long shutdown 2, during which maintenance and upgrading can be applied. The long shutdown 2 lasted from 2018 until 2022. The upgrades from the ALICE perspective are discussed in detail in section 3.3.

For many high-energy particle physics programs, tracking is a key feature, and it is implemented with the help of several different subdetectors. The Inner Tracking System (ITS) is a six-layered silicon vertex detector and is the first de-

TABLE 3.1 Information about the location and acceptances of the ALICE subdetectors [39].

| Detector | $z$ (mm) | $\eta_{\min}$ | $\eta_{\max}$ |
|----------|----------|---------------|---------------|
| SPD      | central  | -2.0          | 2.0           |
| SDD      | central  | -0.9          | 0.9           |
| SSD      | central  | -0.97         | 0.97          |
| TPC      | central  | -0.9          | 0.9           |
| V0-A     | 3400     | 2.8           | 5.1           |
| V0-C     | -897     | -3.7          | -1.7          |
| T0-A     | 3750     | 4.61          | 4.92          |
| T0-C     | -727     | -3.28         | -2.87         |

detector which the outgoing mid-rapidity particles can interact with. It consists of three different detector parts, each having two layers, the Silicon Pixel Detectors (SPD), Silicon Drift Detectors (SDD), and Silicon micro-Strip Detectors (SSD), in the order from inside to outside. The design of each of these subdetectors has been done so that the innermost detectors would have the best parameter resolution, as the particle density is the largest there. This is why the SPD has the finest granularity out of the three, with a cell size of  $425 \mu\text{m}$  to  $z$  direction by  $50 \mu\text{m}$  radially [39]. With this granularity, the SPD can differentiate tracklets even in heavy ion collisions with as much as  $50$  particles per  $\text{cm}^2$  as reported in the technical design report [39]. The SDD and SSD have an analog readout that can provide  $dE/dx$  measurement at very low transverse momentum. ITS is an essential part of the ALICE tracking system, which will be discussed in detail in section 4.2. The vertex position ITS provides can be measured at a resolution of better than  $100 \mu\text{m}$ .

Time Projection Chamber (TPC) [158] shown in figure 3.2 offers the main charged particle tracking capabilities for ALICE in the central region. It consists of a large barrel of about  $5.6$  m in diameter and  $5$  m in length, resulting in a pseudorapidity acceptance around the central pseudorapidity  $|\eta| < 0.9$ . It is split into two portions with a central electrode. Inside the TPC, charged particles ionize the  $\text{Ne-CO}_2\text{-N}_2$  gas mixture, after which the electric field inside the chamber will cause the electrons to drift to the endplates of the cylinder, which can be seen in the figure 3.2 with a dark green color. The position where the electrons end up in the end plate and the drift timing are located accurately. The drift time provides the track  $z$  information, so the trajectory of the original charged particle can be traced. TPC was designed with the extremely high particle multiplicity of heavy ion collisions in mind, at maximum  $8000$  particles per event by the estimates [159].

Minimum bias triggering, which is covered in detail in section 4.1, is done with a combination of signals in the forward-facing scintillator counter detectors V0-A and V0-C and in some cases, in the ITS. The V0 signal has also been widely

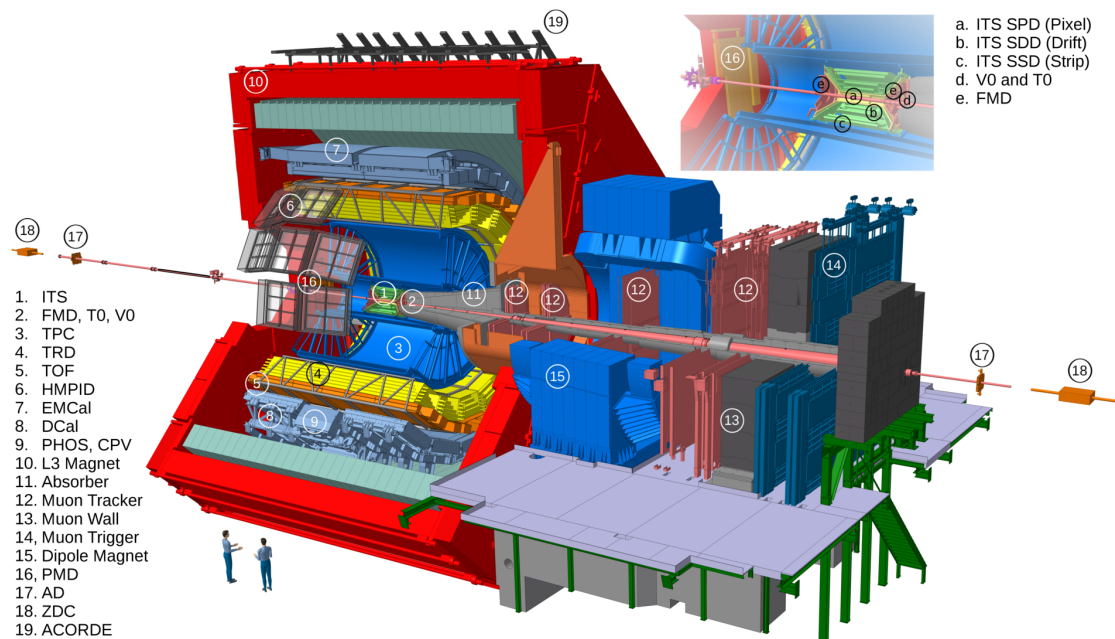


FIGURE 3.1 A figure describing the subdetectors of ALICE during the initial running period until 2022. Positive rapidities face left in this figure. Figure from [17], reprinted under the license CC BY 4.0.

used as an indicator of the centrality of heavy ion collisions. T0 is a Cherenkov counter based detector mainly used for generating a collision time, especially important for the time-of-flight (TOF) detector, but can also act as an alternative minimum bias trigger source.

Other aspects of the ALICE detector include, for example, a muon arm, electromagnetic calorimeter (EMCal), and TOF detector. As seen in figure 3.1, ALICE has been built asymmetrically as the muon tracker takes up a large space on the C-side of the detector. It is specially designed to detect vector-meson resonances decayed in the  $\mu^+\mu^-$  channel which is studied with ultra-peripheral heavy ion collisions because of the larger electromagnetic fields producing vector-mesons [161–167]. ALICE EMCal can be used to measure neutral particles. However, it has a limited 107 degree azimuthal acceptance. To accompany the EMCal, a dijet calorimeter has been included with an azimuthal acceptance of 60 degrees on the opposite side to the main EMCal calorimeter [168]. Particle identification in ALICE is handled by a combination of detectors, the TOF detector being one of them. TOF provides particle identification information up to a transverse momentum of 2.5 GeV for pions and kaons and 4 GeV for protons [39].

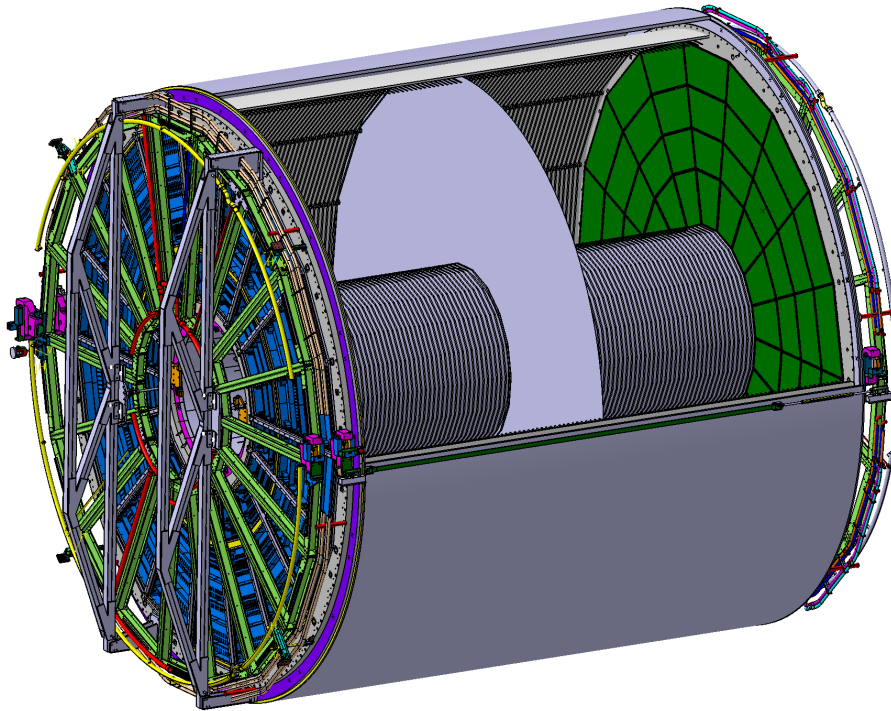


FIGURE 3.2 A closeup schematic of the Time Projection Chamber of the ALICE detector. The main characteristics of TPC are the central electrode which splits the detector, and the endplates with readout wire chambers for charge detection. Figure from [160], reprinted under the license CC BY 4.0.

### 3.3 Overview of the ALICE upgrade for LHC Run 3

LHC operates on a long-term plan for running beams, upkeep, and upgrades. The times when consistent beams are provided are numbered as run 1, 2, 3, and so on, and between the beam runs, there are long shutdown periods which is the optimal time for instrument maintenance and upgrading for the LHC itself and the experiments. There are shorter shutdown periods as the need arises, but the scheduling for long shutdowns in advance is required as some of the updates are very thorough and require a lot of planning, research, and building time. The LHC ended the four-year-long period of run 2 in 2018 [169], and the long shutdown 2 period started.

The long shutdown 2 lasted till 2022 and has introduced many updates for all of the LHC detectors, but especially to the ALICE detector [160]. As ALICE is a dedicated heavy ion collision detector, it has been built with the capability to measure a large number of tracks with great precision. This was a tradeoff with speed as the TPC requires drifting time. Without the upgrade, the TPC could not read all interactions at the average designed collision rate of 50 kHz Pb–Pb collisions during run 3, as the tracks create pile up within the drift time window of approximately  $100 \mu\text{s}$  [160]. This can be solved with a continuous readout technique.

The continuous readout technique was fitted in the ALICE detector system during long shutdown 2. The data will be saved without any trigger but instead in time intervals called time frames which last approximately 11 ms each. This requires the sorting of events at a later time when there are particles from different collisions simultaneously inside the TPC drift chamber. Without any modifications to the TPC, this would not be possible. TPC has been using a technique that requires an active ion gating grid to deny ions drifting back into the drift volume, and this needs to be run with a trigger. To circumvent this, the whole TPC readout system needed to be changed. The active ion gating grid was superseded by Gas Electron Multipliers (GEMs) [170], which can block most of the ion backflow while simultaneously providing amplification [160, 171, 172].

The inner tracking system, an essential detector for high-precision tracking and vertexing, received an overhaul for the LHC Run 3. First, the detector can stand closer to the interaction point as the beam pipe radius was reduced from 29 mm to 16 mm. This helps especially with pointing resolution which benefits the secondary vertex reconstruction capabilities [173]. The innermost layer stands at a radius of 18 mm from the center of the beam pipe [160]. The detector material was reduced for fewer secondary interactions, causing less smearing of data. The ITS also gave up the particle identification capabilities after the upgrade, as all measurements with ITS particle identification have been concluded during Run 2. Lastly, the maximum interaction readout rate of 1 kHz has raised up to 100 kHz for Pb–Pb collisions and to 400 kHz for pp collisions, which is an essential upgrade for the LHC Run 3 purposes [173].

For Run 3, the ALICE muon spectrometer was upgraded with a Muon Forward Tracker (MFT) to extend the muon physics program. The MFT is a silicon detector with five disks at different distances from the interaction point. It is situated in front of the absorber, after which the muon trackers are located. The main goal of the upgrade was to improve the pointing resolution of muons and add vertexing capabilities [160, 174].

Besides the TPC, the continuous readout without a trigger is not possible for most of the ALICE detectors. Some detectors utilize the trigger information, and for some, it is strictly required for operating [175]. This is not a problem as the triggered data is combined with the data received with continuous readout mode. As such, the triggered mode of some detectors can be thought of as a sub-mode of the continuous mode [176].

The continuous readout technique requires a software update for the purposes of online data reduction and calculation of time frames. The continuous readout is split into time frames, separated by a heartbeat trigger, which is a non-physics trigger launched approximately every 100 ms, which is the drift time of TPC. This timing was decided to minimize events that are split into two time frames [176]. During Run 3, the detector outputs 3.5 TB/s of raw data, which must be significantly compressed before storing. For these purposes, a new online & offline framework was developed, called O<sup>2</sup>. The O<sup>2</sup> contains components for ALICE first level processors (FLP), event processing nodes (EPN), physics data processing (PDP), and the analysis software. FLP will receive the raw data



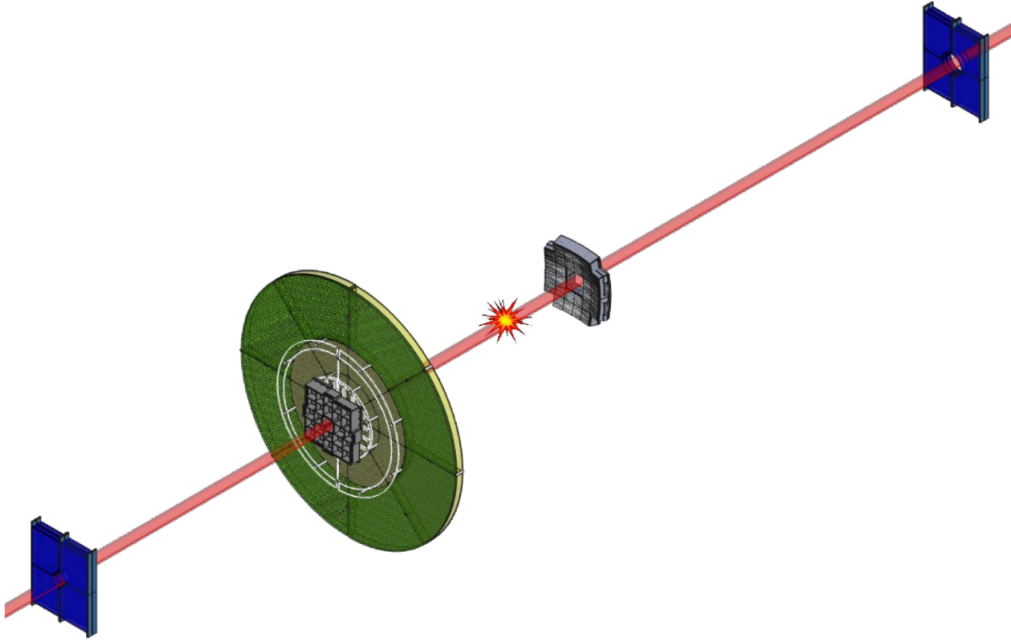


FIGURE 3.3 The Fast Interaction Trigger. Subdetectors of FIT from left to right: FDD-A, FT0-A together with FV0, interaction point, FT0-C, and FDD-C. Figure from [175], reprinted with permission from the author.

and calculate sub time frames, reducing the output from 3.5 TB/s to 900 GB/s. Sub time frames are transferred to the EPN farm for compressed time frame calculation, outputting approximately 130 GB/s of data which will be saved to disk.

### 3.3.1 Fast Interaction Trigger: FIT

In the previous section, the concept of continuous readout was introduced as a way to gather data at a higher rate, 50 kHz for Pb–Pb collisions and 200 kHz for pp and p–Pb [176]. Many subdetectors of ALICE still do need the triggering system, or use the triggering information in their operations [175, 176]. For such capabilities, Fast Interaction Trigger was devised. In addition to online capabilities, such as the triggering and luminosity measurement, FIT can also provide many offline analysis tools [177]. FIT can be used for timing purposes for particle identification, collision centrality classification, and event plane orientation determination for heavy ion collisions. FIT consists of four distinct parts located in the forward and backward regions from the interaction point, as depicted in figure 3.3. The longitudinal distance from the interaction point and the pseudorapidity acceptances of each subdetector are listed in table 3.2.

The furthest away from the interaction point are the Forward Diffractive Detectors (FDD) A and C [178], which replace the ALICE Diffractive detector. The A and C arrays are nearly identical, consisting of eight rectangular scintillator pads in two layers. The large rapidity interval of the FDD allows the identification of collisions with large rapidity gaps like diffractive processes or photon-induced ultra-peripheral collisions. FDD can also be used to estimate the centrality of a

TABLE 3.2 Information about the location and acceptances of the FIT subdetectors during LHC Run 3 [160].

| Detector | $z$ (mm) | $\eta_{\min}$ | $\eta_{\max}$ |
|----------|----------|---------------|---------------|
| FT0-A    | 3305     | 3.5           | 4.9           |
| FT0-C    | -843     | -3.3          | -2.1          |
| FDD-A    | 17 000   | 4.8           | 6.3           |
| FDD-C    | -19 500  | -7.0          | -4.9          |
| FV0      | 3160     | 2.2           | 5.0           |

heavy ion collision based on the FDD signal.

Closer to the interaction point is the detector pair FT0-A and C. FT0 consists of two detector arrays made of quartz Cherenkov radiators. Unlike the other subdetectors of FIT, the FT0-C has been built in a convex shape as the interaction point is so close to the detector. Each quartz radiator has an area of  $2.65 \text{ cm} \times 2.65 \text{ cm}$ , with FT0-A having 96 radiators and FT0-C 112. Higher granularity is good for measuring multiplicity and event plane angle.

FV0 is located right in front of FT0-A and consists of a set of plastic scintillators in five rings with equal pseudorapidity coverage. The rings are separated into eight sectors, except the outer ring, which is split into 16 sectors. This granularity is sufficiently good for measuring multiplicity and event plane angle of heavy ion collisions. FV0 is also used to monitor the LHC background conditions and luminosity information in real-time, which is forwarded to the LHC for beam tuning [160, 175]. FV0 and FT0 together provide the fastest trigger in ALICE.

### 3.3.2 Event plane determination

As a part of ALICE service work, in which I participated together with Heidi Rytkönen, we studied the performance of the FIT event plane resolution. The following text explains the physics and the work related to this task in detail.

The shape of the QGP droplet is an interesting property of heavy ion collisions. Due to the collision geometry, the pressure gradients in the transverse plane are anisotropic, thus causing the collective elliptic flow of particles. The information about the orientation of the droplet can be used as an advantage, for example, in path length studies of jet quenching [179, 180]. The orientation of the droplet is described by the reaction plane of the event, which is defined as the vector between the centers of the colliding nuclei perpendicular to the  $z$ -axis. The azimuthal angle in which the reaction plane is in laboratory coordinates is called the reaction plane angle and is shown in figure 3.4.

The reaction plane is an angle that cannot be observed directly but has to be estimated via particle information. It has been found that hydrodynamics describes the collective behavior of the softly produced particles of the collision [181]. As the collision zone, as shown in figure 3.4, is anisotropic, different directions in the transverse plane have different pressure gradients of the hydro-

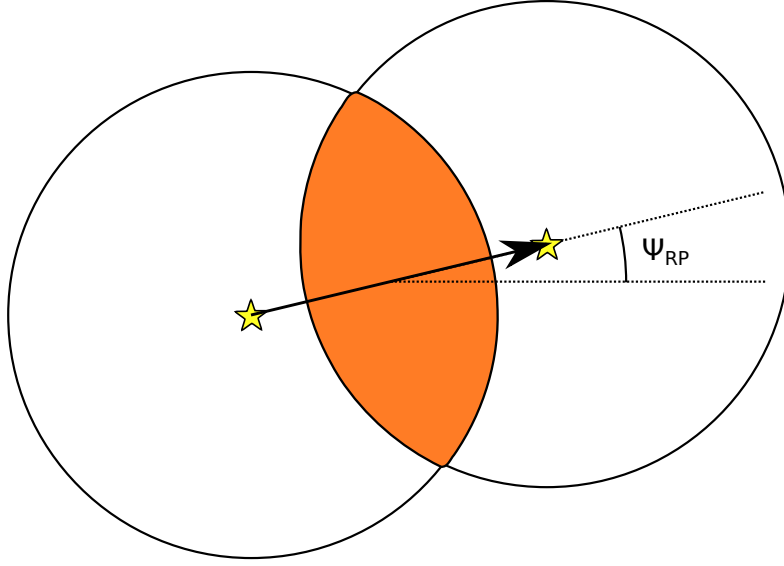


FIGURE 3.4 A schematic drawing of the transverse plane of the collision zone of mid-central heavy ion collision, where the centers of the ions are marked with yellow stars. The arrow represents the impact parameter  $\vec{b}$ , and the angle  $\Psi_{\text{RP}}$  is the reaction plane angle.

dynamic QGP, which then will cause a collective flow behavior of particles. By measuring the particles, we can study the collective behavior by using a Fourier transform [182] of the azimuthal angle distribution of event particles

$$\frac{dN}{d\phi} = \frac{N}{2\pi} \left( 1 + \sum_{n=1}^{\infty} 2v_n \cos(n[\phi - \psi_n]) \right), \quad (3.1)$$

where  $N$  is the amount of particles,  $v_n$  is the flow strength of  $n$ th harmonic, also called the flow coefficient, and  $\psi_n$  defines the symmetry plane angle of the  $n$ th harmonic. The symmetry plane describes the direction of the flow, and it is usually different for each harmonic. Event plane angle  $\Psi_n$ , on the other hand, describes the direction of the flow as we see it from the limited number of particles, which is usually slightly different from the symmetry plane. The fewer particles an event has, the more uncertain the event plane angle will be, thus deviating from the underlying symmetry plane. The event plane converges into the symmetry plane on the limit of infinite particles in a collision. As the symmetry plane cannot be measured directly, the discussion revolves around measuring the event plane and the observed flow coefficient, which can then be corrected for the true flow coefficient, as will be shown in the next section.

The interpretation of the flow coefficients is seen in figure 3.5.  $v_1$  describes directed flow, which means that by average, the whole event is moving in a certain direction, and this is usually close to zero in the LHC energies, as the beam does not have transverse momentum where the directional flow could originate. Directed flow is relatively challenging to measure due to the high sensitivity to the total momentum conservation of an event [183]. In lower energy fixed target ion-ion collisions, like in the BNL AGS, the directional flow was noticed

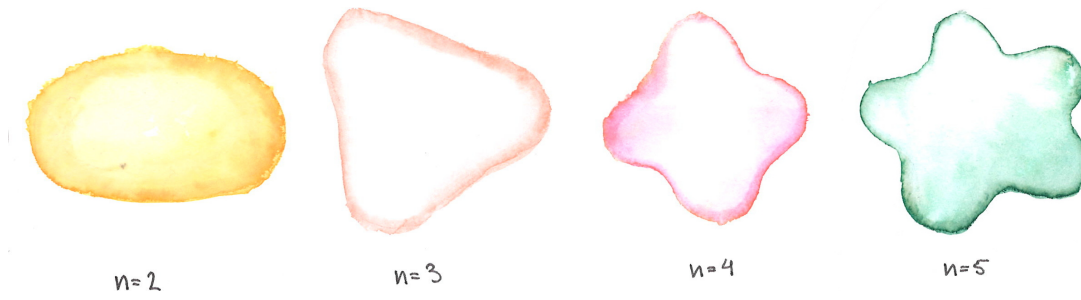


FIGURE 3.5 A physical interpretation of the different flow coefficients, starting from  $v_2$  in the leftmost picture to  $v_5$  in the rightmost picture. Image courtesy of Anna Öennerstad.

to be significant [184]. On the other hand,  $v_2$  shows the strength of the elliptic flow. The pressure gradients of a collision will drive the elliptic flow in the case where the collision zone has an almond shape, causing an excess of particles in the direction of the event plane angle as to the perpendicular direction. Thus in mid-central collisions, the eccentricity and the flow coefficient are well correlated [185]. This information suggests that in these mid-central cases, the event plane is a good estimate of the initial shape of the collision area. Higher flow coefficients describe finer preferences in direction as drawn in figure 3.5 and are influenced by final-state collective dynamics and initial-state fluctuations [186]. One of the main offline analysis functionalities of the new FIT detector [177] is to determine low harmonic event planes of heavy ion collisions.

### 3.3.3 Flow coefficients

There are many ways of calculating the flow coefficients and the event plane. The method I used was via flow vectors, also known as Q-vectors [187]. For each particle, we have a unit vector describing the direction in azimuthal angle  $\phi$  in a complex plane

$$q_n = x_n + iy_n \equiv \cos(n\phi) + i \sin(n\phi), \quad (3.2)$$

where  $n$  refers to the  $n$ th harmonic, as in equation (3.1), and the azimuthal angle is defined by the direction of the momentum of the particle. The sum of these unit vectors for particles in a single event will give us the Q-vector of the event

$$Q_n = \sum_{\text{particles}} q_n \equiv X_n + iY_n = |Q_n| [\cos(n\Psi_n) + i \sin(n\Psi_n)], \quad (3.3)$$

which can be used to calculate the event plane angle of the event

$$\Psi_n = \frac{1}{n} \arctan\left(\frac{Y_n}{X_n}\right). \quad (3.4)$$

With the event plane coefficient, the observed flow coefficient can be calculated with

$$v_n^{\text{obs}} = \langle\langle \cos(n[\phi - \Psi_n]) \rangle\rangle, \quad (3.5)$$

where  $\langle\langle \dots \rangle\rangle$  represents an average over all particles in all measured events. In this equation, one needs to avoid auto-correlation effects if the event plane angle has been calculated with the same set of particles as the  $v_n^{\text{obs}}$  would be calculated. In this case, auto-correlation means that one would compare the azimuthal angle of a particle  $i$  to the event plane angle  $\Psi_n$  where the said particle  $i$  was used to calculate the  $\Psi_n$  itself. This is avoided by subtracting the said particle from the  $\Psi_n$  before comparing  $\Psi_n$  to the particle azimuthal angle  $\phi$  and then adding it back to the  $\Psi_n$  for the calculations after particle  $i$ . For the studies we have conducted here, the  $v_n^{\text{obs}}$  has been calculated with mid-rapidity particles and the event plane with FIT particle information, thus avoiding the auto-correlation entirely.

As outlined in the previous section, the observed flow coefficient, as calculated in equation (3.5), needs to be corrected as the event plane differs from the symmetry plane, which represents the true direction of the flow. To estimate how close the event plane is to the symmetry plane, a resolution of the event plane is calculated as

$$R_n = \langle \cos(n[\Psi_n - \psi_n]) \rangle, \quad (3.6)$$

where  $\psi_n$  is the symmetry plane angle, and the angled brackets denote an average over all events.

Equation (3.6) is not directly usable in measurement as the symmetry plane angle  $\psi_n$  is unknown. By using sub-event methods, the resolution  $R_n$  can be calculated without the symmetry plane information. In the two-subevent method [188] we split the particles of the event into two equal-sized parts A and B, which each have their own event plane angle. Then one can write

$$\langle \cos(n[\Psi_n^A - \Psi_n^B]) \rangle = \langle \cos(n[\Psi_n^A - \psi_n + \psi_n - \Psi_n^B]) \rangle \quad (3.7)$$

$$= \langle \cos(n[\Psi_n^A - \psi_n]) \cos(n[\Psi_n^B - \psi_n]) \rangle \quad (3.8)$$

$$+ \langle \sin(n[\Psi_n^A - \psi_n]) \sin(n[\Psi_n^B - \psi_n]) \rangle$$

$$\approx \langle \cos(n[\Psi_n^A - \psi_n]) \rangle \langle \cos(n[\Psi_n^B - \psi_n]) \rangle \quad (3.9)$$

$$\approx R_{n,\text{subevent}}^2 \quad (3.10)$$

$$\rightarrow R_{n,\text{subevent}} \approx \sqrt{\langle \cos(n[\Psi_n^A - \Psi_n^B]) \rangle}, \quad (3.11)$$

where the first approximation assumes that the two subevents do not correlate except via the collective flow. Also, as the  $\langle \Psi_n - \psi_n \rangle \approx 0$ , the sinus will be on average zero. The second approximation assumes that as the subevent sizes are the same sized by definition, the resolution of the two sets will be the same as well. Thus the resolution of the subevents can be solved, as shown in the final line of the equation.

Now we have a resolution parameter for half an event. This is good, but it has the inherent problem that the resolution depends on the event's multiplicity, so this resolution is worse than the whole event resolution. To solve the full event resolution, we can use a function [181, 189] to describe the resolutions

dependency of the multiplicity

$$R(\chi) = \frac{\sqrt{\pi}}{2} \chi \exp\left(-\frac{\chi^2}{2}\right) \left( I_0\left(\frac{\chi^2}{2}\right) + I_1\left(\frac{\chi^2}{2}\right) \right), \quad (3.12)$$

where  $\chi = v_n \sqrt{M}$ ,  $M$  is multiplicity, and  $I$  is the modified Bessel function [181]. In the limit of infinite multiplicity, the modified Bessel function has an asymptotic equivalency [190]

$$I_n\left(\frac{\chi^2}{2}\right) \sim \frac{\exp\left(\frac{\chi^2}{2}\right)}{\sqrt{\pi\chi}}, \quad (3.13)$$

which shows that the resolution approaches unity as multiplicity grows. As we have split the multiplicity in half, we can find the full event  $\chi$

$$\chi_{\text{full}} = v_n \sqrt{2M} = \sqrt{2} \chi_{\text{subevent}}. \quad (3.14)$$

The full event resolution is calculated by first solving  $\chi_{\text{subevent}}$  from equation (3.12), and then using the information in equation (3.14)

$$R_{\text{full}} = R\left(\sqrt{2} \chi_{\text{subevent}}\right), \quad (3.15)$$

and with this, we can calculate the flow coefficient of the full event

$$v_n = \frac{v_n^{\text{obs}}}{R_{n,\text{full}}}. \quad (3.16)$$

If we would like to use subevents with different multiplicities, one way to do so is to use the three-subevent method. Now each of the subevents can have different multiplicity and thus different resolutions. The equation (3.10) is now modified to

$$\left\langle \cos\left(n \left[ \Psi_n^A - \Psi_n^B \right] \right) \right\rangle \approx R_n^A R_n^B, \quad (3.17)$$

and the same can be done for the pair of subevents B and C and then again for A and C. With this information, we can see easily that, for example, the resolution of subevent A is

$$R_n^A \approx \sqrt{\frac{\langle \cos(n [\Psi_n^A - \Psi_n^B]) \rangle \langle \cos(n [\Psi_n^A - \Psi_n^C]) \rangle}{\langle \cos(n [\Psi_n^B - \Psi_n^C]) \rangle}}, \quad (3.18)$$

which can be used to calculate the corrected flow coefficient for detector A in the same way as for two event corrections in equation (3.16)

$$v_n = \frac{v_n^{\text{obs}}}{R_n^A}. \quad (3.19)$$

As these techniques should yield the same result, we created a toy MC model for validating the two and three subevent methods against the inputted flow in the toy MC and against each other. The toy MC generates particles in azimuthal distribution according to the Fourier series as written in equation (3.1)

for the first five terms until  $v_5$ . The pseudorapidity distribution of particles was taken from the ALICE measurement [191], and the flow strength was inputted per centrality from the ALICE measurement [192]. The toy MC did not end up using transverse momentum information for the validation purposes of this thesis, but each particle's transverse momentum was sampled using an exponential function.

The toy MC analysis used ALICE V0 and T0 detector acceptances as shown in table 3.1. The two-subevent method randomly split the particle information into two parts to create two equal-sized subevents from the particle information of each subdetector V0-A, V0-C, or T0. The three-subevent method used one subevent from a subdetector of choice and two subevents from TPC acceptance split into two parts, negative and positive rapidity, with a 0.2 rapidity gap between them.  $v_{\text{obs}}$  was calculated from the particle information from the TPC acceptance as that would be a realistic case in the data analysis later.

The result of the flow coefficient analysis with both two and three subevent methods can be seen in figure 3.6. In the left-hand side figure, the three-subevent and two-subevent methods agree well, along with the inputted  $v_2$ . From the right-hand side figure, the resolution of the toy MC model is seen and compared to the measured ALICE resolution of V0-C. The resolution is much higher than the measured resolution, which is to be expected of an ideal toy model. These results validate the flow coefficient methods, although it would be interesting to see in future studies how well the two and three-subevent methods match if the resolution of the toy MC would be artificially lowered.

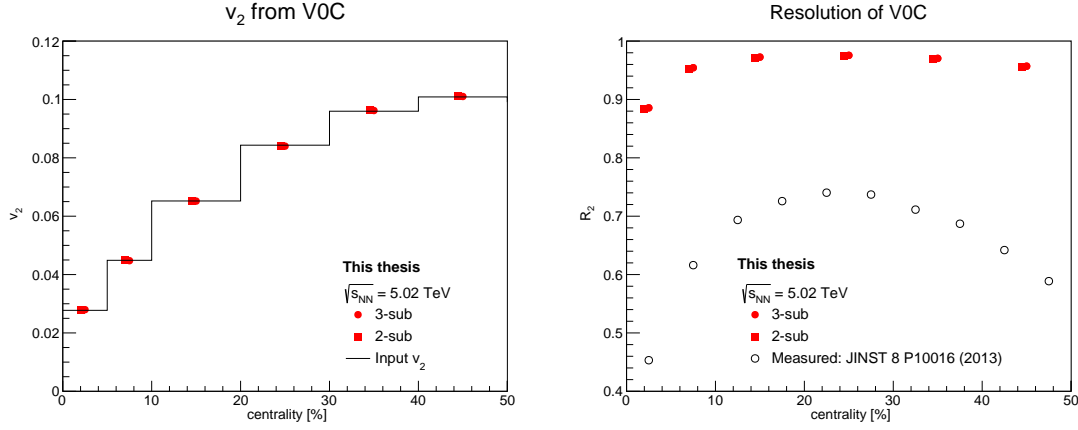
In the real-world use case, the forward detectors are divided into channels (48, 96, or 112 in the case of FV0, FT0-A, and FT0-C), making the split into two subevents not feasible. Using the three-subevent method, we can use all of the channels of the forward direction by using the TPC as a help for subevents B and C.

### 3.3.4 $Q$ -vector corrections

The detector performance is always non-optimal due to measurement inefficiencies. There also might be areas of the detector not performing optimally or completely switched off for the time of the run. In case the detector would favor some areas over others, it may seem like there is a presence of a flow signal without any corrections.

Averaged over all events, the physics should have no preference for a direction. Thus the event plane angle distribution should be flat. The event plane is calculated with the help of the  $Q$ -vector as shown in equation (3.4). For the event plane distribution to be flat, the  $Q$ -vector components  $X$  and  $Y$  need to be distributed completely symmetrically. Using this information, we can calculate the needed corrections for every event  $Q$ -vector. There are three stages for the correction: recentering, twisting, and rescaling of the  $Q$ -vectors.

The non-corrected  $Q$ -vector components can be described with the help of constants  $A_n$ ,  $\Lambda_n$ , and the mean  $\bar{Q}$  each of which represent an aspect of non-



(a) Comparison between the inputted flow coefficient versus calculated flow coefficients according to the two and three subevent methods. (b) Comparison for the resolution parameter between two and three subevent methods. Also shown are the measured ALICE results for the V0 resolution.

FIGURE 3.6 Validation graphs we created for the flow coefficient calculations and comparison between the two and three subevent methods. Also included for comparison is the measured resolution of V0-C from [193]. Note that the binning between the simulation and the published measurement is different.

symmetricity of the  $X$ - $Y$  distribution

$$X_n = \bar{X} + A_n^+ (\cos(n\Psi_n) + \Lambda_n^+ \sin(n\Psi_n)) \quad (3.20)$$

$$Y_n = \bar{Y} + A_n^- (\sin(n\Psi_n) + \Lambda_n^- \cos(n\Psi_n)). \quad (3.21)$$

By manipulating these equations so that the non-symmetric components of the equations disappear, we have a corrected  $Q$ -vector distribution.

Recentering of the  $Q$ -vector takes the average of the whole distribution and shifts each point to be zero

$$X'_n = X_n - \bar{X}_n \quad (3.22)$$

$$Y'_n = Y_n - \bar{Y}_n. \quad (3.23)$$

Twist correction will rotate the  $Q$ -vector so that if the vector is in an elliptic shape, it faces either left to right or top to bottom directions, not diagonally. This is important during the final correction. The twist is done with

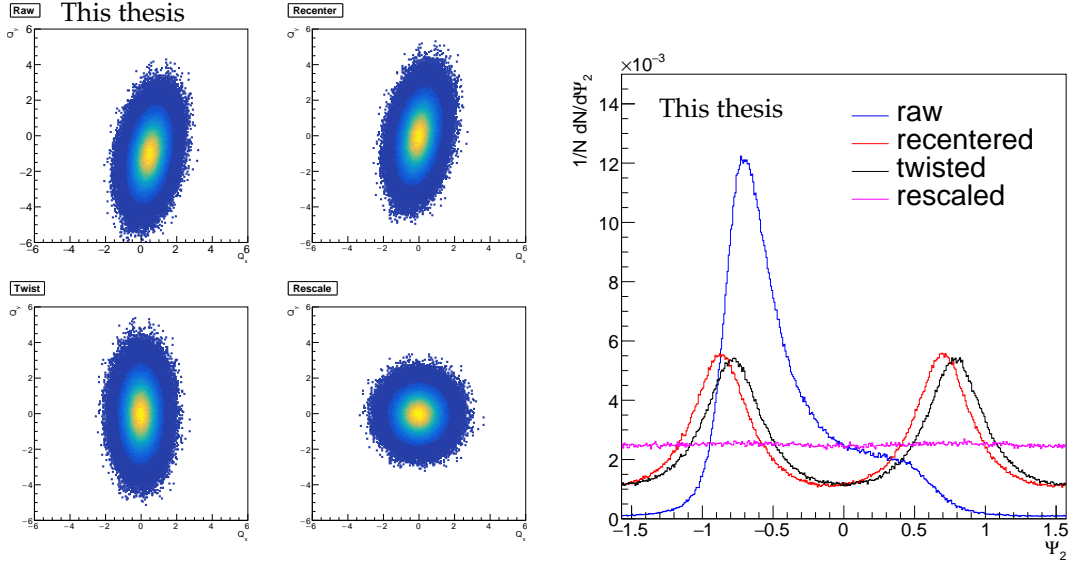
$$X''_n = \frac{X'_n - \Lambda_n^- Y'_n}{1 - \Lambda_n^- \Lambda_n^+} \quad (3.24)$$

$$Y''_n = \frac{Y'_n - \Lambda_n^+ X'_n}{1 - \Lambda_n^- \Lambda_n^+}, \quad (3.25)$$

which removes the  $\Lambda_n$  term of the equations (3.20) and (3.21).

Finally, the stretching of the  $Q$ -vector in the  $x$  or  $y$ -axis direction is corrected





(a) The  $Q$ -vector plane in different phases of the correction procedure. From left to right and top to bottom are the following  $Q$ -vector distributions: uncorrected, recentered, twisted, and rescaled. Each correction is done on top of the previous one. (b) The event plane angle in each stage of the  $Q$ -vector correction process.

FIGURE 3.7 Toy MC visualization of the  $Q$ -vector corrections. Part of the validation we performed for the FIT event plane studies.

with a simple scaling

$$X_n''' = \frac{X_n''}{A_n^+} \quad (3.26)$$

$$Y_n''' = \frac{Y_n''}{A_n^-}. \quad (3.27)$$

The different phases of the corrections are depicted in figure 3.7, and as one can see, the outcome is a symmetrical zero-centered distribution. In the right-hand side part of the figure the  $\Psi_2$  distribution is also drawn to further point out how the  $Q$ -vector corrections flatten the  $\Psi_2$  distribution. Figure 3.7 was made for the specific purpose of demonstrating these corrections by sampling a 2D Gaussian distribution. There are different ways to calculate  $A_n^\pm$  and  $\Lambda_n^\pm$ , and one of them is to use the random subevent method as introduced in [187].

### 3.3.5 AMPT MC generator with full FIT detector simulation

To estimate the performance of the FIT to calculate the event plane for each event, we used the latest standalone AMPT [137, 194] MC event generator to simulate full heavy ion events, which include realistic collective flow effects across many centralities [186]. For the simulation, we set the center-of-mass energy to

$\sqrt{s_{\text{NN}}} = 5.5$  TeV as that is the designed energy during run 3 of the LHC physics program. A center-of-mass energy of 13.6 TeV for pp collisions was reached at the beginning of LHC Run 3, which amounts to  $\sqrt{s_{\text{NN}}} = 5.36$  TeV for the future Pb–Pb collisions. We studied that the energy difference had no meaningful effect on the outcome.

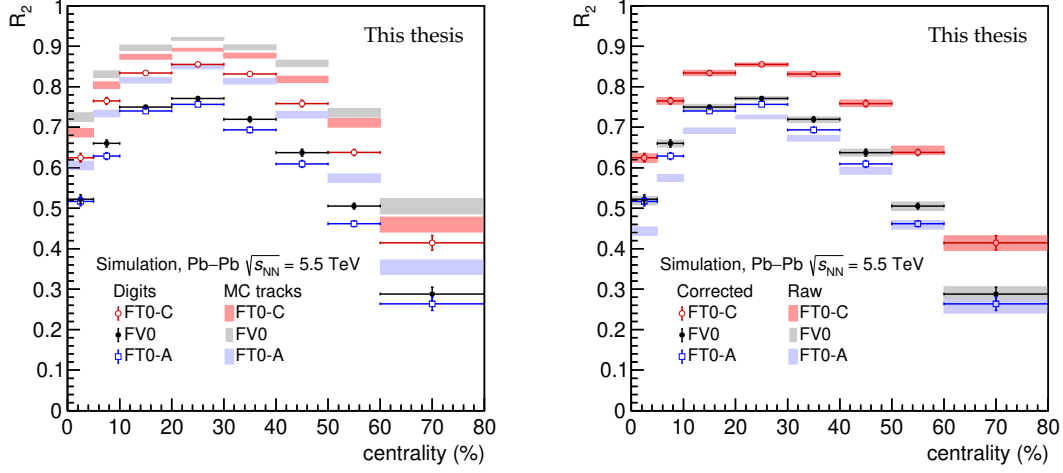
The AMPT was set to generate a random orientation for the reaction plane for each collision with the string melting setting turned on. The AMPT parameter `PARJ(41)`, used in Lund symmetric splitting function as parameter  $a$ , was set to 0.3 as it fits the ALICE measurements better than the default value [195]. AMPT can be set to generate events in a specific impact parameter range, so to generate ALICE data comparable centrality classes, we ran AMPT with impact parameters corresponding to ALICE 5.5 TeV Pb–Pb centrality classes according to reference [196]. Otherwise, the run was done with default settings as given in [194]. The exact settings of the AMPT simulation can be found in appendix C.1.

After AMPT had generated events, the events were forwarded to the ALICE GEANT3 [153] software to simulate the detector response to the particles. The event simulation included the beam pipe, the inner tracking system, the new muon forward tracker, and the FIT. The digitizing of the signal was also simulated, although with a reduced interaction rate, to minimize any pileup effects for this analysis.

The event plane resolution was calculated for FV0, FT0-A, and FT0-C using the three-subevent method, like in the toy MC model. Each subdetector was selected as subevent A, and TPC split in half as subevents B and C. The  $v_n^{\text{obs}}$  from equation (3.5) is calculated with stable charged hadrons from AMPT in the TPC acceptance in transverse momentum range of  $0.2 \text{ GeV} < p_T < 5.0 \text{ GeV}$ , and the event plane calculated from each FIT subdetector.

The detector simulation will affect the results in a multitude of ways, such as the limited granularity of the detector, secondary interactions in the detector material, and particle decays, for example. We quantified these detector effects by comparing the resolution from the true MC information in the detector acceptances to the digitizer values. The digitizer informs how much signal each sector has received, and that is regarded as a sum of particles inside a sector. The center point of each sector is assigned as a location for the signal, creating a granular output in the process. A comparison between the MC truth output and the digits is seen in figure 3.8a. Here the resolution of FV0 drops the most during the digitizing. The FV0 has the highest resolution when calculated from the MC truth, but it is dropped to be just above the resolution of FT0-A, which consistently has the lowest values. FV0 has the highest acceptance out of the subdetectors, so the resolution being the highest for the true MC information is understandable. However, the large drop in the resolution is not easy to interpret. This could be due to the relatively large-sized sectors of the subdetector as seen in figure 3.3 depicting the subdetectors.

The  $Q$ -vectors were corrected for all the results as explained in section 3.3.4. The effect of the correction was tested by comparing results with and without the correction in figure 3.8b. FT0-C and FV0 seem to have almost no effect with or



(a) Event plane resolution calculated from (b) Event plane resolution with and without  $Q$ -vector corrections.  
MC tracks and digitizer information.

FIGURE 3.8 Studies of how the full detector simulation and the  $Q$ -vector corrections affect the event plane resolution for each detector.

without the corrections, but FT0-A, on the other hand, does benefit quite a bit. We studied that removing the beam pipe from the simulation increases the raw FT0-A resolution by approximately 3% in mid-rapidity (20–30%), but also removing the FV0, the resolution increases approximately a total of 24%, which is a significant improvement. FV0 is located right before the FT0-A, so the effect on FT0-A resolution makes sense. FV0 is split into two parts by the  $y$ -axis, separated by aluminum, which turned out to be a significant source of secondary interactions, thus modifying the  $Q$ -vector distribution.

As the flow of the event is the same for each subdetector, the  $v_2$  for each subdetector should be the same even though the detectors have different resolutions. For each subdetector, the event plane was used to calculate  $v_2^{\text{obs}}$  from charged hadrons in TPC acceptance and then corrected with event plane resolution to  $v_2$  as shown in equation (3.19). For additional comparison besides the subdetectors, an ideal resolution was calculated using the primary particle information, that is, the original AMPT particles, with an acceptance of  $-6 < \eta < -1$  and  $1 < \eta < 6$  for the subevent A in the three-subevent method, while retaining the subevent C and D as the TPC acceptance split in half. This was because even though the true value for the reaction plane would be available in the AMPT output, it was not used in the simulation and thus not saved in the output.

Figure 3.9 shows the flow coefficient  $v_2$  for full detector simulation with AMPT+GEANT. The resolution, as was seen in figure 3.8b, is closely comparable, or better than, with the FIT predecessor V0 [193]. Each subdetectors agree with the other on the  $v_2$  flow coefficient, but they all overestimate the ideal measurement. The nature of this overestimation is not certain, but the ATLAS [197], CMS [198], and PHOBOS [199] show that the flow coefficient  $v_2$  is slightly decreased in

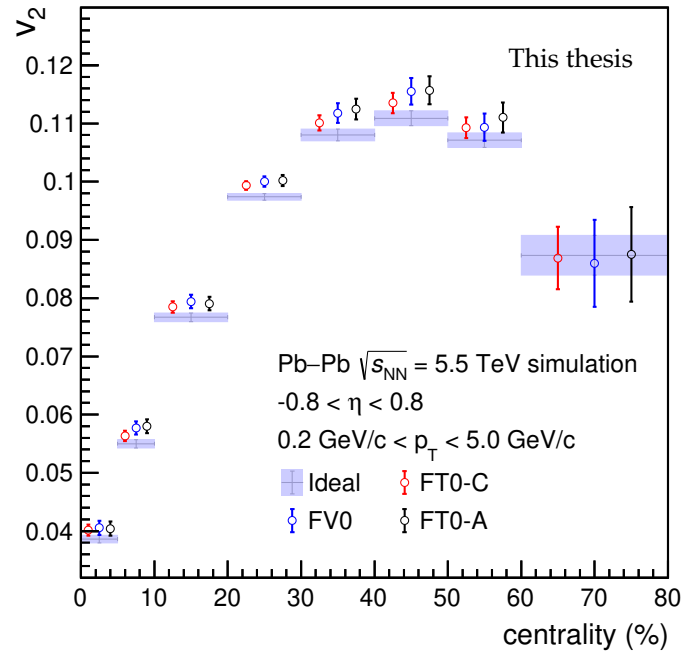


FIGURE 3.9 Recovery of the elliptic flow  $v_2$  in the full detector simulation for each sub-detector. Particles with ideal performance were used to calculate the reference flow from an artificially large acceptance, marked as “Ideal” in the figure. See text for more details.

the forward and backward directions indicating that the large non-central region used for the ideal case could result in a slightly smaller flow coefficient. AMPT with string melting realistically describes the flow in forward directions when compared to data [137].

## 4 EVENT AND TRACK SELECTION

The proton–proton and proton–lead data gathered for the main analysis of this thesis was procured with the ALICE detector system in the years 2017 and 2016, respectively, both with the center-of-mass energy of 5.02 TeV. The asymmetric composition of the proton–lead system results in asymmetric beam energies as both beams in the LHC are guided with the same magnets. The lead ion used in the experiments has 208 nucleons, of which 82 are protons with a positive coulomb charge. This means that the charge to atomic number ratio is  $Z/A = 82/208$ , whereas for a single proton, it is one. The consequence is that if the proton can be accelerated to energy  $E_a$ , the lead can only go up to  $E_b = E_a \frac{Z}{A}$ . By a very good approximation  $1 \ll m/E$  for the beams, the center-of-mass energy can be written for a proton–lead beam as

$$\sqrt{s_{\text{NN}}} = 2E_a \sqrt{\frac{Z}{A}}. \quad (4.1)$$

The proton beam was run with 4 TeV energy in the laboratory frame, and the lead ion with 1.58 TeV per nucleon [200, p.439], which will result in a center-of-mass energy of approximately 5.02 TeV. This results in a rapidity shift of  $\Delta y = 0.465$  in the direction of the proton projectile velocity vector [201], and the effect is seen, for example, when comparing forward or backward regions of p–Pb collisions with symmetrical pp collisions [202].

### 4.1 Visible cross section related to ALICE minimum bias trigger

The most commonly used minimally biased triggers in ALICE are V0-AND or V0-OR. The names refer to the V0 detector and a logical AND and OR for hits in the forward AND/OR backward direction of V0. In addition, the V0-OR trigger requires a hit in the innermost detector SPD as well [203]. For this trigger, ALICE has measured minimally biased cross section  $\sigma_{\text{V0-AND}}$ , often called the visible cross section, with a van Der Meer scan [204].

As was prefaced in section 2.1, the visible cross section does not describe the inelastic cross section completely. To calculate the visible cross section efficiency, ALICE used Pythia6 and PHOJET MC event generators tuned to replicate the measured rapidity gaps. The visible cross section is simulated with the MC by triggering the MC with ALICE V0-AND and V0-OR triggers. The cross section efficiency for V0-AND and V0-OR is then calculated by the ratio of inelastic cross section to the minimum bias cross sections. This way ALICE has calculated an efficiency of  $0.742^{+0.050}_{-0.020}$  for V0-AND, and  $0.852^{+0.062}_{-0.030}$  for V0-OR triggers at  $\sqrt{s} = 7$  TeV pp collisions [101]. To validate these efficiencies, we can calculate

$$\frac{\sigma_{\text{V0-OR}}}{\sigma_{\text{V0-AND}}} = \frac{\epsilon_{\text{V0-AND}}}{\epsilon_{\text{V0-OR}}} \quad (4.2)$$

with both the MC and measured data. By measuring the ratio with data, we achieve the double ratio of  $0.8727 \pm 0.0001$ , and the double ratio between the MC efficiencies is  $0.871 \pm 0.007$ , which means they agree with each other within the margin of error [101].

In this thesis I have used the minimum bias trigger V0-AND, for which ALICE has measured a cross section of  $50.87 \pm 0.04 \pm 0.92$  mb for pp [205] and  $2090 \pm 70$  mb for p-Pb collisions [206] at  $\sqrt{s_{\text{NN}}} = 5.02$ . Statistical and systematic uncertainties are shown separately for the pp collisions, while the systematic uncertainties dominate in p-Pb collisions. For this work I analyzed 816 M triggered pp events and 626 M triggered p-Pb events.

Even though the visible cross section differs from the inelastic cross section, the ratio of the cross section of a process  $r$  over a number of triggered processes  $r$  is constant. To show that this is true, I will start by writing a cross section for process  $r$  open

$$\sigma_r = \frac{W_r}{\mathcal{L}}, \quad (4.3)$$

where  $W_r$  is the reaction frequency  $W_r = N_r/\Delta t$ , and  $\mathcal{L}$  is the instantaneous luminosity of the beam [99]. Luminosity is a property of the experimental setup, whereas the rate depends on the process itself. Now it is straightforward to see that

$$\frac{\sigma_{\text{V0AND}}}{N_{\text{V0AND}}} = \frac{N_{\text{V0AND}}/\Delta t}{\mathcal{L}N_{\text{V0AND}}} = \frac{N_{\text{inel}}/\Delta t}{\mathcal{L}N_{\text{inel}}} = \frac{\sigma_{\text{inel}}}{N_{\text{inel}}}. \quad (4.4)$$

## 4.2 Vertex and track reconstruction

The detector system outputs signals which can be used to calculate locations where a particle could have traversed. To use this information meaningfully, the tracks left by the particles need to be reconstructed by tracking multiple signals to form a continuous track, and this is needed to be done for every plausible track in the detector. For this, a combination of detectors and tracking algorithms is used.

For the charged particles, from which the jets and dijets are reconstructed in this thesis, the main detector components are the TPC and ITS. As explained in

the chapter 3, TPC is excellent for tracking thousands of tracks simultaneously as it was designed specifically for heavy ion collisions [207].

Before the track-finding, a preliminary determination of the interaction vertex is done using the SPD layers of the ITS. The vertex is defined as a point of space where a maximum number of tracklets converge. A tracklet is a line that is connected by a cluster in each of the two layers of the SPD. This calculation is repeated multiple times to find possible secondary vertices or pileup events. Each iteration discards clusters that have already contributed to some other vertex. In case the algorithm does not find a single vertex this way, a vertex is chosen to be located in the beam axis with a  $z$ -axis location chosen with the most points of closest approach of the tracklets in the event [203].

After a preliminary vertex is found, the tracking process starts. Tracking happens in three stages, as shown in figure 4.1. The first phase starts to look at the outer layers of the TPC for tracks, going inwards by finding the nearest cluster inside a certain proximity cut. After the track reaches ITS, it continues the propagation using the TPC track information as a seed for the ITS track-finding algorithm, which works the same way as in the TPC. After tracks are propagated to the innermost layer of ITS, they are interpolated to the point of closest approach to the preliminary interaction vertex, which then serves as a starting point for the second stage.

The second stage traces the track from the preliminary interaction point toward the outer layers like as in the first stage. This time the information from the first stage is used to perform fits with a Kalman filter [209]. During the second stage, the track is extended beyond the TPC for the purposes of outer detectors, which are not used during the tracking procedure.

The third stage starts again from the outer layer of the TPC and proceeds inwards, just like in the first stage. The tracks are refitted with the previously found clusters, and the track properties are calculated, like position, direction, curvature, and so on. The majority of the tracks define the primary interaction vertex, with a minority born from secondary vertices, which are checked for possible long-lived resonances. Some secondary vertices can be caused by pileup collisions and are rejected for this analysis.

For the analysis, the SPD vertex is required to be found as this greatly improves the resolution of tracks reconstructed only with TPC information. The primary vertex and the SPD vertex need to be within 0.5 cm of each other if a primary vertex is found. If the SPD vertex was reconstructed only for  $z$ -axis, the resolution of the fit needs to be good enough, or else the event is rejected. The primary vertex of the collision needs to be within 10 cm of the center of the detector for good quality.

Each vertex besides the primary vertex is checked for the probability of it being pileup. Pileup vertices need to have enough contributors, be located over three sigma away from the primary vertex in  $z$ -axis direction, and be within the overlap area of the beams. pp collisions are additionally checked for unnaturally high amounts of SPD clusters when compared to the tracklets, which would imply an additional source for clusters beside the primary vertex.

The information provided by the ITS improves the resolution of the tracks significantly, so these tracks are used whenever possible. The SPD layers of the ITS have had inactive modules during the ALICE data taking, causing uneven distribution of tracks calculated with both ITS and TPC. In order to achieve a more uniform distribution of particles, tracks reconstructed only from TPC information can be used whenever ITS cannot participate. Even though ITS has not been used in the reconstruction for all tracks, the SPD vertex is still required nevertheless. This combination of two classes of tracks is called the hybrid track selection.

To assure hybrid tracks of acceptable quality, some quality assurance cuts are made. The tracks are required to have at least 70 TPC clusters hit out of the maximum of 159. This means that some of the rows can be skipped. The fit of the track is checked by requiring  $0.1 < \chi^2/\text{TPC clusters} < 4.0$ . The distance of the closest approach to the primary vertex of the track needs to be below 3.2 cm in the  $z$  direction and 2.4 cm in the  $x$ - $y$  plane. ALICE re-examines these cuts from time-to-time and mines the raw data files to create analysis objects which can be used for analysis. The cuts I have used for this analysis are known as pass 1.

The  $p_T$  resolution of the tracks in ALICE is optimal between 150 MeV and 100 GeV. Tracks below 150 MeV are not used in the analysis, as they curve too much in the magnetic field. Tracks over 100 GeV suffer from lowered  $p_T$  resolution as the particle curving is insufficient. These tracks over 100 GeV are used in the event analysis as anti- $k_T$  [210] jets are sensitive to high  $p_T$  tracks, but jets containing constituents with over 100 GeV are removed from the analysis.



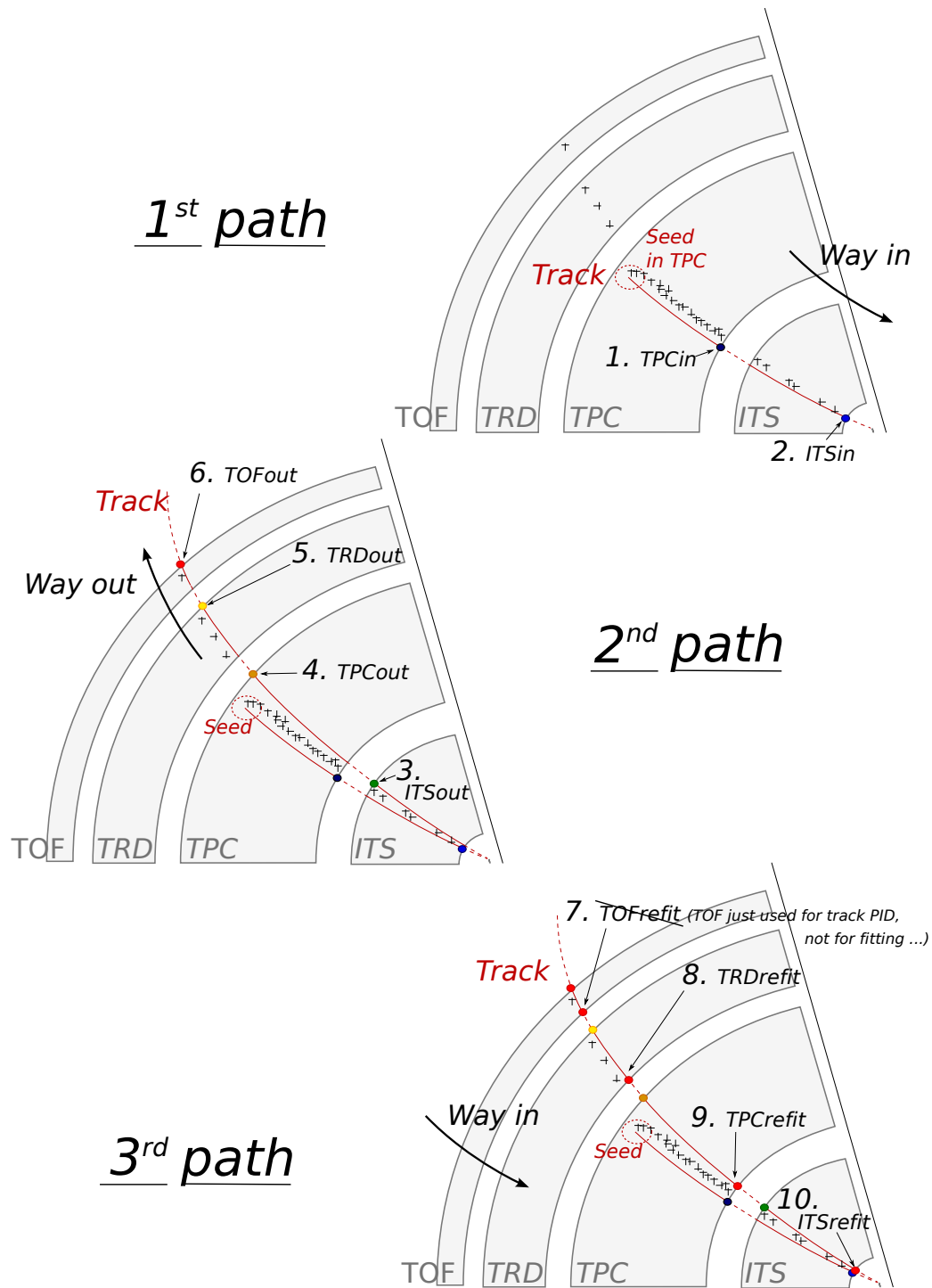


FIGURE 4.1 A step-by-step schematic of the ALICE tracking process. Each path describes the different stages of track reconstruction in ALICE. The numbers from 1 to 10 refer to bits that are activated during the fitting process. Figure from [208], reprinted with permission from CERN.

### 4.3 Vertex reconstruction efficiency

In this analysis, I use minimum bias triggered events to gather dijet invariant mass data. Most of these events have a proper primary vertex calculated either from hits in ITS or a combination of ITS and TPC, as was detailed in section 4.2. This requires that there need to be enough tracks for the vertex to be reconstructed [203]. Some of the events are triggered with a minimum bias trigger but have too few tracks for a vertex reconstruction. The events where the vertex reconstruction was not successful are left out of the analysis. Hence, the number of events used in the analysis needs to be corrected so that it matches the number of minimum bias events. I can write the total number of events in the vertex  $z$  acceptance  $z_{\text{vtx}} < 10$  cm as

$$N_{<10 \text{ cm}}^{\text{tot}} = N_{<10 \text{ cm}}^{\text{w/vtx}} \frac{N_{<10 \text{ cm}}^{\text{tot}}}{N_{<10 \text{ cm}}^{\text{w/vtx}}} \approx N_{<10 \text{ cm}}^{\text{w/vtx}} \frac{N^{\text{tot}}}{N_{<10 \text{ cm}}^{\text{w/vtx}'}} \quad (4.5)$$

where the approximation is an assumption that events without vertex are distributed in the same way as the events with vertex. Now I define the ratio of events without vertex divided by the total number of events with or without vertex as a vertex reconstruction efficiency

$$\epsilon_{\text{vtx}} \equiv \frac{N_{<10 \text{ cm}}^{\text{w/vtx}}}{N^{\text{tot}}}, \quad (4.6)$$

so that I can correct the number of events analyzed in the analysis  $N_{<10 \text{ cm}}^{\text{w/vtx}}$

$$N_{<10 \text{ cm}}^{\text{tot}} \approx \frac{N_{<10 \text{ cm}}^{\text{w/vtx}}}{\epsilon_{\text{vtx}}}. \quad (4.7)$$

I measured the vertex reconstruction efficiency for pp as 0.949 and for p–Pb 0.985. The higher efficiency of p–Pb is understandable due to a higher number of tracks per event, which increases the quality of the vertex reconstruction.

## 5 JETS

### 5.1 Jet definition

A high-energy parton, born in a relativistic collision, will fragment and create a well-collimated shower of particles. Algorithms have been developed to connect the particles from the shower to the original parton, although no algorithm can perfectly recreate the original information. Among the most commonly used jet definitions in high energy physics are the  $k_T$  [211] and anti- $k_T$  [210] algorithms. The implementation of the  $k_T$  and anti- $k_T$  algorithms that I have used in this thesis is by the FastJet library [1]. The algorithms define a distance between any two 4-momenta

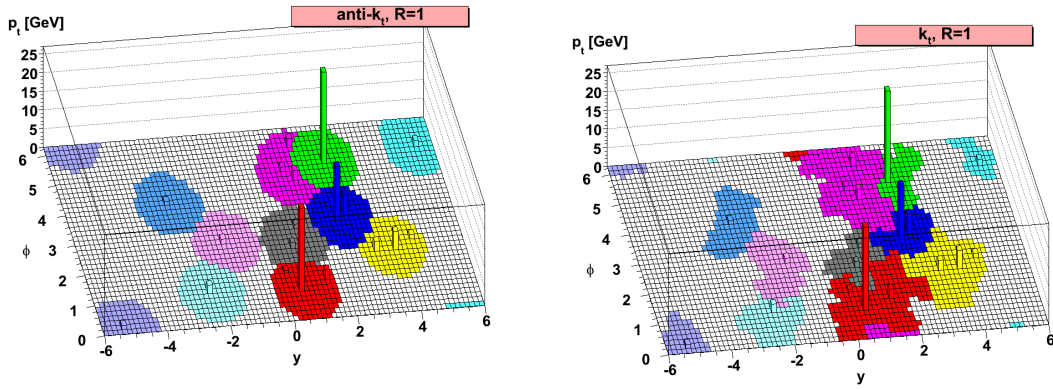
$$d_{ij} \equiv \min \left( p_{T,i}^{\pm 2}, p_{T,j}^{\pm 2} \right) \frac{\Delta R_{ij}^2}{R^2} = d_{ji}, \quad (5.1)$$

where inside the minimum function “+” is used for the  $k_T$  algorithm and “-” for the anti- $k_T$  algorithm,  $\Delta R_{ij}^2 = \Delta\phi_{ij}^2 + \Delta\eta_{ij}^2$  which is distance in the  $\eta$ - $\phi$  plane, and  $R$  is the resolution parameter for the algorithm. In addition, each 4-momenta has a distance to the beam defined as

$$d_{B,i} = p_{T,i}^{\pm 2}, \quad (5.2)$$

where again “+” is for  $k_T$  algorithm and “-” is for anti- $k_T$  algorithm. In some studies, Cambridge/Aachen jet algorithm [212] is used where equation (5.1) is reduced to  $\Delta R_{ij}^2/R^2$  and the beam distance is always 1. This thesis focuses on the  $k_T$  and anti- $k_T$  algorithms. For each event, the FastJet clustering considers all distances  $d_{ij}$  and  $d_{B,i}$  and finds the smallest. If the smallest distance is  $d_{ij}$ , the 4-momenta  $i$  and  $j$  are combined, and if the shortest distance is  $d_{B,i}$ , the 4-momentum  $i$  is declared as a jet and is left out for the rest of the clustering. The clustering is continued until all 4-momenta are combined and declared as jets.

As can be seen in the equation (5.1), these two algorithms start the reconstruction from different ends of the  $p_T$  spectrum, as the  $k_T$  algorithm clusters low  $p_T$  particles first, and anti- $k_T$  algorithm, on the other hand, high  $p_T$  particles. This will affect the shape of the jet area in the  $\eta$ - $\phi$  plane, which is demonstrated in



(a) Different jet areas demonstrated by the anti- $k_T$  reconstruction algorithm. (b) The  $k_T$  reconstruction algorithm.

FIGURE 5.1 A schematic demonstrating the different jet area shapes for anti- $k_T$  and  $k_T$  algorithms. Used with permission of Springer Nature BV, from [210]; permission conveyed through Copyright Clearance Center, Inc.

figure 5.1. The figure shows how the anti- $k_T$  algorithm creates very round areas around the highest  $p_T$  tracks. In case of jet overlap it favors the highest  $p_T$  to cluster first. The  $k_T$  algorithm jets have no clear shape to the jets, but instead, each is shaped somewhat differently. This is possible as the clustering starts from small  $p_T$  particles first, which means that the center of the jet drifts easier, thus creating jets with various shapes.

There are several recombination schemes for combining two 4-momenta into one. The most straightforward way is the E-scheme, in which the 4-momentum vectors of particles are summed. This retains the mass of the original particles and also generates the invariant mass of the system of two 4-momentums. To experimentally identify a mass of a particle, the particle itself needs to be identified. This is challenging when the energy of the particle is very high or very low. As such, the masses are usually left out or assigned the mass of a pion, as pions are the most numerous in an average event. Because my analysis is highly dependent on high-energy particles, I have used the  $p_T$ -scheme, where the recombination starts by scaling each 4-momentum so that the energy is equal to the 3-momentum amplitude, making the 4-momenta massless. Then combining the information of two 4-momentum is done by

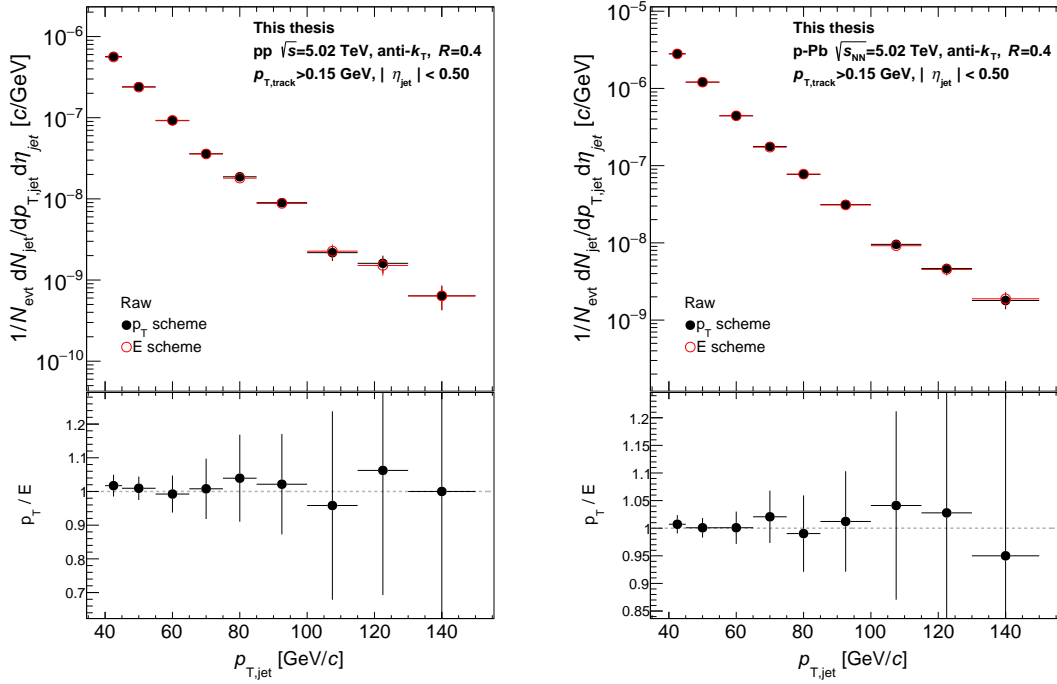
$$p_{T,combined} = p_{T,i} + p_{T,j} \quad (5.3)$$

$$\phi_{combined} = \frac{p_{T,i}\phi_i + p_{T,j}\phi_j}{p_{T,i} + p_{T,j}} \quad (5.4)$$

$$\eta_{combined} = \frac{p_{T,i}\eta_i + p_{T,j}\eta_j}{p_{T,i} + p_{T,j}}. \quad (5.5)$$

This way, the resulting 4-momentum is still massless. The location of the jet will shift during the reconstruction, but the transverse momentum will be a scalar sum of its constituents' transverse momenta.

The difference between the E-scheme and  $p_T$ -scheme can be seen in figure 5.2, where I have plotted the jet transverse momentum with both schemes. The



(a) Proton–proton collisions

(b) Proton–lead collisions

FIGURE 5.2 A comparison of jet reconstruction schemes for raw jets without any manipulations like background subtraction.

difference in jet  $p_T$  is small, which is natural as the transverse momentum is not dependent on the mass of the jet. If one were to study the single jet mass, like in reference [213], the analysis would have to be made with an E-scheme, as the other schemes do not retain masses of the single jets.

## 5.2 Background subtraction

The study of jets in hadron collisions faces the challenge of the underlying event. The underlying event in jet studies refers to all the particles not produced by the original high-energy partons which form the jets [214]. Each collision of hadrons always has some underlying event, especially when colliding ions. Hard interactions such as jets are a rare phenomenon as the production of jets at high energies drops as a power law. Thus, the particles of the underlying event mostly have a small transverse momentum and as such, often called the soft background. It is usually impossible, or at least extremely challenging, to discern which particle arises from the original parton and which is not. That is why many methods estimate the background density of the whole event.

The strength of the underlying event is usually denoted with the letter  $\rho$ , and  $\rho_m$ , for the  $p_T$  density and mass density of the event, respectively. A common

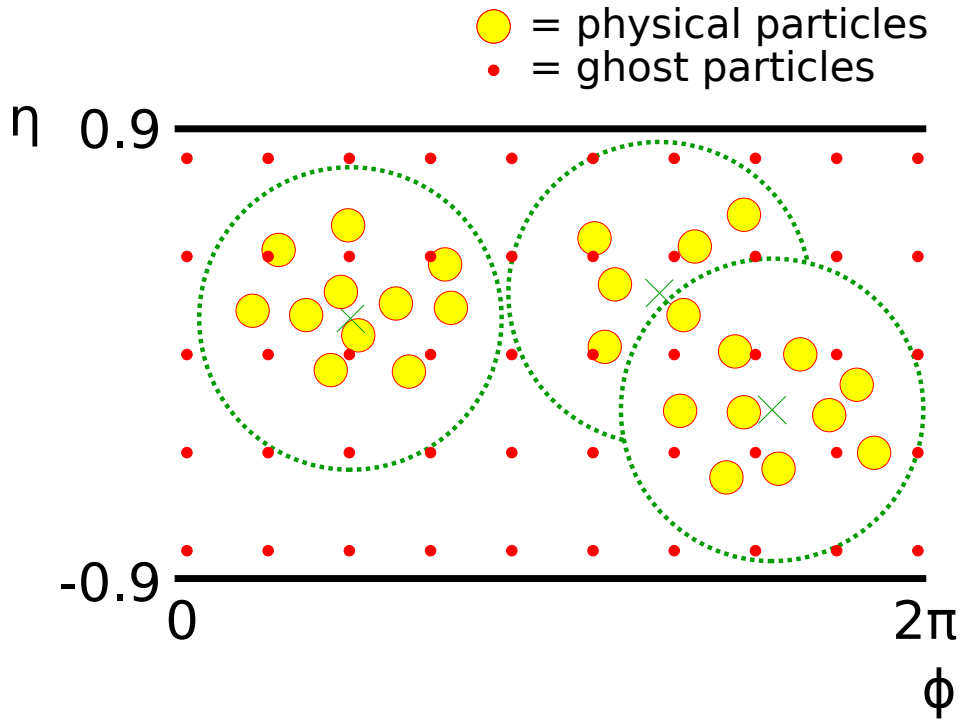


FIGURE 5.3 A simplified schematic to demonstrate how infinitesimally energetic evenly distributed ghost particles are used to calculate the area of each jet. Each particle will be included in some jet; in this figure, the jets with physical particles are shown. The area of each jet would be proportional to how many ghost particles are included in the jet. In the real calculation, the density of the ghosts would be significantly higher.

way to define these [215] is

$$\rho = \text{median}_{k_T \text{ jets}} \left\{ \frac{p_{T,\text{jet}}}{A_{\text{jet}}} \right\}, \quad (5.6)$$

$$\rho_m = \text{median}_{k_T \text{ jets}} \left\{ \frac{m_{\text{jet}}}{A_{\text{jet}}} \right\}, \quad (5.7)$$

where the median of all of the  $k_T$  jets is taken, excluding the two leading jets. The two leading jets most likely do not originate from the underlying event and should not be accounted for. This method is implemented in the FastJet package and is thus referred to as the FastJet default method in this thesis. The  $k_T$  jets are used to estimate the background as  $k_T$  jets are described as having soft-adaptable boundaries [210]. This refers to the fact that the shape of the jet is sensitive to the soft particles whereas the anti- $k_T$  creates regular shapes around the most energetic particles, as demonstrated in the figure 5.1.

As the area of jets in the  $\eta$ - $\phi$  plane is needed to calculate the underlying event density, one needs a definition. A common way to do this is to add artificial particles to the event with infinitesimally small energy, dubbed as “ghosts”. The ghost particles are added to the event evenly in the  $\eta$ - $\phi$  plane and are included

in the clustering of jets along the physical particles. As every particle will be included in some jet, and a well-known total amount of ghosts are spread evenly in the event, by counting the number of ghosts in a jet, one can calculate the area of the jet. This is demonstrated in a simplified schematic in figure 5.3 where jets with physical particles are shown. Each of these includes some amount of ghost particles, and the area of each jet will be proportional to the number of ghosts included in the jet. In the real calculation, the density of the ghost particles is much higher. Specifically for this analysis, each ghost has an area of 0.005, which means that approximately 2260 ghosts are distributed evenly in the central acceptance of  $|\eta| < 0.9$ .

The background estimation, as shown in equations (5.6) and (5.7), has a problem when studying collisions with a much weaker underlying event than in a typical heavy ion collision, such as proton–lead, or proton–proton collisions. If I happen to have an event with more than half of the underlying event  $k_T$  jets being empty, which means that they are formed solely by the ghost particles, the  $\rho$  and  $\rho_m$  will be zero. This will create a discontinuity between the bin, including zero, and other bins. Because of this, a method that takes this into account was developed by the CMS collaboration [216], sometimes also called the sparse event method. In this method, the underlying event densities are defined as

$$\rho = \text{median}_{\text{real } k_T \text{ jets}} \left\{ \frac{p_{T,\text{jet}}}{A_{\text{jet}}} \right\} \times C, \quad (5.8)$$

$$\rho_m = \text{median}_{\text{real } k_T \text{ jets}} \left\{ \frac{m_{\text{jet}}}{A_{\text{jet}}} \right\} \times C, \quad (5.9)$$

where in the median, only  $k_T$  jets with any amount of real particles are included, and the empty portion of the event is taken into account with the coefficient  $C$ , which is defined as

$$C = \frac{A_{\text{real jets}}}{A_{\text{all } k_T \text{ jets}} \Big|_{|\eta_{\text{jet}}| < 0.5}}, \quad (5.10)$$

where it is easy to see that this method will approach the previous one asymptotically in the case where all jets have at least one real particle. The  $k_T$  jets used to calculate this ratio must be inside the acceptance. Figure 5.4 shows the coefficient  $C$  for both pp and p–Pb collisions, showing how pp collisions are generally emptier than p–Pb events. There is a significant discontinuity in the p–Pb  $C = 1.0$ . The last bin only includes events where every  $k_T$  jet has a real particle included, and if even one of the  $k_T$  jets is empty, this value will drop significantly more than the bin width, which is 0.01 in this case, thus creating a discontinuity in the last bin.

In figure 5.5, I have plotted the underlying event density in 5.02 TeV pp and p–Pb collisions with both introduced methods. The FastJet default method has a fairly large discontinuity between the first bin and the ones after, whereas the CMS method is relatively smooth until at high  $\rho$  values where the ALICE data runs out of events. The CMS method seems to estimate the background slightly higher when compared to the FastJet default method.

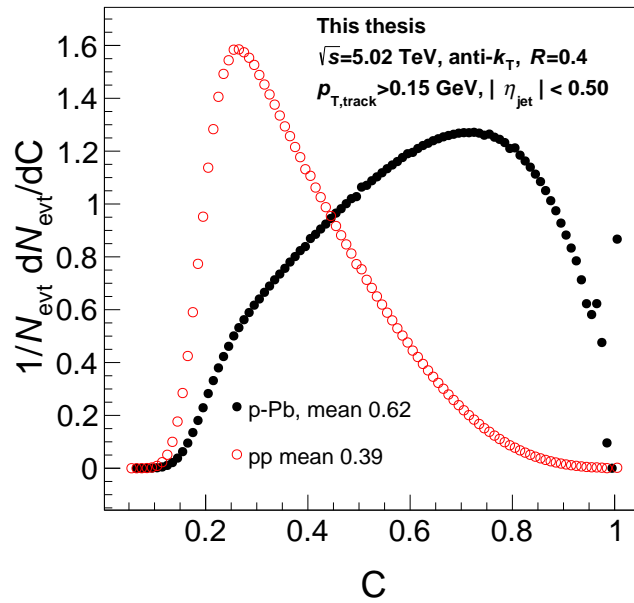
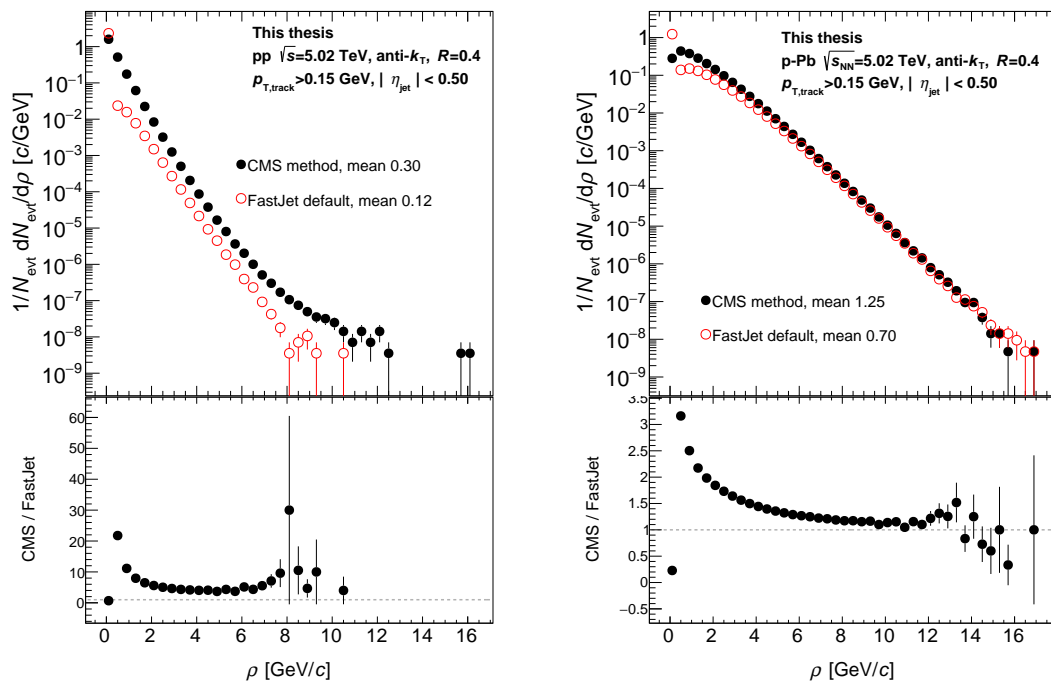


FIGURE 5.4 The coefficient  $C$  as described in equation (5.10) for both pp and p-Pb. The pp collisions are emptier when compared to p-Pb.

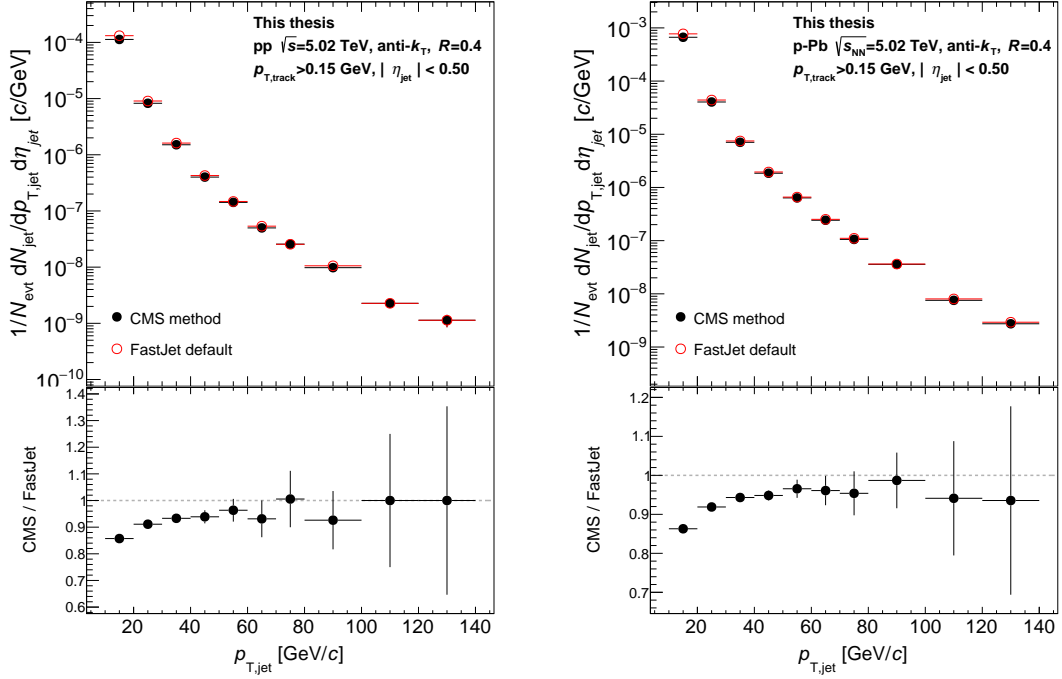


(a) Proton-proton collisions

(b) Proton-lead collisions

FIGURE 5.5 Comparison of two different methods of calculating the average  $p_T$  density of an event for a 5.02 TeV pp collision.





(a) Proton–proton collisions

(b) Proton–lead collisions

FIGURE 5.6 The background subtracted jet spectrum with the background density estimated using CMS and FastJet default methods. The background was subtracted using the equation (5.11).

Subtracting the underlying event from the jet transverse momentum is a straightforward calculation

$$p_{T,\text{corr}} = p_{T,\text{raw}} - \rho \times A_{\text{jet}}, \quad (5.11)$$

where the background density times the area of the jet is used to subtract the underlying event from the raw jet  $p_T$ . To see the effect of the background estimation method on a background subtracted single jet  $p_T$  spectrum, a comparison was drawn in figure 5.6. As the correction relative to the jet  $p_T$  gets smaller in high transverse momentum jets, also the difference between the two subtraction methods lessens.

When using an observable which is dependent on the whole 4-momentum of the jets, like the dijet invariant mass, the background subtraction should be done for the 4-momentum of the jet instead of merely jet  $p_T$

$$p_{\text{corr}}^\mu = p_{\text{raw}}^\mu - \left[ (\rho + \rho_m) A_{\text{jet}}^E, \rho A_{\text{jet}}^x, \rho A_{\text{jet}}^y, (\rho + \rho_m) A_{\text{jet}}^z \right], \quad (5.12)$$

where  $A_{\text{jet}}^\mu$  is the jet area 4-vector as defined by the FastJet program [1]. To explain the area 4-vector, I can start by defining another helpful 4-vector  $n^\mu$ . A

4-momentum  $p^\mu$  can be written as

$$p^\mu = (E, p_x, p_y, p_z) \quad (5.13)$$

$$= (m_T \cosh y, p_T \cos \phi, p_T \sin \phi, m_T \sinh y) \quad (5.14)$$

$$= p_T \left( \sqrt{1 + \left(\frac{m}{p_T}\right)^2} \cosh y, \cos \phi, \sin \phi, \sqrt{1 + \left(\frac{m}{p_T}\right)^2} \sinh y \right), \quad (5.15)$$

which can be further simplified for massless particles, like the artificial ghost particles, to

$$p^\mu = p_T (\cosh \eta, \cos \phi, \sin \phi, \sinh \eta) \quad (5.16)$$

$$\equiv p_T n^\mu (\phi, \eta). \quad (5.17)$$

Now the area 4-vector can be written as

$$A^\mu = \int \int_{A_{\text{jet}}} d\phi d\eta n^\mu (\phi, \eta), \quad (5.18)$$

where the jet area over  $\eta$ - $\phi$  plane is integrated. This means a sum over all the ghost particles in the jet with an extra coefficient  $n^\mu$ .

It is worth noting that when inspecting the 4-momentum area in a transverse plane, with the assumption of small  $R$  and massless constituents

$$A^\mu \approx \pi R^2 n^\mu (\psi_{\text{jet}}, \eta_{\text{jet}}) \quad (5.19)$$

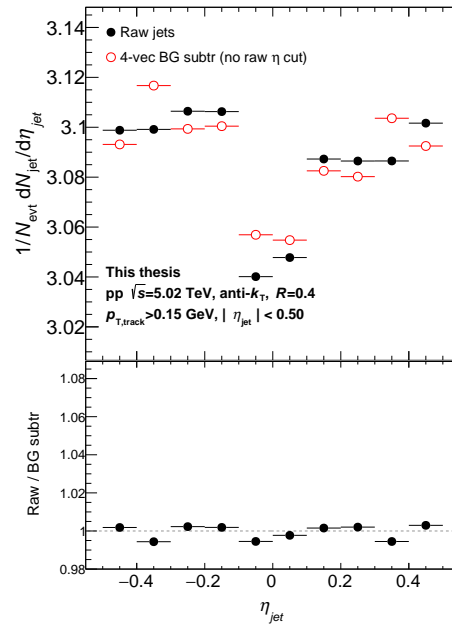
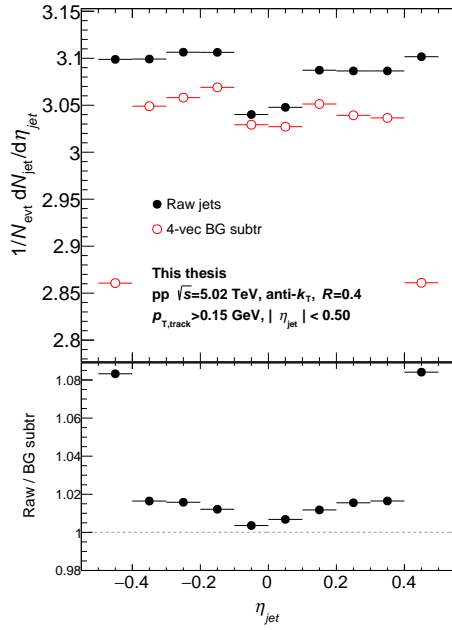
$$\approx A_{\text{jet}} n^\mu (\psi_{\text{jet}}, \eta_{\text{jet}}), \quad (5.20)$$

where the  $n^\mu$  vector now has the jet  $\phi$  and  $\eta$  information. Furthermore, the transverse area of a jet

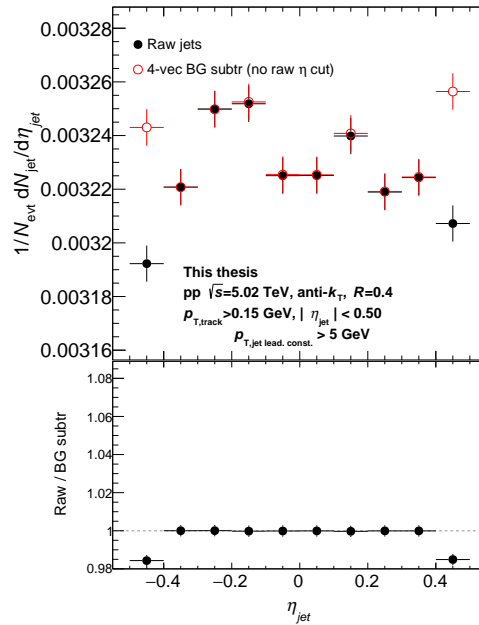
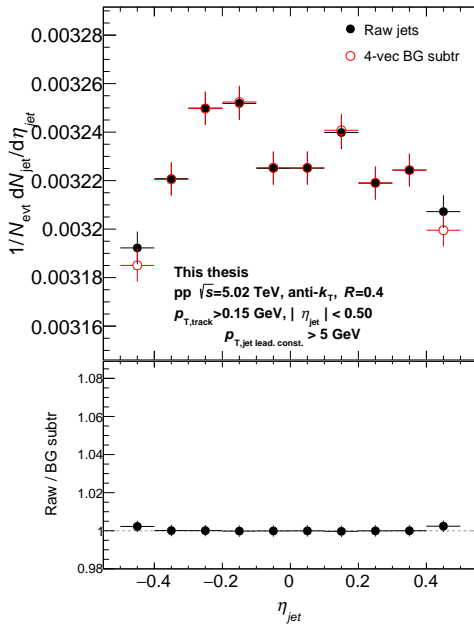
$$A_T = \sqrt{A_x^2 + A_y^2} = A_{\text{jet}} \sqrt{\cos^2 \phi + \sin^2 \phi} = A_{\text{jet}}, \quad (5.21)$$

so the method returns the previously shown underlying subtraction for the simple jet  $p_T$ .

The 4-vector background subtraction can and will shift the directions of a jet according to the background. This does not affect high-energy jets, like the ones I am interested in the dijet analysis, but it does shift softer jets quite a bit. One way to show how this behaves is to see how much jets are shifted outside of the jet pseudorapidity acceptance  $|\eta_{\text{jet}}| < 0.5$ . Figure 5.7a compares raw jets and 4-vector background subtracted jets without any transverse momentum cut. It shows how many jets are lost outside of the acceptance due to the shift caused by the 4-vector background subtraction. If one would accept jets that would be reconstructed originally outside the jet acceptance but then would shift inside due to the background subtraction, this would create a feed-in effect which would balance the situation within 1% as is seen in figure 5.7b. Fortunately, this effect is very small for harder jets. In figures 5.7c and 5.7d, I have selected only jets that include a leading constituent that has a transverse momentum of at least 5 GeV and created the same figures. This shows that the 4-vector background subtraction does not shift hard jets significantly.



(a) Raw jets and 4-vector background subtracted jets. The background subtraction shifts some of the jets outside of the jet acceptance. (b) In this figure, the jet rapidity cut was made after the background subtraction.



(c) Raw jets and 4-vector background subtracted jets inside acceptance. The leading constituent of each jet is required to have  $p_T > 5$  GeV. (d) In this figure, the jet rapidity cut was made after the background subtraction. The leading constituent of each jet is required to have  $p_T > 5$  GeV.

FIGURE 5.7 Tests for how much the 4-vector background subtraction shifts jets outside or inside the acceptance. No  $p_T$  cut was applied for this study.

## 6 ANALYSIS

### 6.1 Dijet invariant mass definition

Dijets generally refer to a two-jet system, usually thought to be roughly back-to-back azimuthally due to the kinematics. In this analysis, I am specifically interested in the leading and subleading jets of the event, meaning the most energetic and second most energetic jets. High transverse momentum jets are a rare occurrence. For example, in 5.02 TeV pp collisions, I found events with leading and subleading jets with over 20 GeV jets roughly once every 300k minimum bias events used in the analysis.

In addition to requiring the jets to have transverse momentum over 20 GeV, I require that the azimuthal angle between the leading and subleading jet is over  $\pi/2$  so that the chance that I measure a dijet with jets from the same hard interaction is better. Suppose the azimuthal angle between the leading and the subleading jet is too close. In that case, the subleading jet is discarded from this dijet search, and the next highest  $p_T$  jet after the discarded one is tested for the transverse momentum and the azimuthal angle conditions. A dijet is formed if these are satisfied.

The dijet, which is formed out of jets labeled  $c$  and  $d$ , has an invariant mass of

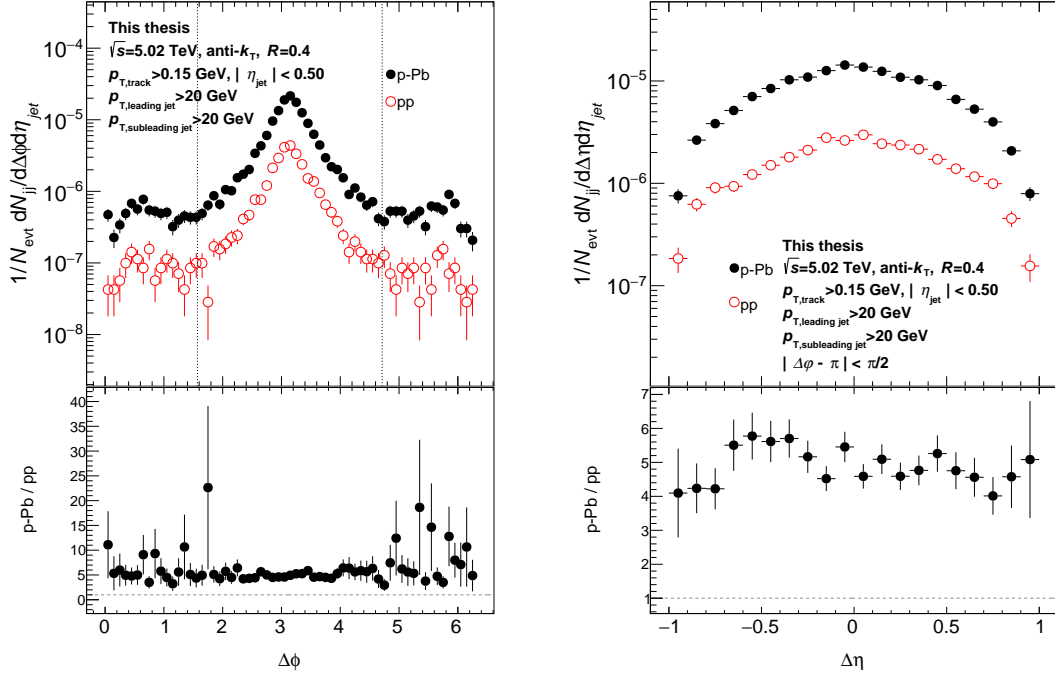
$$M_{jj}^2 = (p_c + p_d)^2 \tag{6.1}$$

$$= m_c^2 + m_d^2 + 2(m_{T,c}m_{T,d} \cosh \Delta y - p_{T,c}p_{T,d} \cos \Delta\phi) \tag{6.2}$$

$$\approx 2p_{T,c}p_{T,d} (\cosh \Delta\eta - \cos \Delta\phi), \tag{6.3}$$

where the approximation holds for a case when  $m/p_T \ll 1$ . In this analysis, all jets are massless as I use the  $p_T$ -scheme to reconstruct the jets. However, the background subtraction will generate a small mass for each jet as the energy of the jet will not match the momentum of the jet exactly anymore.

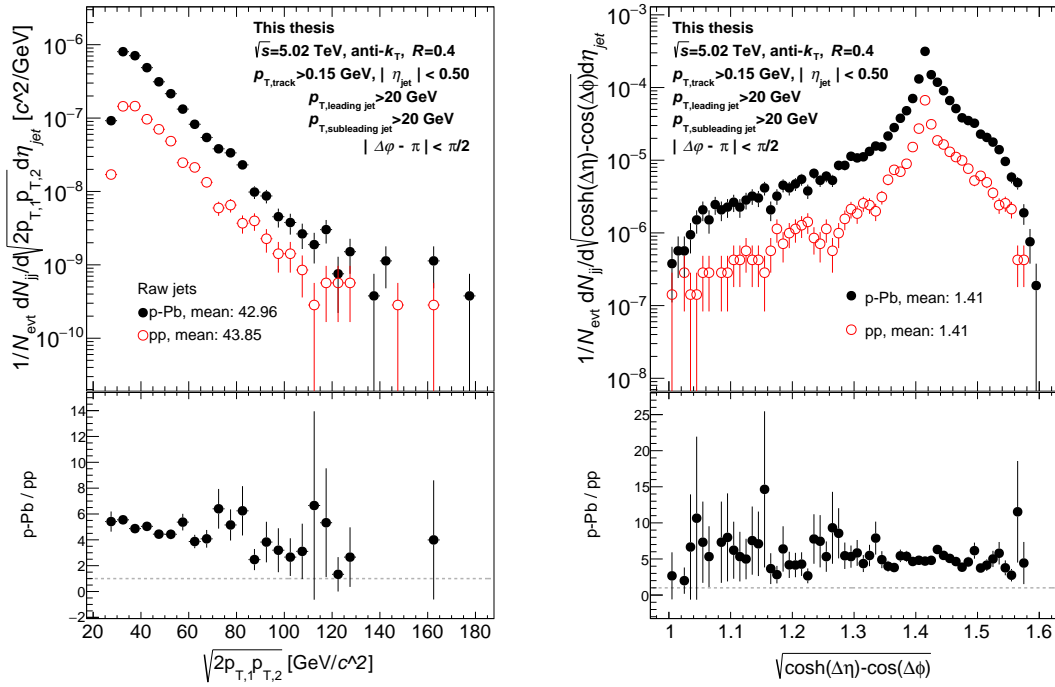
The dijet mass mostly forms from the transverse momentum of the leading and subleading jets, but the geometry of the dijet has a sizeable contribution. Using jets without any background subtraction, I have studied the kinematical part



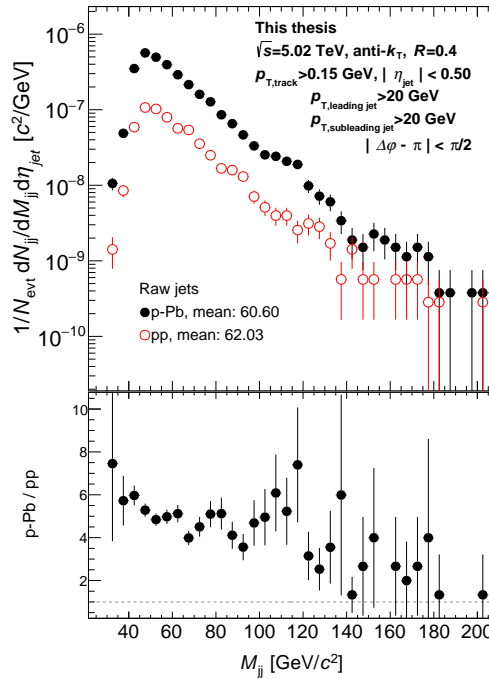
(a) The azimuthal angle difference of the di-jet system. (b) The difference in pseudorapidity of leading and subleading jets.

FIGURE 6.1 The geometrical components of a dijet system.

$\sqrt{2p_{T,c}p_{T,d}}$  and the geometrical part  $\sqrt{\cosh \Delta\eta - \cos \Delta\phi}$  of the dijet system. The geometrical part is formed from the  $\Delta\eta$  and  $\Delta\phi$  distributions, which I have drawn in figure 6.1. The  $\Delta\eta$  figure shows only accepted dijets, but the  $\Delta\phi$  figure also extends to dijets which are cut before the analysis is done to demonstrate how the whole  $\Delta\phi$  spectrum behaves. This is signified by two dotted lines drawn at  $\pi/2$  and  $3\pi/2$ , and only dijets from between these lines are used in the analysis. The shapes of  $\Delta\phi$  and  $\Delta\eta$  are very similar for both pp and p-Pb, as seen in the ratio plots underneath. It has also been studied that the more energetic the dijet is, the more likely the leading and subleading jets are located near the mid-rapidity of the detector [95], creating more  $\Delta\eta \approx 0$  dijets. As the jet acceptance for  $R = 0.4$  jets in ALICE is  $|\eta_{\text{jet}}| < 0.5$ , which restricts the  $|\Delta\eta| < 1$  and thus the hyperbolic cosine  $1 \leq \cosh(\Delta\eta) \leq \cosh(1) \approx 1.54$ . The cosine term, on the other hand, will always be negative because of the  $\Delta\phi$  cut. The kinematical part, geometrical part, and the dijet invariant mass of raw dijets are shown in figure 6.2. The geometrical part of the equation is peaked around  $\sqrt{2} \approx 1.41$ , reinforcing the fact that most of the dijets are close in pseudorapidity due to the relatively small jet acceptance of ALICE and back-to-back in azimuthal angle. The maximum value of the geometrical part is  $\sqrt{1.54 + 1} \approx 1.595$ , after which there are no hits in the histogram. Multiplying the means of the kinematical and geometrical parts the result is very close to the mean of the dijet mass. The  $\Delta\phi$  cut only affects the very low mass dijets, as seen in figure 6.3. This observation is in line with the expectation that hard events and hard jets splittings are a rare occurrence.

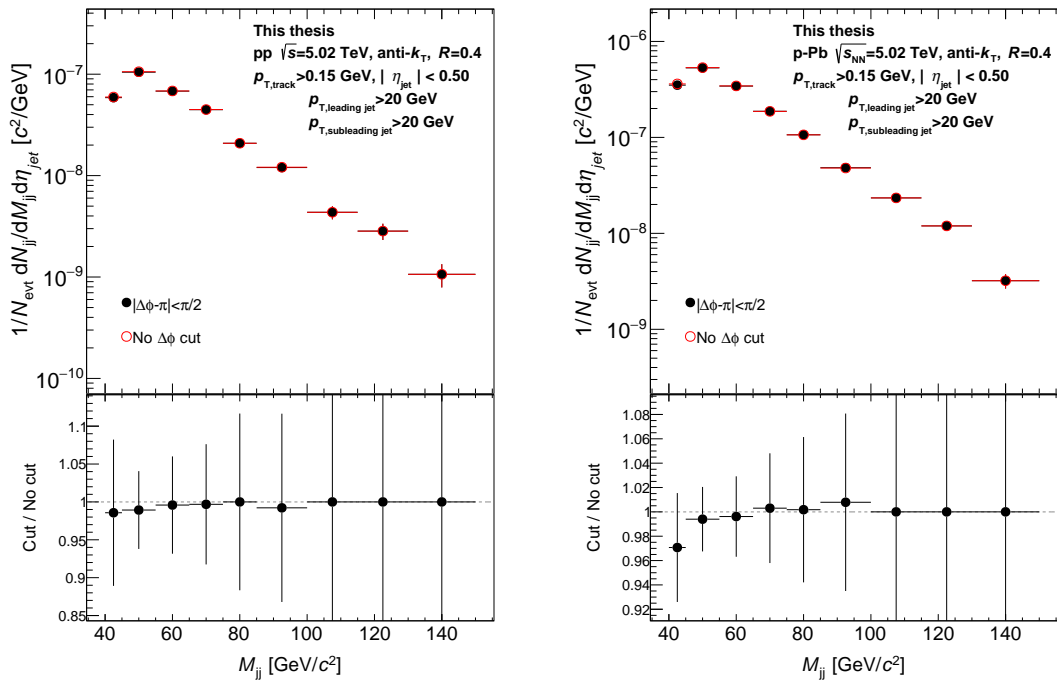


(a) This is the kinematical part of the dijet invariant mass. (b) This is the geometrical part of the dijet invariant mass.



(c) The dijet invariant mass formed from raw jets without background subtraction.

FIGURE 6.2 A comparison of dijet invariant mass and the parts it is formed. The mass mean is approximately the mean of the kinematical and geometrical parts of the mass.



(a) Proton–proton collisions.

(b) Proton–lead collisions.

FIGURE 6.3 The effect of the azimuthal angle cut for dijet invariant mass observable. As the cut data sample is a subset of the other, the error is overestimated in the ratio.

## 6.2 Dijet invariant mass differential cross section

In this thesis, I present the dijet invariant mass scaled to the visible cross section  $\sigma_{V0AND}$

$$\frac{d^2\sigma_{\text{dijet}}}{dM_{\text{jj}}d\eta} \equiv \frac{\sigma_{V0AND}}{N_{V0AND}^{\text{tot evt}}} \frac{dN_{\text{dijet}}}{dM_{\text{jj}}d\eta}, \quad (6.4)$$

where the  $dN_{\text{dijet}}$  is a number of dijets in a specific mass bin with a bin width of  $dM_{\text{jj}}$ , and finally  $d\eta$  is the total width of the jet acceptance, which is 1.0. But as discussed in section 4.3 some visible cross section events are missing as the primary collision vertex was not reconstructed. The number of events which are available to the analysis  $N_{V0AND}^{\text{evt has vtx}}$  can be corrected using the correction factor defined in equation (4.6) resulting in equation

$$\frac{d^2\sigma_{\text{dijet}}}{dM_{\text{jj}}d\eta} = \epsilon_{\text{vtx}} \frac{\sigma_{V0AND}}{N_{V0AND}^{\text{evt has vtx}}} \frac{dN_{\text{dijet}}}{dM_{\text{jj}}d\eta}. \quad (6.5)$$

Lastly, to ensure high-quality measurements, I restrict the accepted events only when the primary collision vertex  $z_{\text{vtx}} < 10$  cm, which is a default cut used in ALICE. This will not affect the differential cross section as the ratio of dijets to events stays the same as the physics is independent of the position of the collision

$$\frac{dN_{\text{dijet}}^{<10 \text{ cm}}}{N_{<10 \text{ cm}}^{\text{evt}}} = \frac{dN_{\text{dijet}}}{N^{\text{evt}}}. \quad (6.6)$$

As shown in equation (4.4) the ratio of cross section divided by the number of events is constant. The events which are not triggered by the minimum bias trigger almost never have a jet in them because of the large number of tracks created by a jet; thus the number of jets or dijets  $dN$  does not change between the inelastic and visible cross section events. One exception to this would be the central diffractive events where a dijet is born diffractively so that both projectiles stay intact. CMS and TOTEM [217] collaborations ran a Monte Carlo study where they estimated a visible cross section of 26.1 pb for dijets with a mass of 100 GeV or over born in centrally diffractive events [218]. The small cross section estimated by the CMS and TOTEM implies a small contribution to the dijet events with no V0-AND trigger. As such, the differential cross section as written in equation (6.5) is a close approximation to the inelastic differential cross section.

## 6.3 Nuclear modification factor

The parton energy loss in a heavy ion system is quantifiable with the nuclear modification factor, defined experimentally as

$$R_{AB} = \frac{\frac{1}{N_{\text{evt}}^{AB}} \frac{dN^{AB}}{dM_{\text{jj}}}}{\langle N_{\text{coll}}^{AB} \rangle \frac{1}{N_{\text{evt}}^{\text{pp}}} \frac{dN^{\text{pp}}}{dM_{\text{jj}}}}, \quad (6.7)$$



where  $N_{\text{evt}}$  are the number of events for pp and AB collisions, and  $\langle N_{\text{coll}}^{\text{AB}} \rangle$  is the average number of inelastic nucleon–nucleon collisions in the AB collisions. This number can be calculated for some specific centrality bin or integrated over all collisions. In minimum bias p–A collisions, with no multiplicity selection, the average number of inelastic collisions can be written as [7, p.62]

$$\langle N_{\text{coll}}^{\text{AB}} \rangle = AB \frac{\sigma_{\text{inel}}^{\text{pp}}}{\sigma_{\text{inel}}^{\text{AB}}}, \quad (6.8)$$

where  $\sigma_{\text{inel}}$  are the inelastic cross section for pp and AB collisions. Now then, using this information, the nuclear modification factor for minimum bias events can be written as

$$R_{\text{AB}} = \frac{\frac{d\sigma_{\text{inel}}^{\text{AB}}}{dM_{\text{jj}}}}{AB \frac{d\sigma_{\text{inel}}^{\text{pp}}}{dM_{\text{jj}}}}. \quad (6.9)$$

## 6.4 Underlying event fluctuations

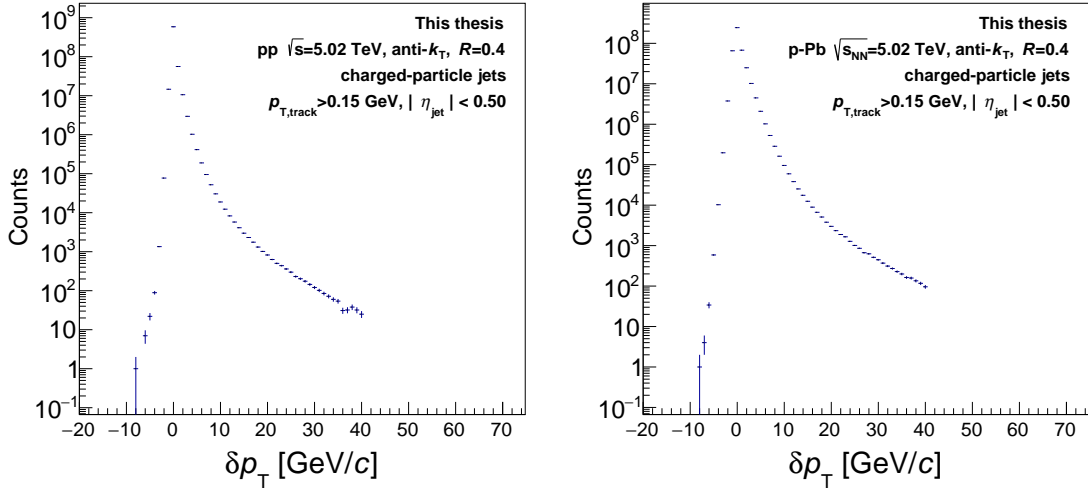
As discussed in section 5.2, single jets and dijets alike need background subtraction, especially in the heavy ion environment where hadrons not originating from the hard event grow more and more prevalent. If the background is subtracted, underlying event fluctuations should also be studied and corrected. The soft background is sizeable in p–Pb collisions, so subtracting it cannot be circumvented, and in order to make a good comparison between pp and p–Pb, the background needs to be subtracted from the pp collisions as well.

The underlying event fluctuations for the single jet  $p_{\text{T}}$  have been studied and measured in previous measurements [201, 219, 220], which I will now replicate here before moving on to the dijet mass. A random cone method is used for the single jet  $p_{\text{T}}$  background fluctuations. A random cone fully within the detector acceptance is selected for each measured event. The cone includes the underlying event, which we are subtracting with the technique established in section 5.2, but also the fluctuations. By comparing the cone  $p_{\text{T}}$  to the estimated background, the fluctuations can be written as

$$\delta p_{\text{T}} \equiv \sum_i p_{\text{T},i} - \rho \times \pi R_{\text{cone}}^2 \quad (6.10)$$

where  $R_{\text{cone}} = 0.4$ . This can be measured straight from the measured data, and in figure 6.4, the background fluctuation distributions are shown for pp and p–Pb, which I have obtained for my analysis. The jet  $p_{\text{T}}$  analysis I have conducted for this thesis is outlined in the appendix A, and hereafter I focus on the dijet observable.

In the following text, I will generalize the  $\delta p_{\text{T}}$  background fluctuations estimation method to the dijet invariant mass analysis. The dijet for each eligible collision will be formed from jets where the underlying soft event has been



(a) pp

(b) p-Pb

FIGURE 6.4 The underlying event fluctuations for jet  $p_T$  observable, measured from the data using a random cone method. The cut at 40 GeV has been done to reflect previous jet analysis, which will be compared to later in this thesis.

subtracted from using the techniques provided in section 5.2, so the background fluctuations will affect the dijet invariant mass observable in a similar way as the single jet  $p_T$ . I defined a cone pair in a way that it is perpendicular to the dijet system in azimuthal angle. Pseudorapidity for each cone is copied from the jets. A schematic representation of these cones is seen in figure 6.5. A local  $p_T$  density is estimated for each cone

$$\rho' \equiv \sum_{\text{cone}} p_{T,i} / (\pi R_{\text{cone}}^2), \quad (6.11)$$

where  $R = 0.4$  is the radius of the cones, which is the same as the resolution parameter for jet reconstruction. This  $\rho'$  is then used to subtract the underlying event for each jet respectively, in the same manner as in equation (5.12), but instead of using the normal  $\rho$  calculated from the median, I use the  $\rho'$ . Note that as I have two separate cones, sometimes the fluctuations have an opposite effect on the two dijet partners.

After the UE is subtracted with the local  $p_T$  density  $\rho'$  for the leading and subleading jets, I obtain the dijet mass  $M_{jj}'$  with recalculated jets and measure the fluctuations with the difference

$$\delta M_{jj} \equiv M_{jj} - M_{jj}'. \quad (6.12)$$

Two vetoes are used when generating the  $\delta M_{jj}$  to reflect the background truthfully. Firstly, all  $\delta M_{jj}$ , which have a negative  $M_{jj}'$ , are not accepted. This is because the local background found in the cone has a higher  $\rho' \times A_{\text{jet}}$  than the jet  $p_T$ , resulting in a background subtraction larger than the jet itself. The cases where the fluctuations are higher than the jet itself are not interesting for this analysis. Another veto is used when either cone is overlapping with either leading

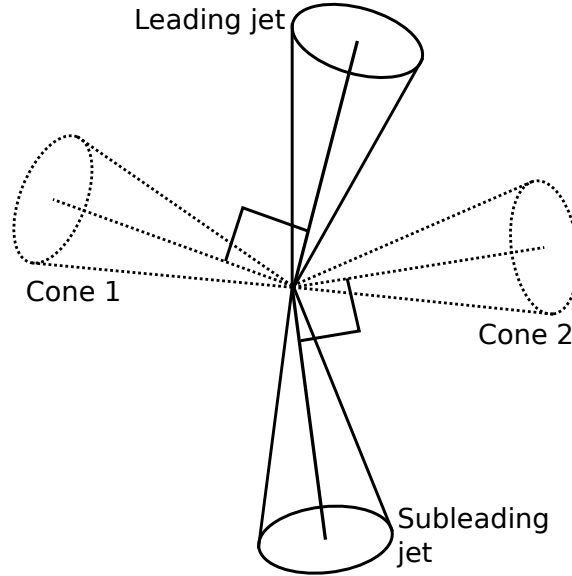


FIGURE 6.5 The rotated cone method for estimating the underlying event fluctuations.

or subleading jets. These overlapping cones and jets provide no useful information as the leading and subleading jets cannot become overlapped due to the  $\Delta\phi$  azimuthal angle cut used during the dijet analysis.

In figure 6.6, I have drawn the  $\delta M_{jj}$  spectrum for pp and p-Pb collisions. Here one can see that the peak is formed around zero but slightly favors the positive side. High values of  $\delta M_{jj}$  are mostly overlaps of the cones and some tertiary jet, thus creating a large fluctuation. To suppress the low statistics and to leave out the few outliers, I fitted the peaks with an asymmetric generalized Gaussian

$$f(x) = C \times \begin{cases} \exp \left[ - \left( \frac{|x-\mu|}{\sigma^+} \right)^{p^+} \right], & x - \mu > 0 \\ \exp \left[ - \left( \frac{|x-\mu|}{\sigma^-} \right)^{p^-} \right], & x - \mu \leq 0 \end{cases}, \quad (6.13)$$

where the positive and negative side of the function have their own power and width. The fitted parameters are written in table 6.1. With the fit, I fill the fluctuation response matrix assuming that the fluctuations are equally strong for each dijet mass value, which I confirmed to be true for dijet masses such as those measured in this analysis. The fit is copied to every row of the 2D histogram by integrating the fit for each bin, and in a way that the  $\delta M_{jj} = 0$  is set as the diagonal bin of the 2D histogram. The 2D UE fluctuation response matrices are seen in figures 6.9a and 6.10a for dijet mass. The usage of this response matrix is detailed in the section 6.6.

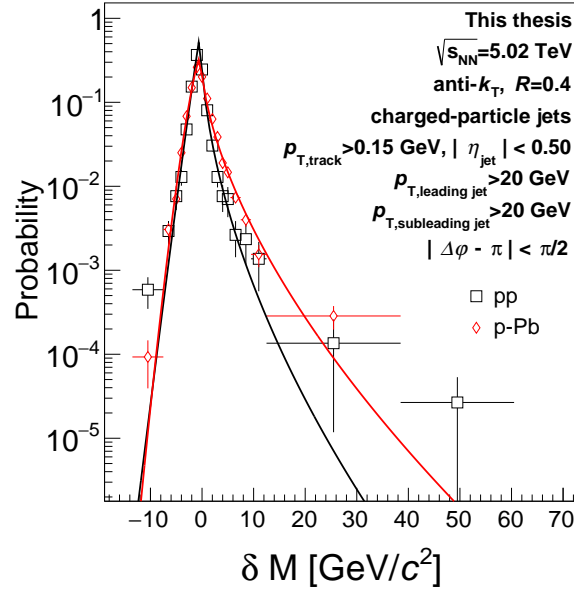


FIGURE 6.6 The underlying event fluctuations for the dijet mass observable for pp and p–Pb. The asymmetric generalized Gaussian fit is used to generate the unfolding matrix for the fluctuations. I have written the details of the fits in table 6.1.

TABLE 6.1 The fitted parameters for the asymmetric generalized Gaussian used to fit the  $\delta M_{jj}$  distribution drawn in figure 6.6

| System | C    | $\mu$ | $\sigma^-$ | $\sigma^+$ | $p^-$ | $p^+$ |
|--------|------|-------|------------|------------|-------|-------|
| pp     | 0.69 | -0.31 | 1.09       | 0.30       | 1.06  | 0.55  |
| p–Pb   | 0.36 | -0.27 | 1.82       | 0.76       | 1.35  | 0.60  |

## 6.5 Detector response

Real detectors have a finite efficiency and resolution, which differ from experiment to experiment. The detector system can have portions that are unavailable for the time of measurement, or there are some limitations for measuring very low or very high-energy particles. For example, the tracking efficiency of the TPC is shown for Pb–Pb and pp collisions in figure 6.7, where one can see how the TPC performs in almost the same way with different collision systems and with approximately 80% efficiency for high transverse momentum particles. This is the biggest sole contribution to the detector response for this analysis. In addition, there are many background effects hindering the physics measurement that should not be accounted for in the results, some of these include beam–gas interactions and cosmic particles. It is very clear that the performance of a specific measurement depends on the experiment itself, but also on the time of the measurement. Different experiments have hugely different experimental setups,

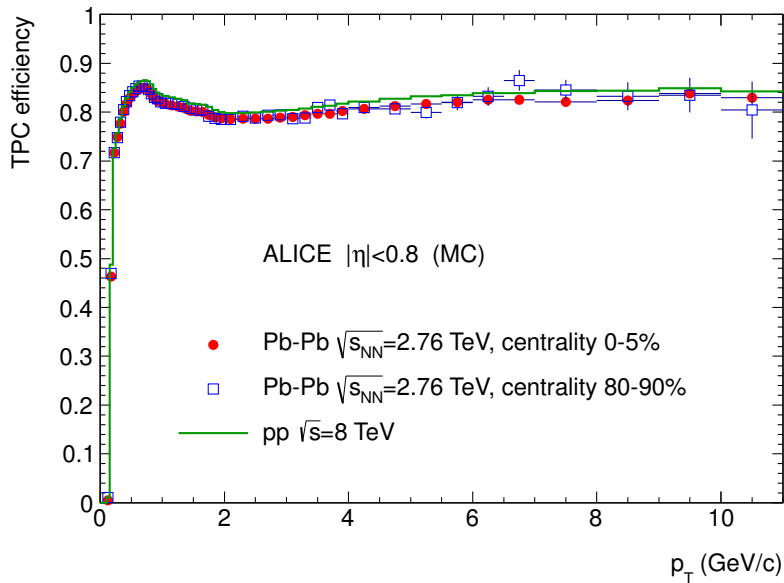


FIGURE 6.7 The tracking efficiency of ALICE TPC in central and peripheral Pb–Pb collisions, and in pp collisions. Figure from [203], reprinted under the license CC BY 3.0.

but also, for the same experiment, the measurements will change in time due to detector degradation and slowly changing environmental situations.

Measurements sensitive to detector effects, like jet  $p_T$  and dijet invariant mass, are not trivially comparable between experiments and sometimes even between measurements of the same experiment at different times. In addition, comparison to theory results is not feasible before correcting the measured data or alternatively simulating the detector effects for the theory results. The latter is, of course, not usually feasible as one would need to do this for every experiment separately, so the former is the most commonly used method.

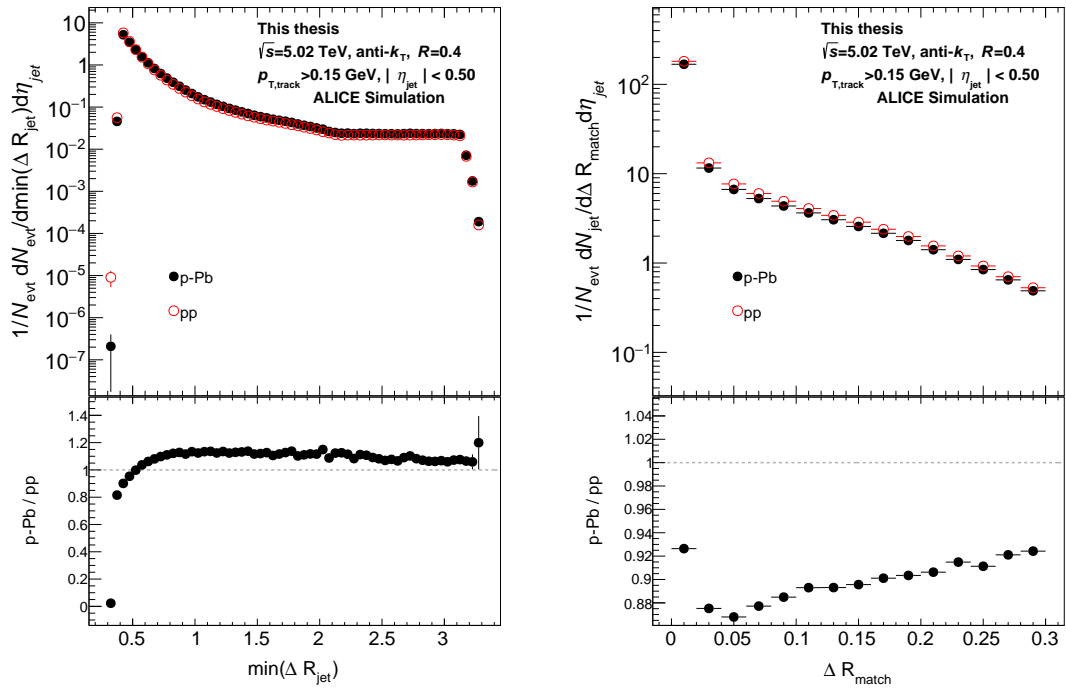
For each physics measurement done in the experiment, the full status of the complete detector is saved for that particular measurement. This information is used to model the behavior of the detector during the time the measurement was made. The modeling of the detector is done with the GEANT3 or 4 [153, 154], and the collisions are simulated with a tuned multipurpose MC, the most common being Pythia 6 or 8 [100]. These MC particles are fed into the full detector simulation, including the triggering and all instrumentation, generating results in an identical way as the data. This detector-simulated MC, usually shortened as detector MC, is the best estimate of the detector’s behavior. By comparing this to the original MC results, called true MC, I can estimate how an observable, in this work, the dijet invariant mass spectrum, is modified during the detector simulation.

To compare detector MC jets to true MC jets, they need to be matched. In this analysis, I match the jets geometrically in the  $\eta$ – $\phi$  plane by requiring that  $\Delta R = \sqrt{\Delta\eta^2 + \Delta\phi^2} < 0.3$  between the true and detector level jets. The geometrical matching parameter should typically be smaller than the jet resolution parameter  $R$ , which is 0.4 for this analysis, but each analysis should consider the

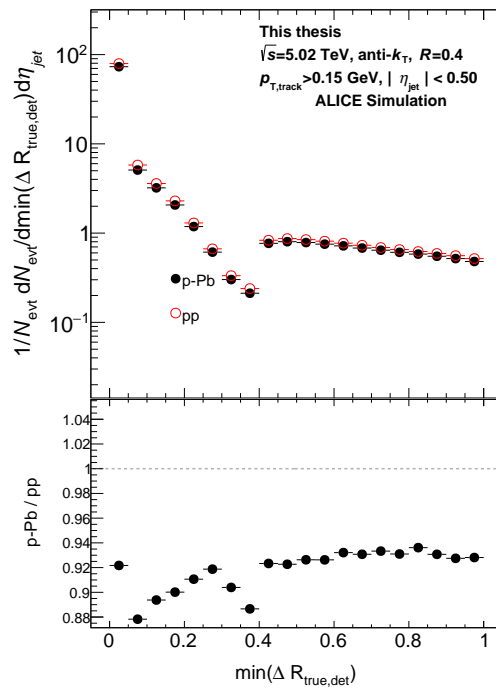
best value for their specific case.

The matching can be studied by measuring different  $\Delta R$  values between jets. Figure 6.8a shows the minimum distance between any two jets in each event that I have analyzed. Most of the time, this distance is about 0.5–0.6, and specifically, there are no entries below  $R = 0.4$ , which is the jet resolution parameter of my analysis. This is why the matching parameter should be lower than the resolution parameter. I have also inspected the distances of matched jets in figure 6.8b to see that the matching distance is focused on the first bin, which matches with a distance under 0.01 and, after that, a decreasing trend. To estimate if I could be missing something, I inspected the minimum distance between the detector and true jets for each event in figure 6.8c. This will most of the time show a matched jet as those will have the smallest distance in a similar way as in the figure 6.8b, but when the match is missing, I can see  $\Delta R$  values larger than 0.3. Right after the distance of 0.4, I can see a bump of jets peaking around 0.5–0.6, which corresponds well to the  $\Delta R$  peak I see at figure 6.8a where the minimum distance of jets in the same event has been measured. This means that the peak around 0.5–0.6 in the minimum distance between the detector and true jets figure 6.8c is formed from separate jets and should not be matched.

For a dijet system to match, I need a dijet in both true and detector level MC. If a dijet is found from both levels, I have required both the leading and subleading jet to match. The order of leading and subleading jets can be changed after detector simulation as it is still the same object. The double matching naturally makes dijets less likely to match than single jets. The detector response for the dijet invariant mass can be seen in figures 6.9b and 6.10b. The hits are focused on the diagonal with some spread around it. From the shape of the response, one can see that a detector dijet with a certain mass is most likely originating from a true dijet with a higher mass.



(a) The minimum distance between all jets in a single event. Note how there are no jets under 0.3. (b) The distances of matched jets. Note that the first bin, including the value zero, is noticeably higher than the rest.



(c) The minimum distance between the detector and true jets in an event.

FIGURE 6.8 A set of figures to show the reasoning behind the chosen matching radius of 0.3.

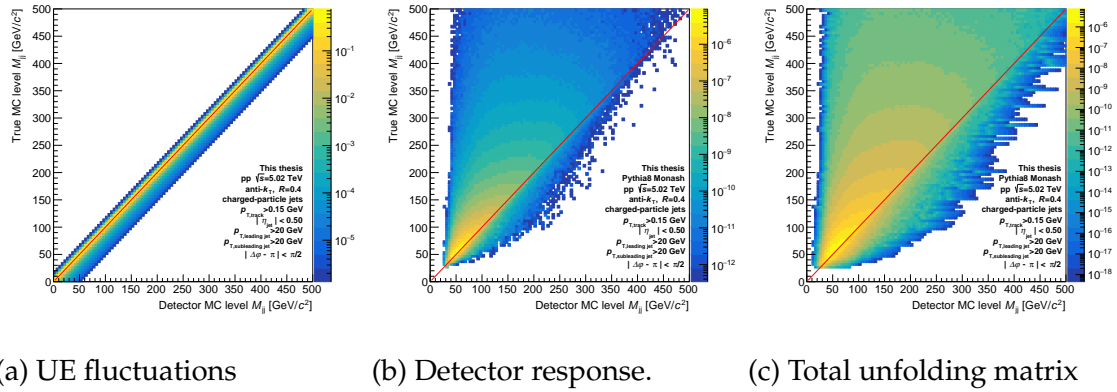


FIGURE 6.9 The unfolding matrices for the dijet invariant mass in proton–proton collisions.

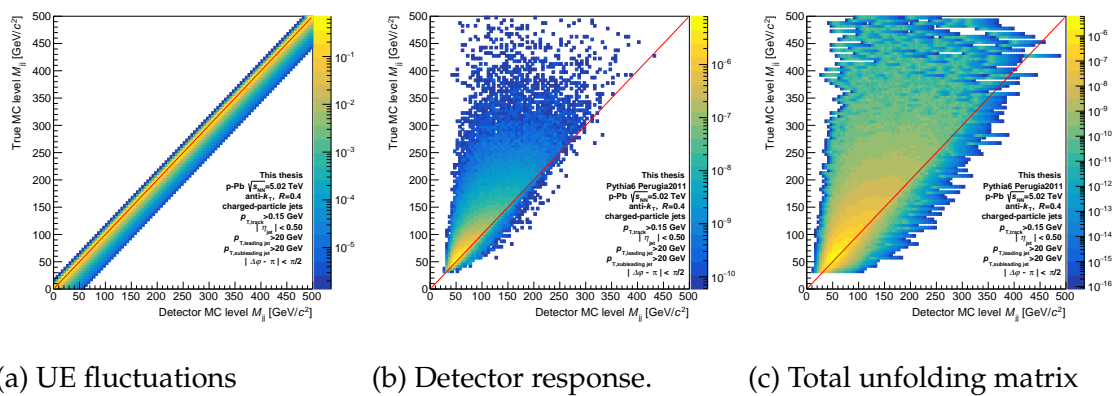


FIGURE 6.10 The unfolding matrices for the dijet invariant mass in proton–lead collisions.



## 6.6 Unfolding procedure

In the previous sections, I have presented the modifications of the observables due to background fluctuations and detector effects. When scaled appropriately, the matched detector level spectrum can be represented by the equation

$$d_{\text{det}}^{\text{matched}} = M_{\text{response}} d_{\text{true}}^{\text{matched}}, \quad (6.14)$$

where the  $d$  vectors represent the spectrums for true and detector levels, and the  $M$  is the 2D response matrix. Then the response matrix can be split up into two parts, the detector, and background fluctuations

$$d_{\text{det}}^{\text{matched}} = M_{\text{response}}^{\text{bg fluc}} M_{\text{response}}^{\text{det}} d_{\text{true}}^{\text{matched}} \quad (6.15)$$

where I want to apply the detector response first, as the background fluctuations have been calculated from the real data before any detector corrections. This way, the true spectrum will be transformed first into detector level and then smeared for the background fluctuations. After both are applied, the resulting spectrum is the matched detector spectrum.

The response corrects only the matched dijets, so I need to apply corrections to the account for true dijets that did not find a pair in the detector level. These dijets are called misses in the unfolding process. In addition, there is also a possibility that a dijet can appear in the detector level MC not seen on the true side at all, and these dijets are called fakes. It is possible that a dijet is found in true and detector levels, but there is no match between them. This results in both a fake and a miss.

I calculate the fakes and misses by comparing the detector response projections to the true and detector level spectrum. The spectrum for true level MC contains all true dijets, but the response projection to the true axis lacks the dijets that were not matched, i.e. misses. I can obtain the fraction of missed dijets by calculating the ratio of the response projection to the true MC axis to the true MC spectrum itself. This can be applied to the detector MC as well, now comparing the detector MC spectrum to the response matrix projected to the detector MC axis, which is not including the fake dijets in the detector level. The comparisons for these and the resulting fractions of fakes and misses are shown in figures 6.11 and 6.12.

In the appendix A, the same figures are shown for single jet  $p_T$ . Single jets generally have fewer fakes and misses. This is natural as the dijet system needs to match two jets instead of only one and requires the jets to be over 20 GeV instead of any jet. This will affect, especially the missing portion, but also fakes, and will limit the lower limit of the measured data that is reliable. The higher the correction of misses and fakes, the higher uncertainty for the detector simulation will affect the results.

Now that I have the fake and miss corrections available to be used, I can apply them as well

$$d_{\text{det}} = D^{\text{misses}} D^{\text{fakes}} M_{\text{response}}^{\text{bg fluc}} M_{\text{response}}^{\text{det}} d_{\text{true}}, \quad (6.16)$$

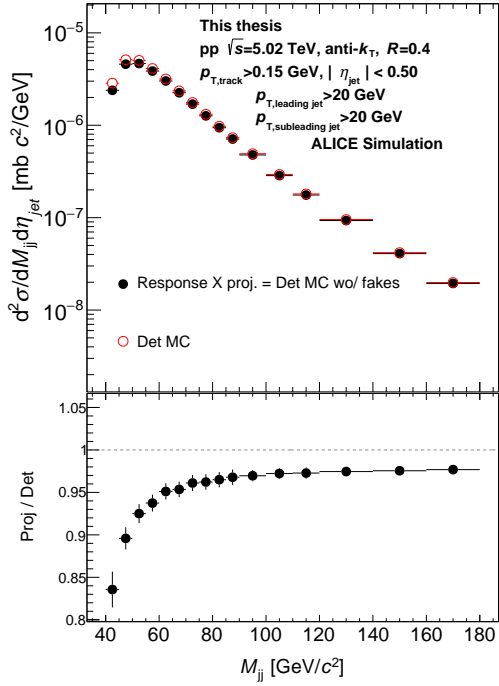
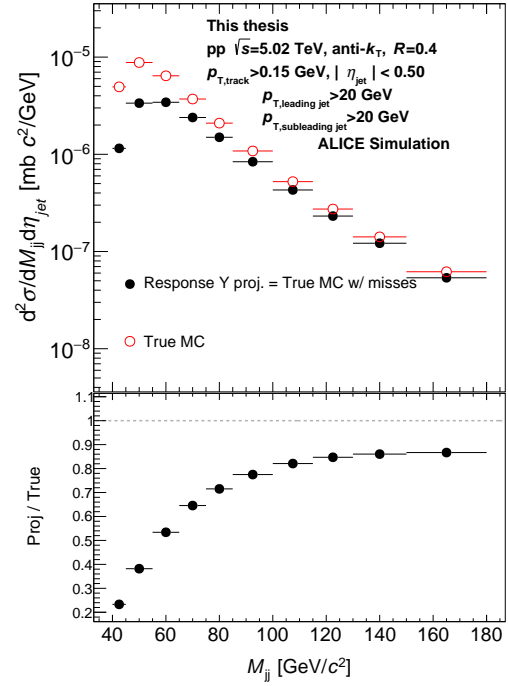
(a) Dijet  $M_{jj}$  fakes for the pp.(b) Dijet  $M_{jj}$  misses for the pp.

FIGURE 6.11 Fakes and misses for the dijet invariant mass spectrum in pp collisions.

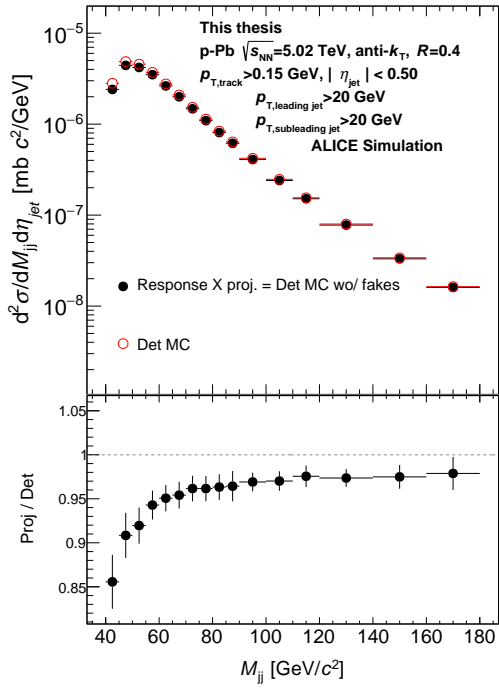
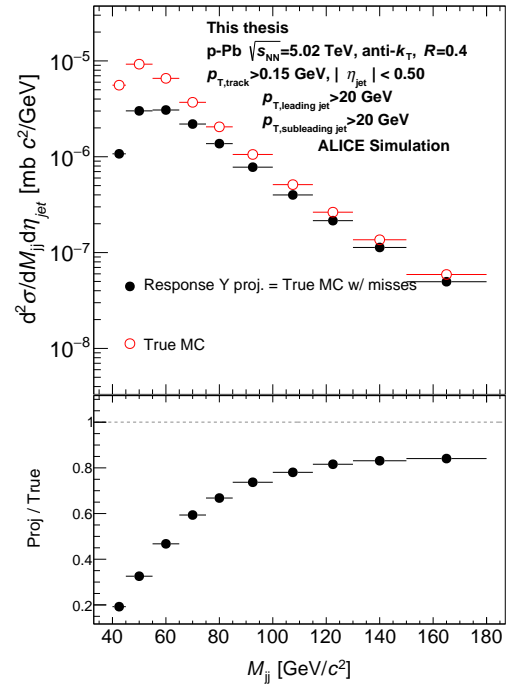
(a) Dijet  $M_{jj}$  fakes for the p-Pb.(b) Dijet  $M_{jj}$  misses for the p-Pb.

FIGURE 6.12 Fakes and misses for the dijet invariant mass spectrum in p-Pb collisions.

where the  $D$  matrices are diagonal and apply a correction for each bin of the spectrum according to the lower part of figures 6.11 and 6.12. The combined total unfolding matrix  $M_{\text{response}}^{\text{bg fluc}} M_{\text{response}}^{\text{det}}$  can be seen in figures 6.9c and 6.10c for the dijet mass.

To correct for the detector effects, I would like to invert the equation (6.16), which is trivial for the diagonal matrices  $D$ , but very nontrivial for the matrices  $M$ . The nontriviality arises from the fact that I have limited statistics to create these matrices, and it is certain that some bins will have only a couple of hits. This will make the outermost off-diagonal elements have large uncertainties and big fluctuations from run to run. As these are scaled to probability, the outlier hits will be extremely small. Inverting a histogram with very small but non-zero values can result in disproportionately large entries in the inverted matrix. This may lead to very large fluctuations in the unfolded results, usually making them unusable.

Unfolding is a technique developed to invert a matrix with limited statistics so that extreme fluctuations will be suppressed. There are several ways to implement this, among which in high-energy physics, the Bayesian iterative method [221] and the Singular Value Decomposition (SVD) [222] method are the most commonly used. In practice, I have utilized the implementations in the widely used RooUnfold C++ package [223] for unfolding purposes. The authors of the package have implemented the Bayesian method, and the SVD unfolding is done with the TSVDUnfold class by K. Tackmann [224].

Based on practical experience, unfolding performs better when unfolding from binning with a larger number of bins to binning with fewer, and for the SVD unfolding algorithm this is an assumed property of the binning [222]. I have used the following binning during the unfolding process:

detector MC : [40, 45, 50, 55, 60, 65, 70, 75, 80, 85, 90, 100, 110, 120, 140, 160, 180],  
true MC : [40, 45, 55, 65, 75, 85, 100, 115, 130, 150, 180, 220, 270, 330, 400].

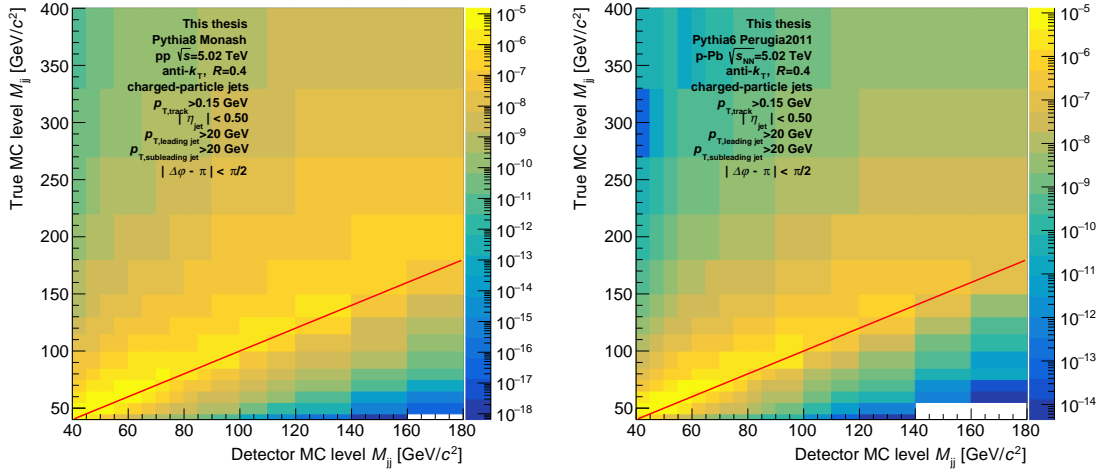
The resulting rebinned unfolding matrix, which includes the background fluctuations and detector response, is presented in figure 6.13. These bins are applied to the data as well. The raw data is first binned to the same bins as in the detector level MC, and the resulting histogram after the unfolding is formed in the binning of the true MC.

It was found during the analysis that, to avoid systematic unfolding problems in the high mass region, it is advisable to continue the true level bins much higher than there is data available. This procedure reduces the propagation of edge effects seen near the end of the binning.

### 6.6.1 Bayesian iterative unfolding method

Bayesian iterative unfolding method [221] uses the widely known Bayes theorem, which can be written in the simplest form as

$$P(C|E) = \frac{P(E|C)P(C)}{P(E)}, \quad (6.17)$$



(a) Proton–proton

(b) Proton–lead

FIGURE 6.13 The rebinned combined response matrix for the dijet mass.

where  $P(C)$  refers to the initial probability of a *cause* and the conditional probability of the said cause to produce the effect  $P(E|C)$ . With this knowledge, it is possible to calculate the conditional probability of a cause, given a certain effect  $P(C|E)$ . Which can be rewritten in the language of high-energy physics to mean “what is the original result given a certain outcome”. The outcome is, of course, the measured jet or the dijet spectrum, and the original result is the measurement without any detector effect, i.e., true MC level result.

In reality, we have many causes for certain effects, that is to say, a true jet or dijet could result in multiple different detector level jets. To reflect this, the Bayes formula can be written

$$P(C_i|E_j) = \frac{P(E_j|C_i) P_0(C_i)}{P_0(E_j)} \quad (6.18)$$

$$= \frac{P(E_j|C_i) P_0(C_i)}{\sum_k P(E_j|C_k) P_0(C_k)} \quad (6.19)$$

where in the final step, the basic property of conditional probabilities is used. Now just by having an initial guess, called the prior, for the true distribution  $P_0(C_i)$ , and the knowledge of how that true distribution will be distributed in the detector level  $P(E_j|C_i)$ , we can calculate the inverted response.

Given  $n(E_j)$  number of events for a certain measurement of a jet or a dijet, we can use equation (6.19) to calculate the number of true level jets or dijets

$$n_1(C_i) = \sum_j n(E_j) P(C_i|E_j), \quad (6.20)$$

and this corresponds to the unfolded spectrum without corrections from fakes or misses.

As the first step, the Bayesian unfolding method requires the prior distribution  $P_0(C_i)$ . After the first iteration, the resulting probability distribution

$P_1(C_i) = n_1(C_i) / \sum_k n_1(C_k)$  is fed again to the equation (6.19) and we get iteratively closer to the case where we would invert the matrix. As the inverted matrix is not a good solution, iterations must be stopped at some point, usually when the resulting distribution stays relatively unchanged. Even a flat distribution would work as a reasonable guess, but choosing a distribution close to the final result will require fewer iterations to converge. For this analysis, the true MC distribution is set as the prior, and the pp spectrum uses five iterations and p-Pb three.

### 6.6.2 SVD unfolding method

The general idea behind SVD unfolding is that the solution of the inverse of the original response matrix should be somewhat smooth. The statistically significant components need to be retained, while the wildly oscillating components are suppressed. The explanation in this section will follow along with the reference [222].

In the SVD unfolding method, one starts by considering deviations from the true distribution from the initial MC prior vector

$$w_i = \frac{d_i^{\text{true}}}{d_i^{\text{prior}}}, \text{ for each } i, \quad (6.21)$$

which can be multiplied back to the true distribution in the end. The problem of the unfolding is restated as a weighted least squares problem. Realizing that the equation (6.14) will never be truly equal because of the limited number of MC simulation events, we can write the problem in a form

$$(Mw - d_{\text{det}})^T B (Mw - d_{\text{det}}) = \min, \quad (6.22)$$

where the  $B$  matrix is the covariance matrix of the measured vector  $d_{\text{det}}$ . This equation can be simplified with a change of basis to

$$(\tilde{M}w - \tilde{d}_{\text{det}})^T (\tilde{M}w - \tilde{d}_{\text{det}}) = \min, \quad (6.23)$$

where the tilde represents the changed basis for the elements, and the problem stays equivalent. This will not yet solve the problem of wild fluctuations, but now we can assert an a priori assumption of smoothness by introducing penalty factors to the minimizing function

$$(\tilde{M}w - \tilde{d}_{\text{det}})^T (\tilde{M}w - \tilde{d}_{\text{det}}) + \tau (Cw)^T (Cw) = \min, \quad (6.24)$$

where the matrix  $C$  is chosen to be

$$C = \begin{pmatrix} -1 & 1 & 0 & 0 & \cdots & 0 \\ 1 & -2 & 1 & 0 & \cdots & 0 \\ 0 & 1 & -2 & 1 & \cdots & 0 \\ \vdots & \vdots & \vdots & \ddots & 1 & 0 \\ 0 & 0 & 0 & 1 & -2 & 1 \\ 0 & 0 & 0 & 0 & 1 & -1 \end{pmatrix}. \quad (6.25)$$

This will create a new term in the equation (6.24)

$$\sum_i [(w_{i+1}^{\text{true}} - w_i^{\text{true}}) - (w_i^{\text{true}} - w_{i-1}^{\text{true}})]^2, \quad (6.26)$$

which can be interpreted as a numerical second derivative. The smoothness of the outcome is regulated by suppressing this second derivative term. The matrix  $C$  is not invertible by itself as it is degenerate. To make matrix  $C$  invertible, a small diagonal component is added  $C \rightarrow C + \xi I$ , where  $I$  is the unit matrix, and  $\xi$  some small value, usually  $10^{-3}$  or  $10^{-4}$ . Finally, the solution of the minimizing problem presented in equation (6.24) can be presented in a matrix form

$$\begin{pmatrix} \tilde{M} \\ \sqrt{\tau} \cdot C \end{pmatrix} w = \begin{pmatrix} \tilde{d}_{\text{det}} \\ 0 \end{pmatrix} \quad (6.27)$$

$$\begin{pmatrix} \tilde{M}C^{-1} \\ \sqrt{\tau}I \end{pmatrix} Cw = \begin{pmatrix} \tilde{d}_{\text{det}} \\ 0 \end{pmatrix}. \quad (6.28)$$

Now the problem can be solved using the standard singular value decomposition matrix technique (SVD) [225, p.487] method.

Generally speaking, any real value matrix of  $m \times n$  size can be factorized in the form

$$A = USV^T, \quad (6.29)$$

where  $U$  and  $V$  are orthogonal matrices of sizes  $m \times m$  and  $n \times n$  respectively, and the matrix  $S$  is an diagonal  $m \times n$  matrix with non-negative entries  $s_i$ . Orthogonal matrices have an inverse equal to the transpose of the matrix. The numbers  $s_i$  are called the singular values of the matrix  $A$ . Singular values can always be arranged in a non-increasing order by swapping corresponding columns in matrices  $U$  and  $V$ . With this information, we can decompose the previously introduced  $\tilde{M}C^{-1} = USV^T$ . Multiplying equation (6.28) from the left side with

$$\begin{pmatrix} U^T & 0 \\ 0 & V^T \end{pmatrix}, \quad (6.30)$$

and we obtain

$$\begin{pmatrix} S \\ \sqrt{\tau} \cdot I \end{pmatrix} V^T Cw = \begin{pmatrix} U^T \tilde{d}_{\text{det}} \\ 0 \end{pmatrix}. \quad (6.31)$$

By defining  $z \equiv V^T Cw$  and  $y \equiv U^T \tilde{d}_{\text{det}}$  the equation simplifies to

$$\begin{pmatrix} S \\ \sqrt{\tau} \cdot I \end{pmatrix} z = \begin{pmatrix} y \\ 0 \end{pmatrix}. \quad (6.32)$$

The case when  $\tau = 0$  is easily solvable element by element by a simple division given that the singular value matrix  $S$  is size  $m \times m$  with  $n$  non-zero singular values

$$z_i = \begin{cases} \frac{y_i}{s_i} & \text{when } i = 1, \dots, n \\ 0 & \text{when } i = n + 1, \dots, m \end{cases}. \quad (6.33)$$

The case  $\tau > 0$  is more involved and requires matrix multiplication tricks that are motivated in detail in reference [226, chapter 25, section 4]. It turns out that the equation (6.31) can be conveniently manipulated by multiplying with a series of matrices in a clever way. For this, I define a matrix

$$\begin{array}{l} \text{Row } i \\ \text{Row } m+i \end{array} \begin{array}{c} \text{Col. } i \qquad \text{Col. } m+i \\ \left( \begin{array}{cccccc} 1 & 0 & \vdots & & \vdots & 0 \\ 0 & \ddots & & & & \\ \cdots & & \frac{s_i}{(s_i^2+\tau)^{1/2}} & \cdots & \frac{\sqrt{\tau}}{(s_i^2+\tau)^{1/2}} & \cdots \\ & & \vdots & & \vdots & \\ \cdots & & -\frac{\sqrt{\tau}}{(s_i^2+\tau)^{1/2}} & \cdots & \frac{s_i}{(s_i^2+\tau)^{1/2}} & \cdots \\ & & & & & \ddots & 0 \\ 0 & & \vdots & & \vdots & 0 & 1 \end{array} \right), \end{array} \quad (6.34)$$

which is an identity matrix except for the four elements shown in the matrix. For each  $i \in [1, n]$ , the matrices are used to multiply the equation (6.31) from the left. The series of multiplications result in a new set of equations

$$\begin{pmatrix} S^{(\tau)} \\ 0_{n \times n} \end{pmatrix} z = \begin{pmatrix} y^{(\tau)} \\ h^{(\tau)} \end{pmatrix}, \quad (6.35)$$

where the new  $\tau$  dependent components are

$$S^{(\tau)} = \text{Diag} \{s_1^{(\tau)}, \dots, s_n^{(\tau)}\} \quad (6.36)$$

$$y_i^{(\tau)} = \begin{cases} y_i \frac{s_i}{(s_i^2+\tau)^{1/2}}, & \text{when } i = 1, \dots, n \\ y_i, & \text{when } i = n+1, \dots, m \end{cases} \quad (6.37)$$

$$h_i^{(\tau)} = -y_i \frac{\sqrt{\tau}}{(s_i^2+\tau)^{1/2}} \quad (6.38)$$

$$s_i^{(\tau)} = (s_i^2 + \tau)^{1/2}. \quad (6.39)$$

Combining this information with the simple equation (6.35), and the information when  $\tau = 0$  in equation (6.33), we can solve for the true level vector element by element

$$z_i^{(\tau)} = \begin{cases} \frac{y_i^{(\tau)}}{s_i^{(\tau)}} = y_i \frac{s_i}{s_i^2+\tau} & \text{when } i = 1, \dots, n \\ 0 & \text{when } i = n+1, \dots, m \end{cases}, \quad (6.40)$$

and from here, it is easy to see that  $z_i^{(\tau)}$ , which represents the true level distribution, is now regulated by the  $\tau$  in a way that the results remain finite even if a singular value  $s_i$  would become infinitesimally small.

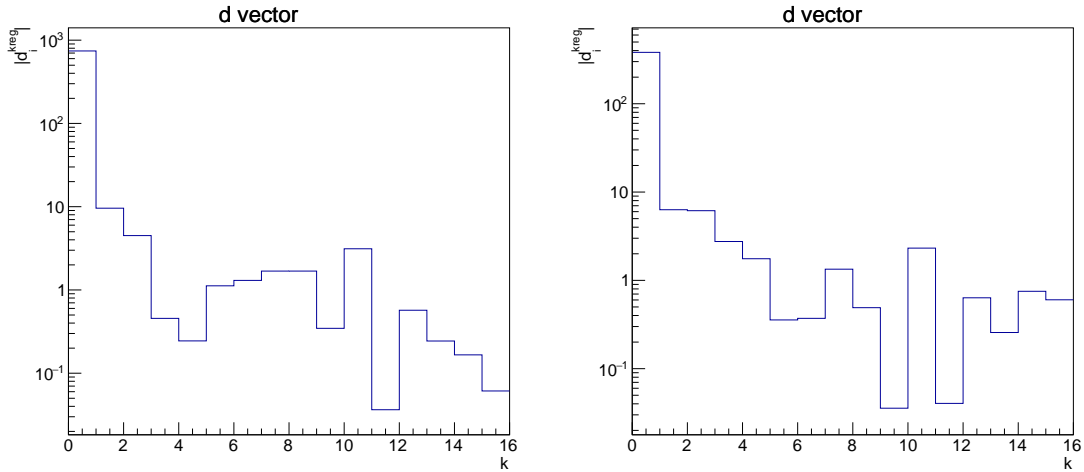
(a)  $d_i$  vector for the pp collisions.(b)  $d_i$  vector for the p–Pb collisions.

FIGURE 6.14 The  $d$ -vector which is used to determine the proper regularization value for the SVD unfolding technique.

The final task is to revert all the manipulations for the  $z$

$$w^{(\tau)} = C^{-1}V_Z^{(\tau)}, \quad (6.41)$$

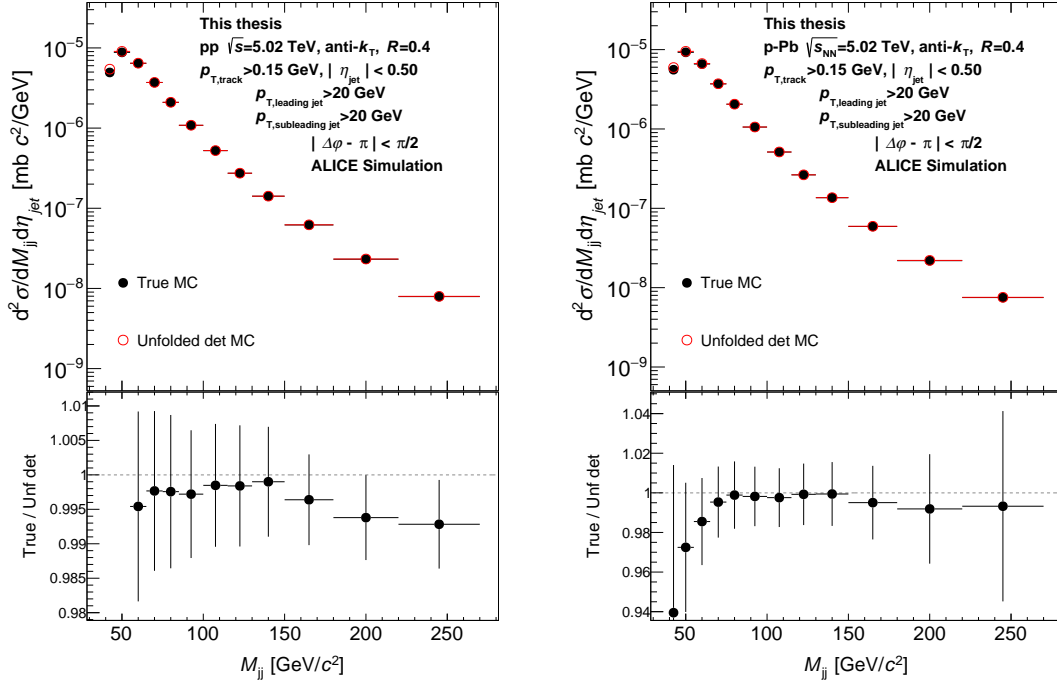
and the original distribution can be achieved by undoing the scaling with prior distribution element by element

$$d_i^{\text{true}(\tau)} = w_i^{(\tau)} d_i^{\text{prior}}. \quad (6.42)$$

Now the main points of the general procedure are explained, but we need to justify the choice of the regularization parameter  $\tau$ . This is decided by the measured vector  $d_{\text{det}}$ , more specifically, the point when the statistical error of the vector components is comparable to the value itself. This is bound to happen at some value because of a limited number of events. This is effectively done by comparing the  $\log(y_i)$  versus  $i$  values (ref [222] uses  $d_i$  vector as a label, thus the name  $d$ -vector). As the SVD uses weighted least squares, and the weight is the statistical error of  $d_{\text{det}}$  in the vector, we are looking at a point when the  $\log(y_i)$  reaches about 1 and stays approximately 1 until the end of the vector.

Figure 6.14 shows the  $d$ -vectors for dijet mass in pp (a) and p–Pb (b) collisions. Based on these figures, I selected the  $k$  value as 9 in pp and 5 in p–Pb collisions. These are the last significant bins, so the regularization parameter  $\tau$  should be put equal to the square of the singular value of the matrix  $\tilde{M}C^{-1}$   $\tau = s_k^2$ . When compared, for example, to the equation (6.40) now the  $\tau = s_k^2$  creates a kind of low pass filter for  $i < k$  as the  $s_i$  are in non-increasing order.





(a) Proton–proton

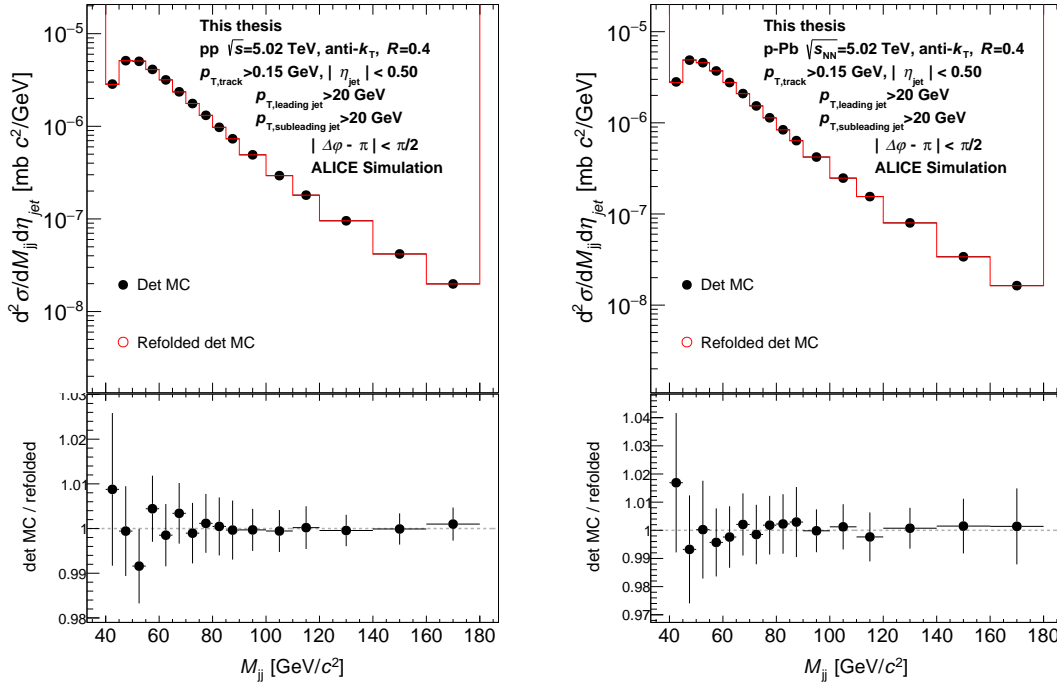
(b) Proton–lead

FIGURE 6.15 The trivial closure test for dijet invariant mass. The test was conducted with the same dataset as the unfolding matrix was generated, thus trivial. In this figure, the datasets are not uncorrelated, so the uncertainty in the ratio is slightly overestimated.

## 6.7 Unfolding validation

Several tests can be done to be convinced of the correctness of the unfolding procedure. The most straightforward test is called closure check, where one unfolds the detector MC and compares that to the true MC spectrum. This should be fairly a good agreement in the mass range of the data. I present the results for the closure test in my analysis in figure 6.15. The proton–proton struggles somewhat after 175 GeV, but that should not be a problem in this analysis as the data is presented at the range from 75 GeV to 150 GeV. In addition, the difference of 0.5 % seen in pp after a dijet mass of 175 GeV would result in a negligible difference in the result when compared to the systematic and statistical errors shown in section 7.1.

Another test that I have done is called a refolding check. While unfolding is a complicated procedure, folding is a straightforward matrix multiplication, where one does not have the problem of fluctuations from the matrix inversion. As the unfolding process should be approximately the inverse of the folding process, one can tailor a refolding test where unfolded detector level MC spectrum is refolded back to the detector level and compared to the original detector MC distribution. In figure 6.16, the result of the refolding test is shown by unfolding and



(a) Proton–proton

(b) Proton–lead

FIGURE 6.16 The refolding check for dijet invariant mass. This check will fold the unfolded detector MC spectrum, and compare it with the original detector MC spectrum.

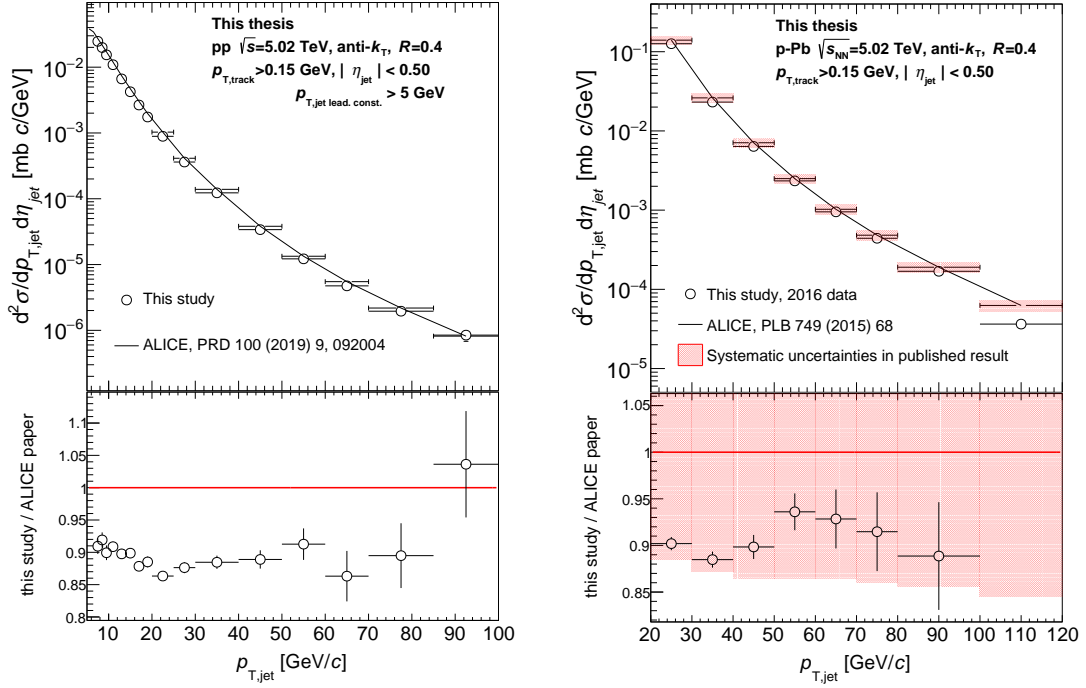
folding a detector MC set, and then it is compared to itself before the manipulations. Besides the numerical artifacts outside the range of the data, the refolding works well within uncertainties.

The detector MC, which is used for unfolding, has to describe the physics reasonably well. In appendix B, I present comparisons between the uncorrected data and detector MC. Overall the agreement in shape is good.

## 6.8 Jet $p_T$ spectrum validation

The jet  $p_T$  analysis follows the same principles as explained in the previous sections for dijet invariant mass. The jet  $p_T$  analysis was replicated as close as possible to the original analysis. More details on the jet  $p_T$  analysis can be found in the appendix A.

For the pp results, it is more straightforward to compare results with no background subtraction done. Instead, to find hard jets, only jets with a leading constituent with  $p_T > 5$  GeV were chosen. This is also reflected in the detector simulation for unfolding purposes. This will greatly lessen the impact of jets born solely from softer interactions. In the left side of figure 6.17, a comparison between this analysis and the published  $\sqrt{s} = 5.02$  TeV pp jet  $p_T$  results [227] is



(a) Proton–proton collisions with no back-ground subtraction unfolded with the Bayesian iterative method with three iterations. (b) Proton–lead collisions, unfolded with the Bayesian iterative method with eight iterations.

FIGURE 6.17 Jet  $p_T$  spectrum comparison.

seen. The discrepancy of 10% has been thoroughly studied inside the collaboration, and it has been noticed that three independent ongoing analyses agree with each other, this analysis among them. Thus an investigation has been started to ascertain the validity of the publication [227]. It was concluded in an internal ALICE meeting that the dijet invariant mass analysis is valid until new findings about the discrepancy are found.

There was no constituent cut for the p–Pb spectrum comparisons as was in the pp collisions. Instead, as the background is removed, the underlying event fluctuations are corrected using the  $\delta p_T$  information shown in figure 6.4. The background subtraction method was matched to be the same between the analyses. The comparison to previously published ALICE  $\sqrt{s_{NN}} = 5.02$  TeV p–Pb MB spectrum [219] is seen on the right side of figure 6.17. Notably, the published paper uses an older p–Pb data measured in 2013 with fewer events than the new 2016 p–Pb dataset.

There has been no real jet  $p_T$   $R_{pA}$  publication as the  $\sqrt{s} = 5.02$  TeV pp results came so much later with a number of events and calibration for a good comparison. The publication with p–Pb MB measurements made a comparison between the  $\sqrt{s_{NN}} = 5.02$  TeV p–Pb and  $\sqrt{s} = 7$  TeV pp, by scaling the pp results

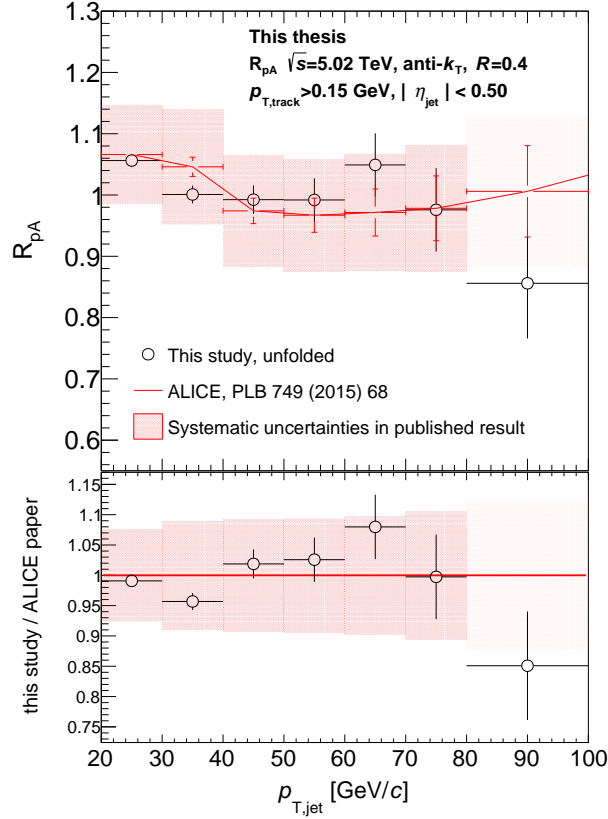


FIGURE 6.18 The jet  $p_T$   $R_{pA}$  comparison. In this figure, the p–Pb spectrum used is the same as in figure 6.17b. On the other hand, pp was matched with the p–Pb jet  $p_T$  analysis for comparison. The background was subtracted,  $\delta p_T$  was taken into account during the unfolding, and the result was unfolded using the Bayesian iterative method with three iterations. The band in the ratio shows the systematic uncertainty of the published ALICE result.

by a factor achieved by a ratio of MC simulations

$$F(p_{T,\text{jet}}) = \frac{\text{yield}(p_{T,\text{jet}})|_{\text{pp,NLO}}^{5.02 \text{ TeV,boosted}}}{\text{yield}(p_{T,\text{jet}})|_{\text{pp,NLO}}^{7 \text{ TeV}}}. \quad (6.43)$$

For my analysis, I am comparing the pp and p–Pb data with the same center-of-mass energy, so such scaling is unnecessary. For the  $R_{pA}$  comparison, all the cuts and corrections, such as the underlying event fluctuations, were matched for the pp spectrum. This ensures the same treatment and, thus, an apples-to-apples comparison between the two. The comparison of  $R_{pA}$  can be seen in figure 6.18. The systematic and statistical uncertainties are drawn for the result from the publication, with systematic uncertainty also shown in the ratio as a band. In my jet  $p_T$  analysis, I did not conduct a systematic error study. As the jet  $p_T$  spectrum I have measured for pp and p–Pb are both slightly under the published results, this will still result in a  $R_{pA}$  of 1.

## 7 RESULTS

### 7.1 Dijet invariant mass systematic uncertainties

Systematic uncertainties refer to systematic behavior which cannot be revealed by repeating the same measurement multiple times [228]. For example, changing a correction method that should yield the same outcome and comparing the outcome with the default result will give an estimate of how sensitive the measurement is for the change. If this results in a systematic difference, it is assigned as a systematic uncertainty. For this analysis, the systematics are divided into two main sources of uncertainty, tracking efficiency uncertainty and unfolding uncertainty.

Each separate source of uncertainty is tested and compared to the default setting, which is the main dijet invariant mass result introduced later in this chapter. This is done for both pp and p–Pb collisions, and separately for  $R_{pA}$ .  $R_{pA}$  is calculated so that a systematic check is tested with both pp and p–Pb simultaneously and compared to the main  $R_{pA}$  result. This way, some uncertainty is possible to cancel out, but this needs the assumption of correlation between the pp and p–Pb datasets.

#### 7.1.1 Tracking efficiency uncertainty

The performance of the tracking is estimated with a full MC detector simulation which uses realistic quality selections and tracking calculations as explained in section 4.2. During tracking, a certain percentage of particle information is lost, and this percentage is dependent on the several tracking-related cuts done to ensure good quality tracks.

As one could use a different strategy for the track quality cuts than the default, these cuts are varied for both data and MC. The variations are ultimately studied and recommended by the ALICE data processing group, and I have gathered a list of the variations in table 7.1. The effect of the variation is calculated as the ratio of “variation  $c$ ”/“default” for both data and MC, and the ratio of ratios

TABLE 7.1 List of track quality checks conducted for calculating the tracking efficiency uncertainty. If the cut is done by default, the standard value is shown in parenthesis. These are the variations that the ALICE data processing group recommends.

| Check (Standard value if available)  |
|--|
| TPC crossed rows $> 120 - \frac{5}{p_T}$ ( $> 70$ )                        |
| crossed rows / findable clusters in the TPC $> 0.9$ ( $> 0.8$ )            |
| # of clusters with TPC $dE/dx$ signal $> 0.5 \times$ # of TPC crossed rows |
| # of clusters with TPC $dE/dx$ signal $> 40$                               |
| # of clusters with TPC $dE/dx$ signal $> 60$                               |

defines the uncertainty

$$\delta c = \frac{\left. \frac{\text{variation } c}{\text{default}} \right|_{\text{data}}}{\left. \frac{\text{variation } c}{\text{default}} \right|_{\text{MC}}}, \quad (7.1)$$

which describes how well the MC simulation reacts to these variations. This number  $\delta c$  represents the tracking uncertainty for a select variation, and as each tracking cut uncertainty is uncorrelated with each other, the sources can be summed in quadrature to get total tracking uncertainty. In the end, the TPC-ITS matching efficiency is also summed in quadrature, defined as the fraction of tracks with clusters both in ITS and TPC divided by the number of tracks with clusters in TPC and is calculated by the ALICE data processing group. This is the full tracking efficiency uncertainty. This full tracking efficiency uncertainty has been collectively studied by the ALICE jet expert group, especially by Dr. Jaime Norman. It was concluded that the pp tracking efficiency uncertainty is a constant 3%, whereas the p–Pb varies as a function of track transverse momentum, as presented in the figure 7.1. The values used in this analysis are publicly available in the AliPhysics code repository [229] in the file `TrackEfficiencyConfiguration.yaml`.

The tracking efficiency uncertainty describes the uncertainty of how well we understand the amount of lost charged tracks. This loss by default is corrected using the unfolding procedure explained in detail in section 6.6. By causing extra loss of tracks, according to the tracking efficiency uncertainty, it produces a conservative estimate of the tracking capabilities of the ALICE detector and can be used to generate a new detector response matrix. This new matrix induces a stronger correction due to the extra loss of tracks. The measured results are unfolded with the default unfolding matrix and the extra track loss unfolding matrix, and then the result of both are compared. The ratio between these will show the effect of the extra tracking loss for any observable, dijet invariant mass included. In figure 7.2, I present the tracking efficiency uncertainty for my analysis for both pp and p–Pb collisions. Note how the spectrum with extra track loss is above the default result, which makes sense as the correction should be bigger with the extra loss of tracks.

It is unclear if the tracking efficiency uncertainty is correlated between the

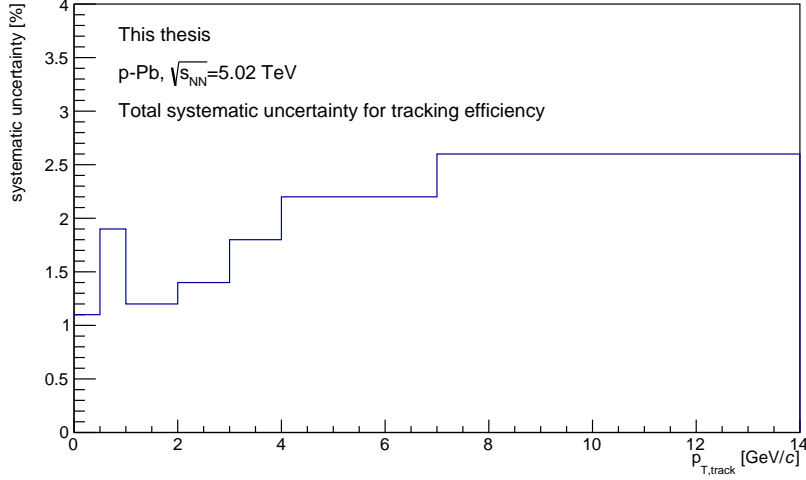


FIGURE 7.1 The tracking efficiency systematic uncertainty for individual tracks of a p–Pb event as a function of track  $p_T$ . This information generates the tracking efficiency systematics for other observables like dijet invariant mass. For tracks higher than 14 GeV, the systematic uncertainty will be equal to the value of the last bin, as seen in this figure.

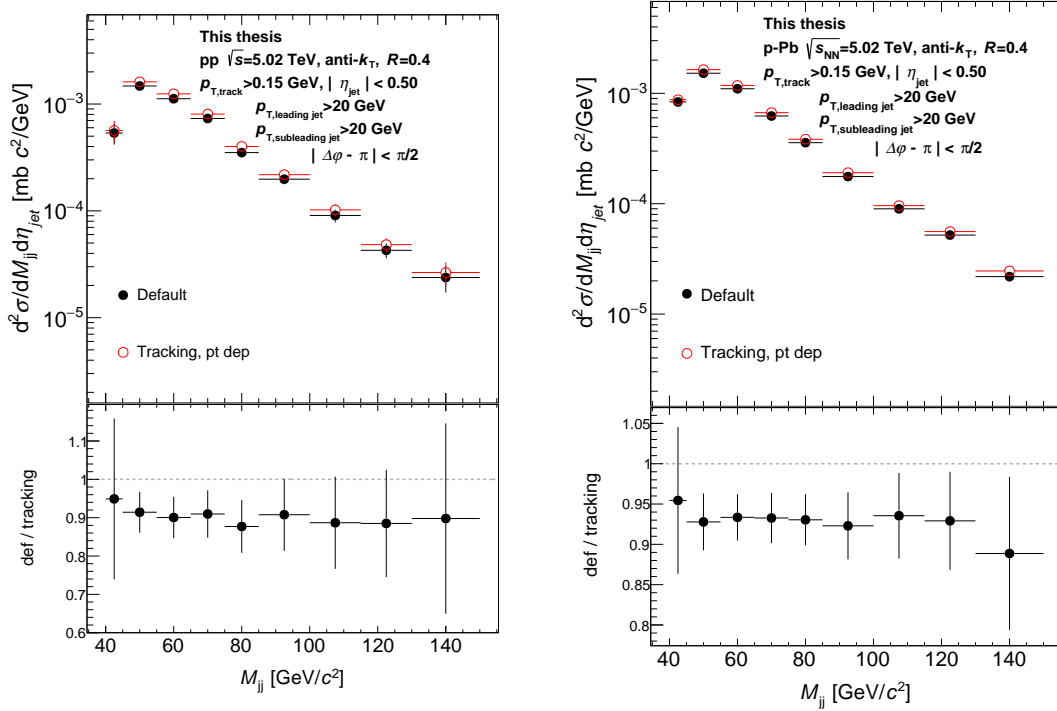
different measurements. This means that even though the systematic behavior is similar between pp and p–Pb, it cannot be trivially concluded that they would cancel each other. I studied the systematic behavior of  $R_{pA}$  by calculating the  $R_{pA}$  value by varying pp tracking while retaining the default p–Pb, and vice versa. Out of these two systematic results, I chose the larger deviation for each bin of the  $R_{pA}$  as the tracking error for  $R_{pA}$ . In figure 7.3, I show the tracking systematic error of  $R_{pA}$  for this analysis.

As this check with extra loss is much easier to do than adding extra tracks, this uncertainty is mirrored for positive and negative contributions, assuming the effect would work similarly for extra tracks. This mirroring is done for the pp and p–Pb spectrums and also the  $R_{pA}$ .

### 7.1.2 Unfolding uncertainty

The unfolding procedure contains several choices for conducting the unfolding. For example, the number of iterations or the selection of prior in Bayesian unfolding. Because of this, I have done extensive testing for different sources of uncertainties in the unfolding process. Each of the unfolding systematics sources I studied is shown individually in figure 7.5. In this section, I explain the reasoning for them all in the order they have been displayed in the figure. Ultimately, I combine all the unfolding systematics into a single unfolding systematic uncertainty.

- Unfolding performs poorly when there is a low number of measured events in certain data bins. By default, I chose to cut off the data above the dijet mass of 180 GeV. The exact value for the cut off depends on the binning and



(a) Proton–proton collisions

(b) Proton–lead collisions

FIGURE 7.2 Tracking efficiency uncertainty estimation. The ratio in the bottom part of the figures shows the deviation of the check from unity, which is set as the systematic uncertainty symmetrically for the positive and negative sides of the spectrum.

the desired amount of statistics in each bin, so I have tested the effect when the data is cut above 160 GeV instead of 180 GeV. This mainly affects the two highest bins.

- In section 6.7, a trivial closure check was made by unfolding a Monte Carlo set which was used to generate the detector response itself. Here I have separated a statistically independent set of MC from the production. The detector MC of this separate set is unfolded with the same detector response as the data and then compared with the true MC of the separated set. The difference between the unfolded detector MC and the true MC is accounted as a systematic uncertainty.
- The binning I chose for the unfolding is not unique, and I could have selected a similar yet different binning. I ran the unfolding with modified binning, and after the unfolding, I rebinned the bins in the same way so the histograms are comparable. The alternative bins are somewhat denser when compared to the default bins (shown in section 6.6) both in detector level MC and true level MC. For the systematic, the following binning was



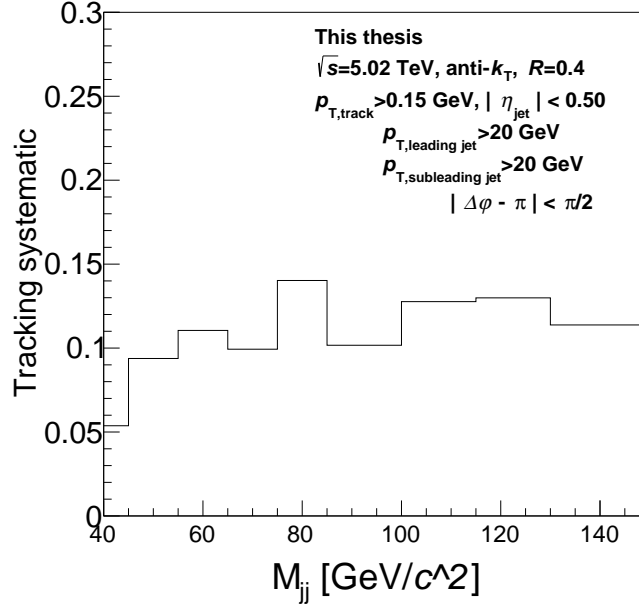
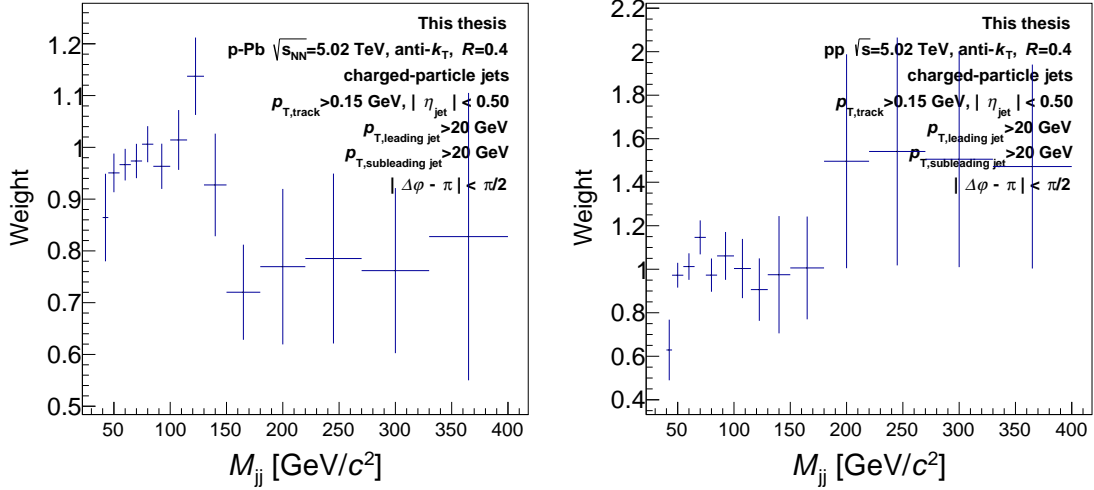


FIGURE 7.3 Tracking efficiency uncertainty for  $R_{pA}$ . This was chosen bin-by-bin as the bigger deviation from unity out of pp or p–Pb tracking efficiency uncertainty shown in figure 7.2. The uncertainty is set symmetrically for the positive and negative sides of the  $R_{pA}$ .

used:

detectorMC : [40, 43, 45, 50, 55, 60, 63, 65, 70, 75, 80, 85, 90, 95, 100,  
105, 110, 120, 130, 140, 150, 170, 180, 200]  
true MC : [40, 43, 45, 50, 55, 65, 70, 75, 85, 92, 100,  
108, 115, 122, 130, 140, 150, 200, 250].

- As explained in the previous sections, the Bayesian unfolding method requires a choice of the prior. I have used the true MC spectrum as a prior, which is a common choice in our field. However, the sensitivity of the final result for the choice of prior must be quantified. I chose the modified prior to be the unfolded data, that is to say, the default result I am presenting in this thesis. The RooUnfold program calculates the prior automatically from the unfolding matrix, assuming the usage of the true MC as the prior. Thus I have technically implemented the change by scaling the unfolding matrix with the ratio between the unfolded data and the true MC spectrum. This ratio is shown in figure 7.4. The histogram shown is used to scale the default prior by multiplying them bin-by-bin.
- There are several unfolding algorithms, two of which have been used for this analysis. The method of unfolding itself is a choice I have made, and as such, I have compared the Bayesian iterative default method to the SVD unfolding method. The SVD unfolding method uses  $k_{\text{term}} = 9$  for pp and 5 for the p–Pb.
- I have varied the number of iterations used with the Bayesian iterative un-



(a) Proton-lead prior change

(b) Proton-proton prior change

FIGURE 7.4 The ratio between the unfolded data and the true MC, which is then used to scale the unfolding matrix, thus changing the prior of the unfolding process.

folding method. I have chosen the number of iterations because the output should not change significantly with the increasing number of iterations, so by design, this source is small but important to test. In this test, the number of iterations has been changed  $\pm 1$ .

### 7.1.3 Total systematic uncertainty

Combining the systematic uncertainties is a multi-step process. Each systematic source listed before is defined as the bin-by-bin deviation from unity. The unfolding systematics are combined together with the equation

$$\delta_{\text{unfolding}} = \sqrt{\frac{\sum_{i \in \text{unf syst}}^{N^{\text{tot unf}}} \delta_i^2}{N^{\text{tot unf}}}}, \quad (7.2)$$

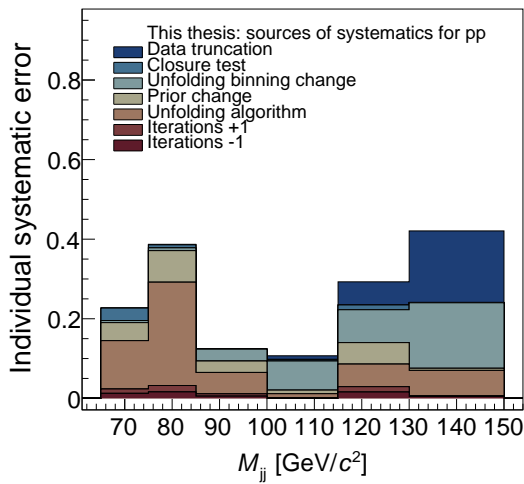
similarly as previous jet publications [230]. After combining, both the total unfolding systematic and the tracking efficiency uncertainty are smoothed with the help of the ROOT [231] `TH1::Smooth` function, which uses the 353QH smoothing algorithm twice. 353QH does running medians of three, running medians of five, running medians of three again, and finally, a quadratic interpolation. This algorithm is explained in detail in the reference [232, p. 295]. After smoothing the tracking and unfolding systematics, the total systematic uncertainty is calculated bin-by-bin by taking a square root of the sum of squares. I present the final systematic uncertainties in figure 7.6.

I estimated the total error for the uncertainty of measured cross sections. The cross sections and errors were reported in section 4.1, and the errors are com-

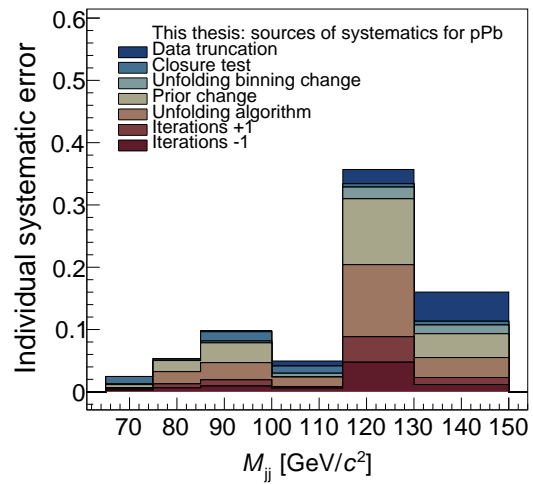
bined squarely

$$\sqrt{\left(\sqrt{\delta\sigma_{pp,\text{stat}}^2 + \delta\sigma_{pp,\text{syst}}^2}/\sigma_{pp}\right)^2 + (\delta\sigma_{pPb,\text{syst}}/\sigma_{pPb})} = 0.038, \quad (7.3)$$

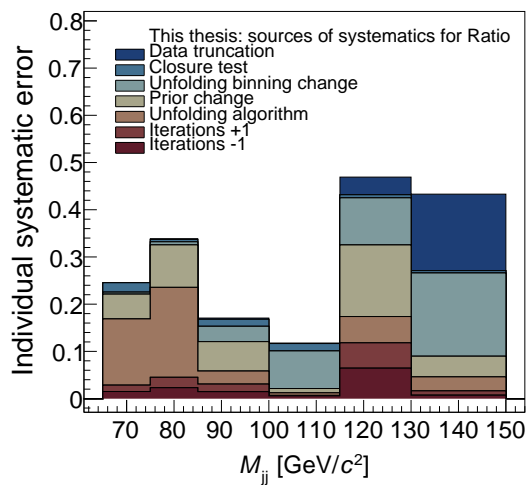
where I have first combined the statistical and systematic errors of pp cross section squarely, after which I combined the total error of pp and p-Pb, resulting in an error of 3.8%.



(a) Proton–proton

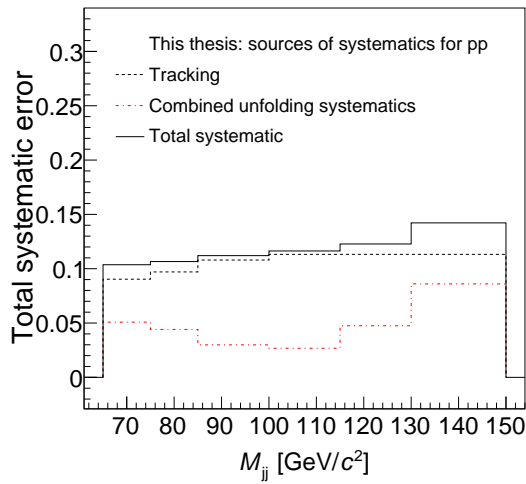


(b) Proton–lead

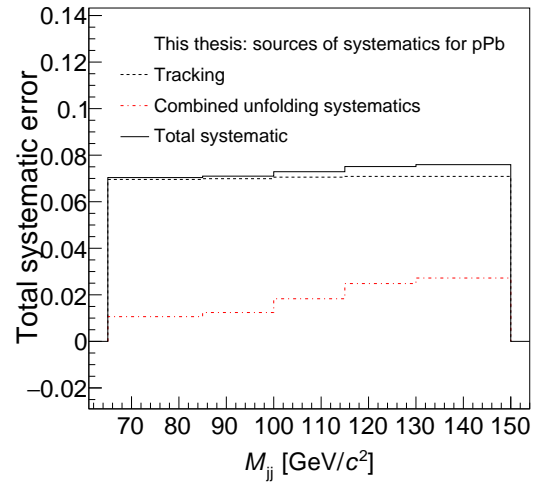


(c) Nuclear modification factor

FIGURE 7.5 The unfolding related systematics are depicted individually on a stacked histogram. The sum of these histograms *does not* reflect the total unfolding systematic. Total unfolding systematic can be found in figure 7.6



(a) Proton-proton



(b) Proton-lead

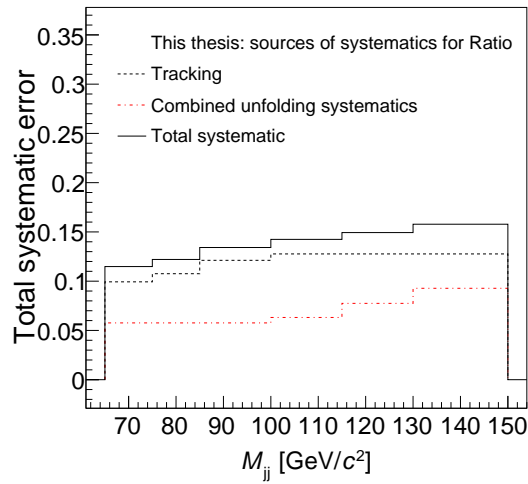
(c)  $R_{pA}$ 

FIGURE 7.6 The smoothed tracking and total unfolding systematics, along with the total systematic uncertainty.

## 7.2 Dijet invariant mass MC model comparisons

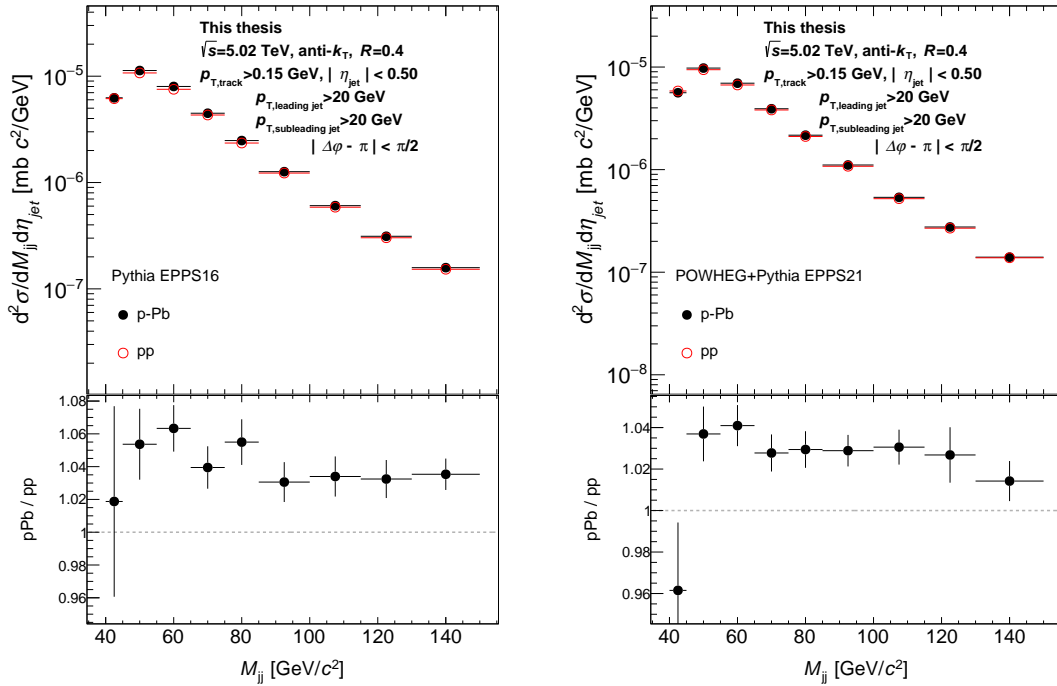
I ran two MC simulations to obtain a better physics interpretation of the measured dijet mass distributions. I studied how big of an effect would the rapidity shift and the use of a nuclear PDF have on the final results. The rapidity shift is needed as the proton has more energy than a nucleon in the lead, as explained in section 4. As protons traverse towards the negative direction in the ALICE coordinate system, the push is  $\Delta y = -0.465$  [233, 234].

I ran two productions. First, standalone Pythia with EPPS16 nPDF [235], and POWHEG+Pythia with EPPS21 nPDF [2]. The POWHEG calculates the hard interaction at the NLO level, whereas Pythia effectively accounts for the higher orders by tuning the parton shower [100].

I used Pythia to simulate events in eight different  $\hat{p}_T$  bins, explained in section 2.5.1, to have a high number of events also in the rare kinematically high regions of the hard collisions. The first bin started at 15–30 GeV, and from there, 30–40 GeV, 40–65 GeV, 65–90 GeV, 90–120 GeV, 120–150 GeV, 150–200 GeV, and the last bin had a  $\hat{p}_T$  minimum of 200 GeV with no upper limit. I scaled each histogram in a given  $\hat{p}_T$  bin with the cross section corresponding to that bin, alongside the number of events.

Unlike Pythia, POWHEG is not run in distinct  $\hat{p}_T$  bins, but the rare events are instead artificially made more probable during the generation of the events. This way, one will receive a broader set of hard interactions but with unrealistic distributions. This is fixed by weighting each histogram event by event with the inverse of the enhancement of the current event. The POWHEG+Pythia simulation uses parton shower and hadronization algorithms from Pythia. Because, by default, Pythia has leading order matrix elements for calculating the hard scattering, the parton shower of Pythia is tuned to match higher-order interactions. Since the POWHEG uses NLO matrix elements, the Pythia showers need to be matched to the POWHEG NLO calculations to avoid double counting [100]. Detailed settings for Pythia and the POWHEG+Pythia are shown in appendices C.2 and C.3.

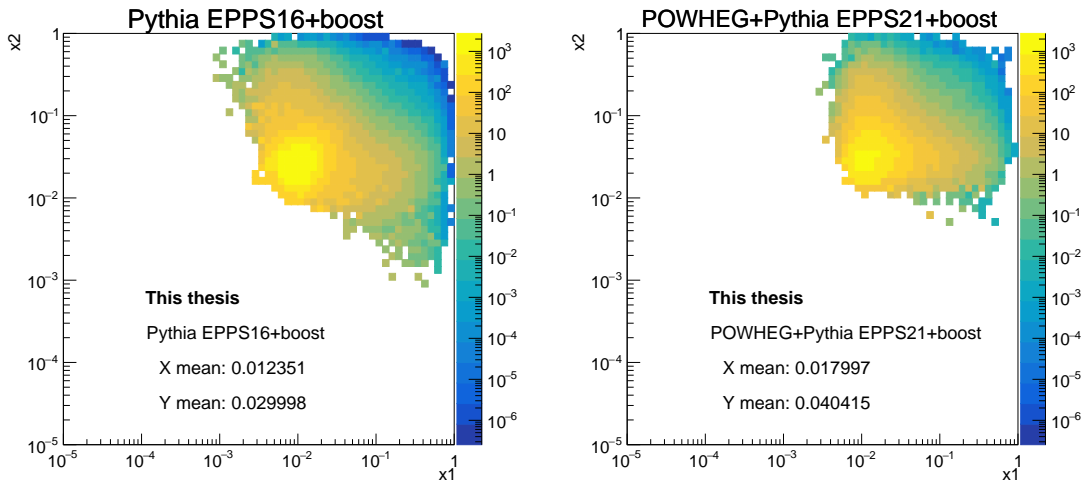
In figure 7.7, the comparison between nonmodified simulated pp events and the rapidity shifted PDF+nPDF pp events can be seen. There seems to be a slight enhancement of jets in the modified simulated pp collisions. I have drawn the partonic  $(x_1, x_2)$  distributions of the hardest interaction for events that have two jets with at least 20 GeV transverse momentum in figure 7.8. The median of the distributions are of the order of 0.01–0.05. Comparing these values to the previously shown EPPS21 publication in figure 2.4, where they show the modification for gluon distribution, it seems that the simulations produce dijets in the anti-shadowing enhancement region. The enhancement in figure 7.7 is understandable as most of the dijet events are from the anti-shadowing region of the nuclear PDFs.



(a) Standalone Pythia Monash tune

(b) POWHEG+Pythia

FIGURE 7.7 Monte Carlo results which compare default simulated pp events with rapidity boosted PDF+nPDF pp events.



(a) Standalone Pythia Monash tune

(b) POWHEG+Pythia

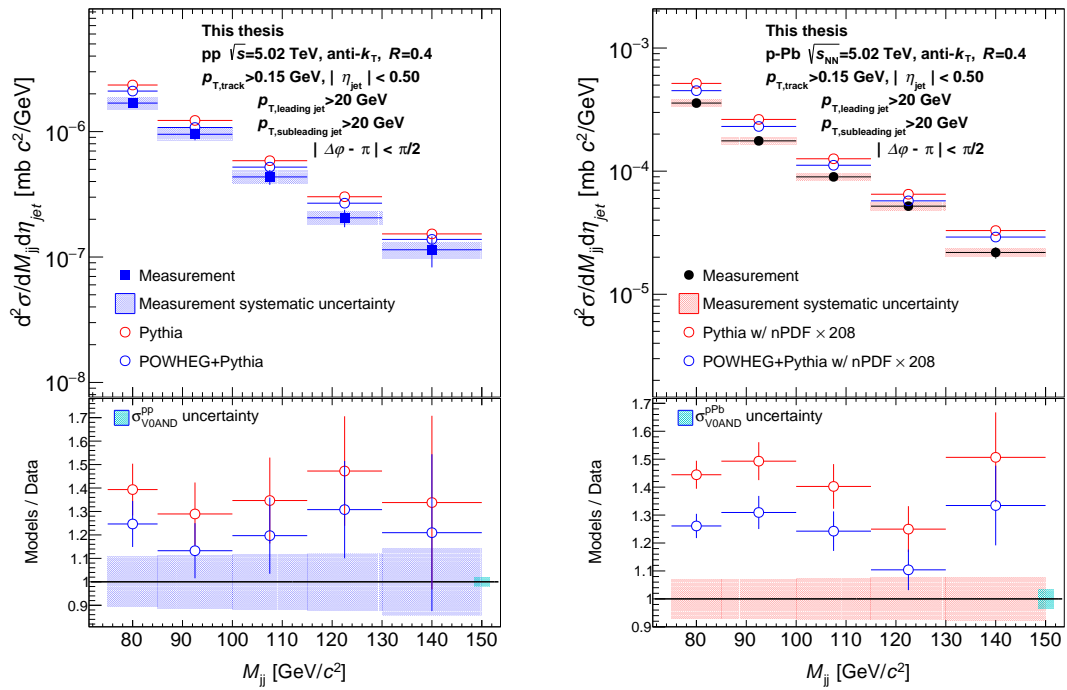
FIGURE 7.8 The  $(x_1, x_2)$  histogram of the rapidity shifted PDF+nPDF Pythia and POWHEG+Pythia productions.

### 7.3 Dijet invariant mass and the nuclear modification factor

In figure 7.9, I have drawn the dijet invariant mass spectrum with the aforementioned systematic uncertainties included as colorful bars. I have also included a comparison to the Pythia and POWHEG+Pythia MC results, which were introduced in section 7.2. I scaled the MC spectrums with the atomic number of lead for the comparisons with p–Pb data. According to the comparison, both MC models overshoot the measurement, but POWHEG+Pythia is consistently closer. Qualitatively similar behavior has been seen in previous studies where Pythia8 tunes overshoot the measurement [113], especially tune Monash [227], which is the tune I also used to generate the Pythia events.

In figure 7.10, I present the measured pp and p–Pb spectrum again, along with the nuclear modification factor  $R_{pA}$ . In this figure, the pp spectrum is scaled with the atomic number of lead. The ratio of these spectra is automatically the nuclear modification factor as shown in equation (6.9), which I have drawn in the bottom panel of the figure. In the figure, I also show the systematic error of the  $R_{pA}$  drawn as a colored bar alongside the two MC models. The colored band of the MC models includes the statistical uncertainties. The two MC  $R_{pA}$  are almost perfectly on top of each other, which shows that there is no big difference for this observable between the showering of Pythia and the NLO calculations of POWHEG. Within uncertainties, the data and the models agree with each other, which means that the systematic and statistical uncertainties in the measurement are too large to make a definite conclusion about the enhancement seen in the MC. The absence of modification is in line with the jet and dijet studies previously conducted in similar kinematical ranges, such as shown in figure 6.18 or in [70, 71, 236]. This figure is an updated version of ALICE preliminary result in [237].





(a) Proton-proton spectrum.

(b) Proton-lead spectrum.

FIGURE 7.9 Dijet invariant mass spectrum with comparisons to two MC models.

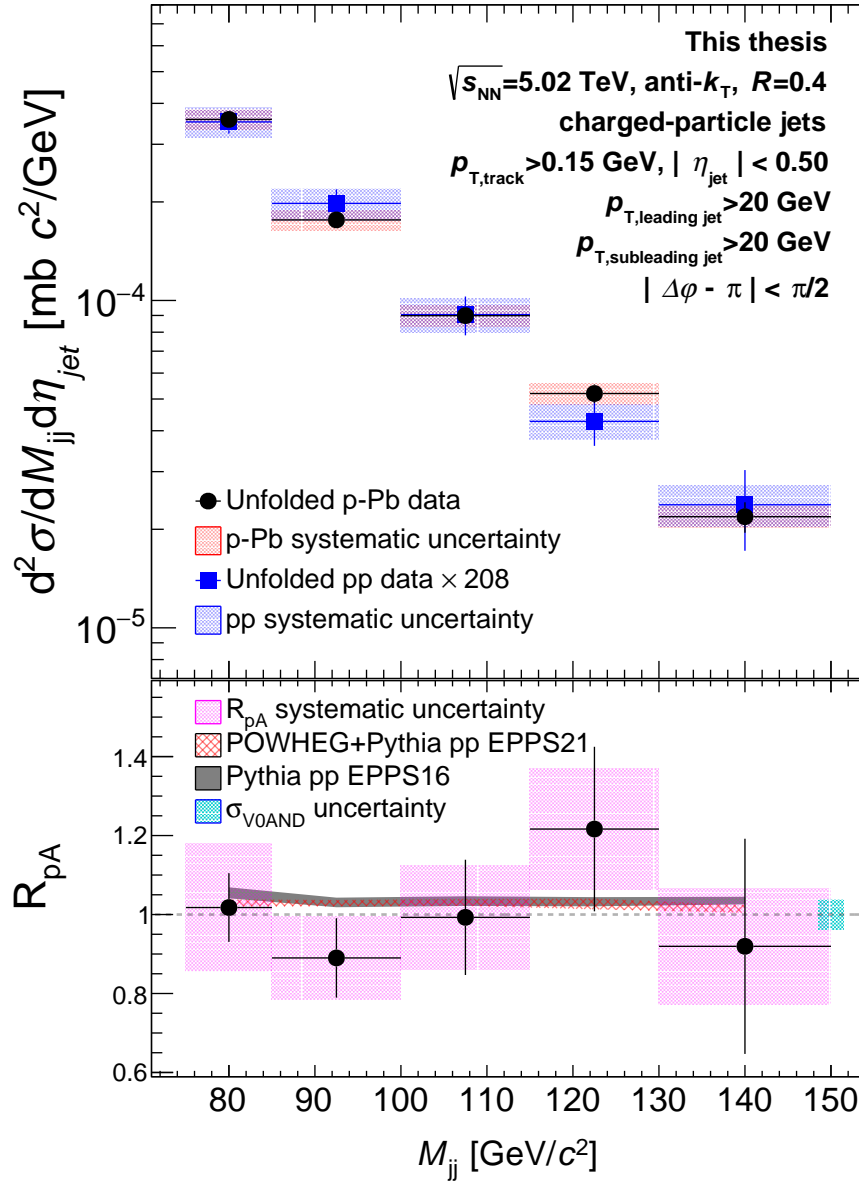


FIGURE 7.10 The dijet invariant mass for  $pp \times A$  and  $p\text{-Pb}$  at  $\sqrt{s_{\text{NN}}} = 5.02 \text{ TeV}$ , including also model comparisons with Pythia and POWHEG+Pythia for the  $R_{\text{pA}}$ .

## 8 CONCLUSIONS AND OUTLOOK

In this thesis, I presented the analysis and study of the dijet invariant mass spectrum reconstructed from charged particles in proton–proton and proton–lead collisions at  $\sqrt{s_{\text{NN}}} = 5.02$  TeV center-of-mass energy measured with the ALICE detector. I reported the dijet invariant mass spectrums for pp and p–Pb in the mass range of 75 – 150 GeV/ $c^2$ , alongside the nuclear modification factor for the dijet invariant mass. There is no modification for the entire available range of the spectrum, which is to be expected in the context of previous jet nuclear modification factor studies in the same kinematical range. According to Pythia and POWHEG+Pythia Monte Carlo simulations, there is a small enhancement of the spectrum. This enhancement could be due to the fact that the events which produce a dijet are from the anti-shadowing region of the lead nuclear PDF. Both models agree with each other and agree with the measurement within the margin of uncertainty. To experimentally confirm the enhancement, a large amount of statistics is needed. Furthermore, the systematical uncertainties would need to be greatly improved, which will be challenging as the dijet invariant mass is sensitive to the tracking efficiency uncertainty, which is significant. In the future, changing the MC generator used to unfold could be used as an additional test on how dependent the results are for this. It would also be beneficial to consider comparisons to several different Pythia tunes and possibly other MC generators as well.

A natural next step would be to measure the centrality dependency of the dijet invariant mass in Pb–Pb collisions. The nuclear modification factor for single jet studies and dijet studies have shown significant modifications, so this would also be the expected result for dijet invariant mass observable. However, how strong the dijet mass suppression would be is an interesting question as the dijet could have a longer path length inside the medium than in previous single jet measurements.

Dijets could also be used for event selection. Events could be binned according to a presence of a dijet with a certain mass, and the evolution of collective behavior could be studied, similarly as has been done previously with jet  $p_{\text{T}}$  [238]. This would be interesting as the dijet mass is a measure of the virtuality of

the hard interaction, unlike single jets, which describe the virtuality of the single parton. The LHC Run 3 period provides a good opportunity for the dijet analysis as high-energy dijets are rare, and the data-taking rate during Run 3 increases significantly to Run 2.



## APPENDIX A JET $P_T$ ANALYSIS

In this appendix, I present the single jet  $p_T$  spectra for the same events as in my thesis's dijet invariant mass  $M_{jj}$  analysis. I use a transverse momentum lower cut of  $p_{T,min} = 7$  GeV for the jets. Including lower momentum jets in the analysis negatively impacts the unfolding.

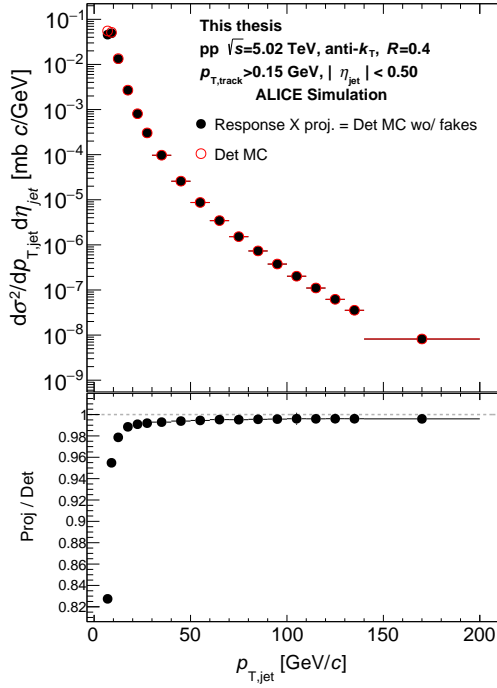
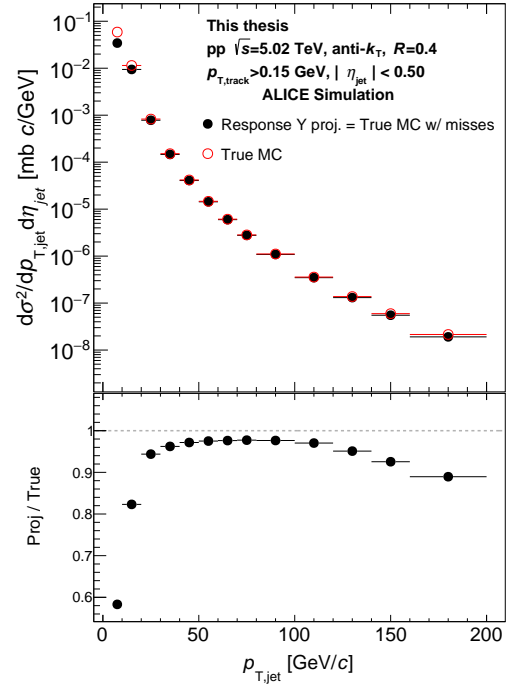
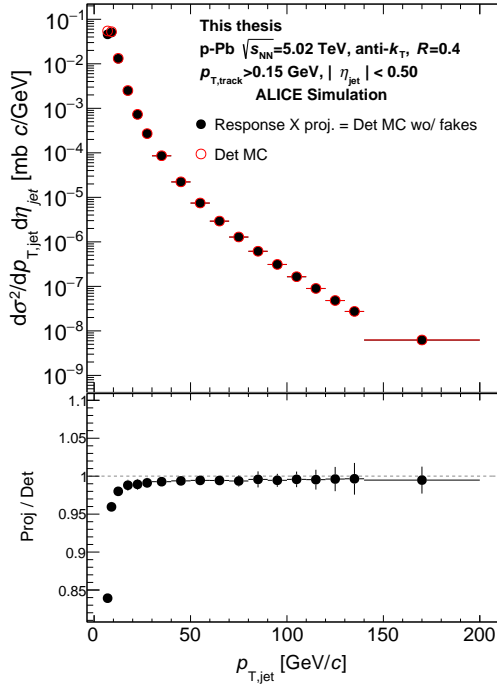
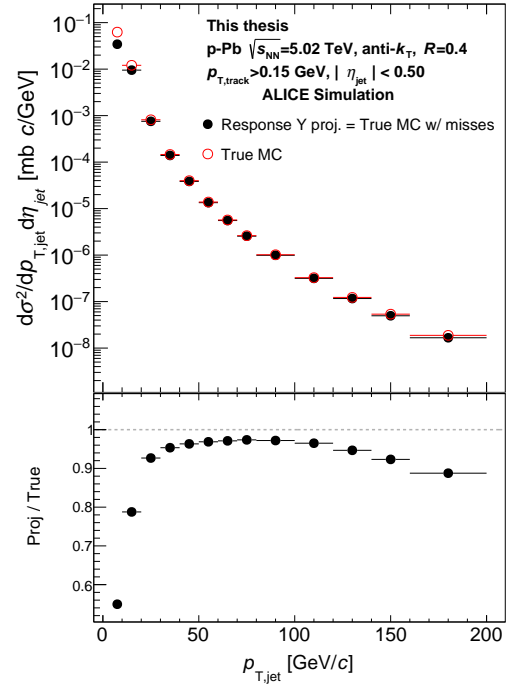
As I explained for both single jets and dijets in section 6.5, each true MC level jet is matched with a detector MC level jet in the  $\eta$ - $\phi$  plane. The closest detector jet within the  $\Delta R < 0.3$  range is chosen as a pair for the true jet. If no detector jet is found as the pair for the true jet, this true jet will become a miss. Conversely, if detector jets are left without a true jet pair, they are marked as a fake jet. Both fakes and misses are shown for jet  $p_T$  in figures A.1 for pp and A.2 for p-Pb.

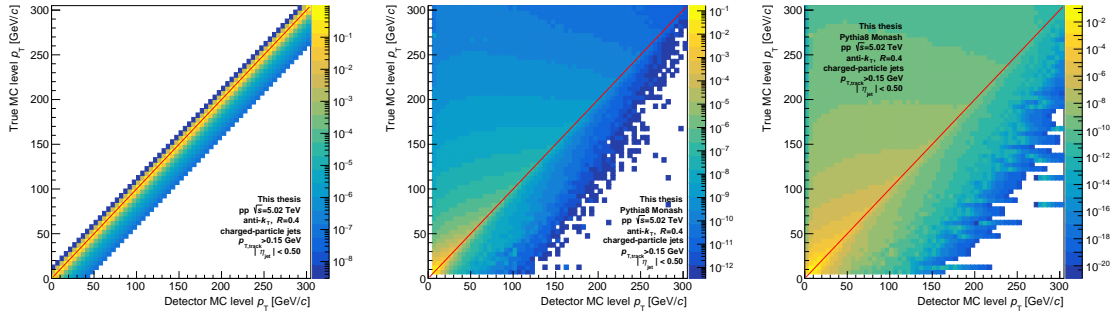
I estimate the impact of background fluctuations as explained in the main text, section 6.4. As in the dijet analysis, I use the  $\delta p_T$  histogram to form a 2D histogram where the 1D histogram is copied in each y-axis slice so that the bin of the 1D histogram which is centered around zero is in the diagonal of the 2D histogram. This 2D histogram can be seen for both pp and p-Pb in figures A.3a and A.4a. I form the detector response for jet  $p_T$  out of the true-detector jet pairs, and the detector response can be seen in figures A.3b and A.4b.

I combine the two response matrices using a matrix multiplication, which can be seen in figures A.3c and A.4c, and then rebinned with same, or similar, binning as in the publications. For the jet  $p_T$  the following binning was used:

detector MC : [2, 5, 10, 20, 30, 40, 50, 60, 70, 80, 100, 120, 140, 160, 200, 250, 300, 350],  
true MC : [2, 4, 6, 8, 10, 15, 20, 25, 30, 40, 50, 60, 70, 80, 90, 100,  
110, 120, 130, 140, 200, 250, 300],

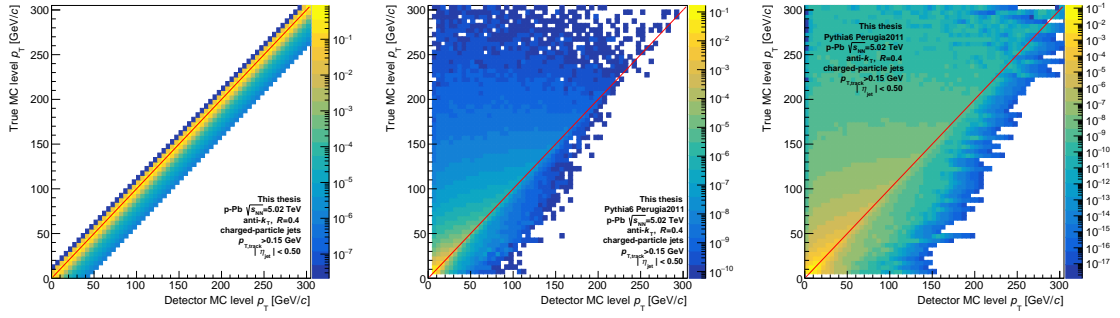
and the combined matrix with the final binning is shown in figure A.5.

(a) Jet  $p_T$  fakes for the pp.(b) Jet  $p_T$  misses for the pp.FIGURE A.1 Fakes and misses for the jet  $p_T$  spectrum in pp collisions.(a) Jet  $p_T$  fakes for the p-Pb.(b) Jet  $p_T$  misses for the p-Pb.FIGURE A.2 Fakes and misses for the jet  $p_T$  spectrum in p-Pb collisions.



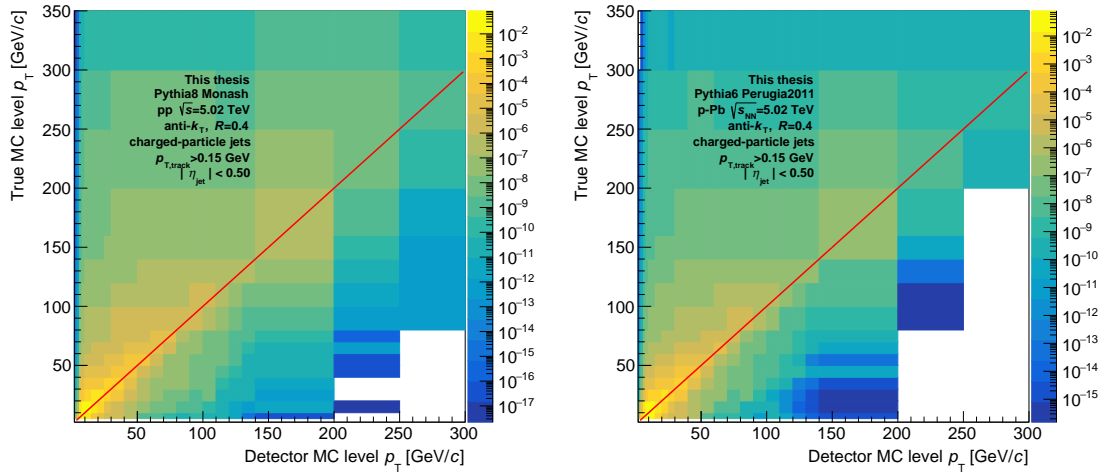
(a) UE fluctuations (b) Detector response. (c) Total unfolding matrix

FIGURE A.3 The unfolding matrices for the jet  $p_T$  in proton–proton collisions.



(a) UE fluctuations (b) Detector response. (c) Total unfolding matrix

FIGURE A.4 The unfolding matrices for the jet  $p_T$  in proton–lead collisions.



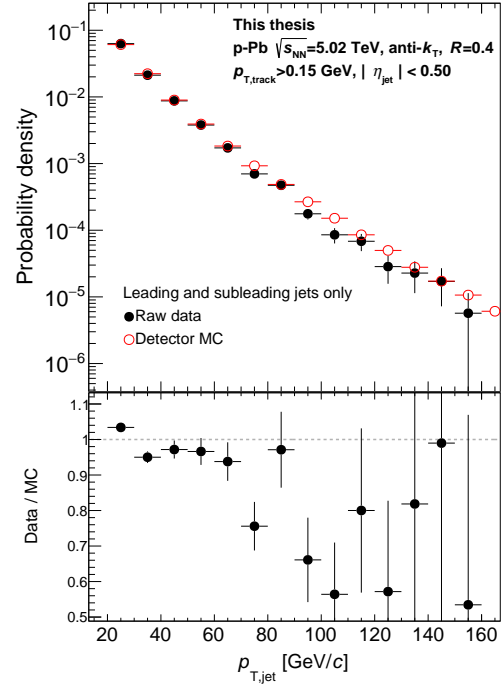
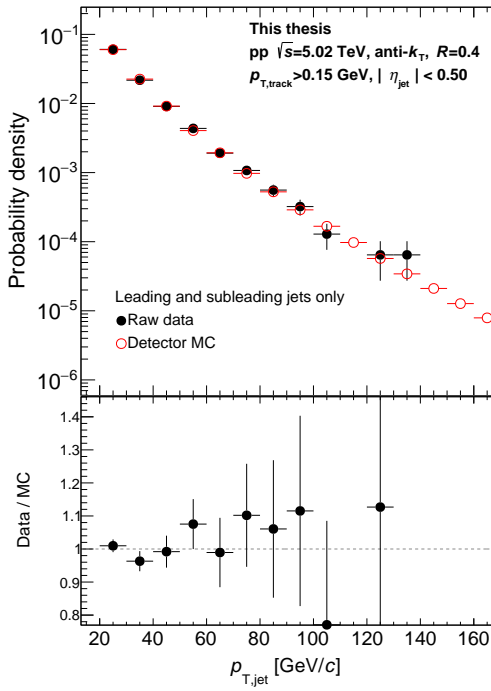
(a) Proton–proton (b) Proton–lead

FIGURE A.5 The rebinned combined response matrix for jet  $p_T$ .

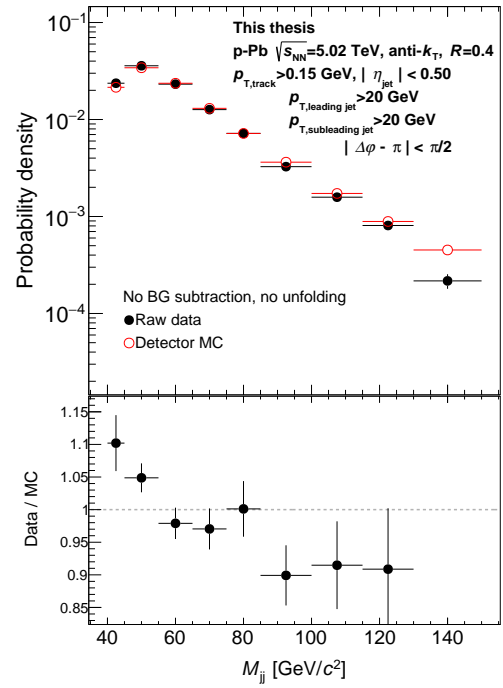
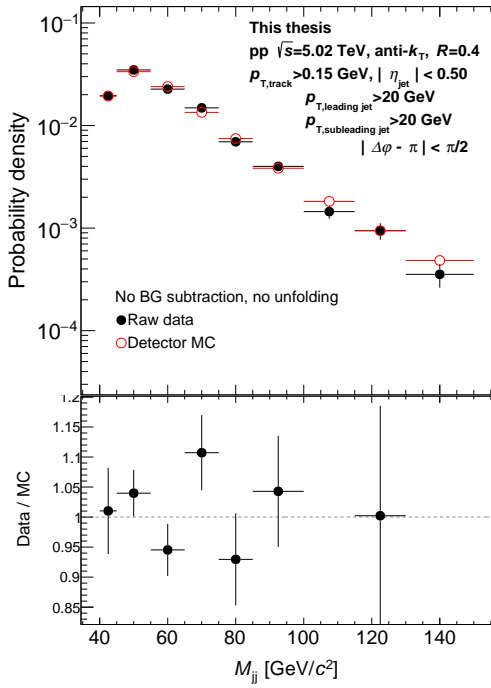


## APPENDIX B RAW DATA TO DETECTOR MC COMPARISONS

In this section, I present comparisons between the uncorrected data and detector-simulated MC. No background subtraction was made for these figures. This is to show that the MC can represent the characteristics of the dijet physics reasonably well, and should be the case for MC which is used in unfolding. The figures are scaled to a probability density, as the behavior of the spectra is an interesting aspect here. Figure B.1 shows the jet  $p_T$  of the leading and subleading jets which are used in the dijet invariant mass analysis. Figure B.2 shows the  $\Delta\phi$  and  $\Delta\eta$  distributions to show if the geometry of the dijets differs. The overall agreement between raw data and detector MC is good, especially for pp. p-Pb has slight deviations, but can be expected as the MC which is used to unfold p-Pb is a pp simulation.



(a)  $p_T$  of leading and subleading jets for pp. (b)  $p_T$  of leading and subleading jets for p-Pb.



(c)  $p_T$  of the dijet system for pp.

(d)  $p_T$  of the dijet system for p-Pb.

FIGURE B.1 Shape comparisons between raw data and detector MC.

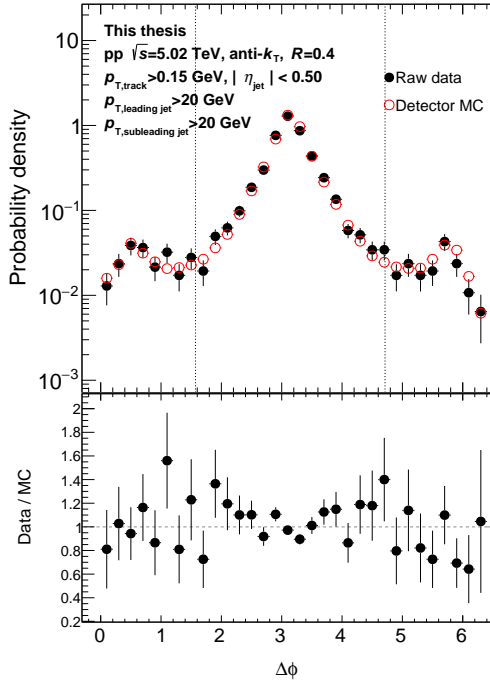
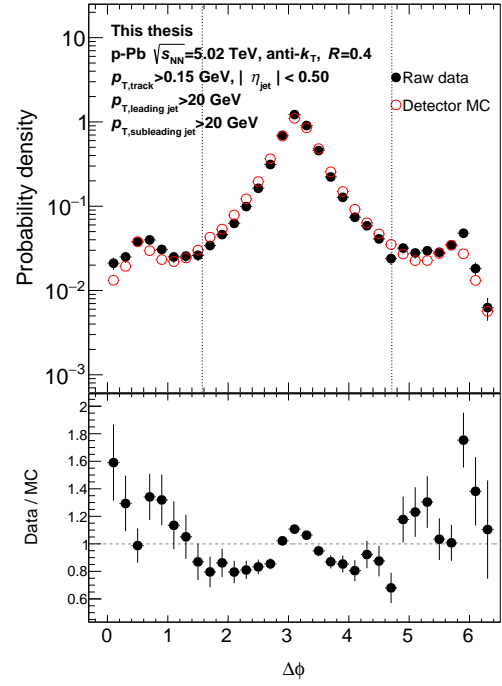
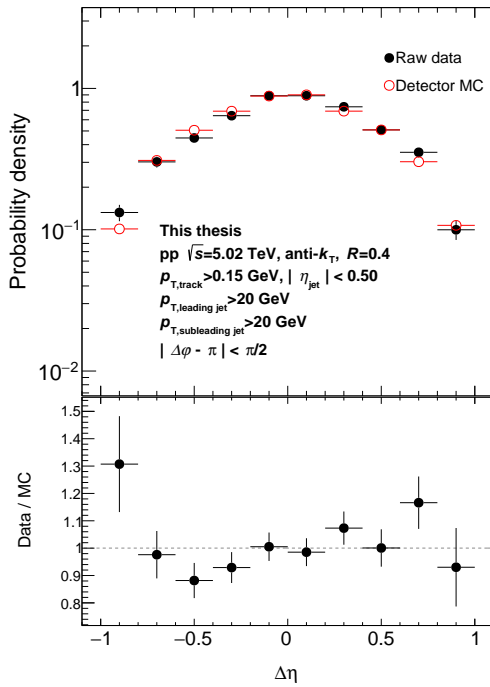
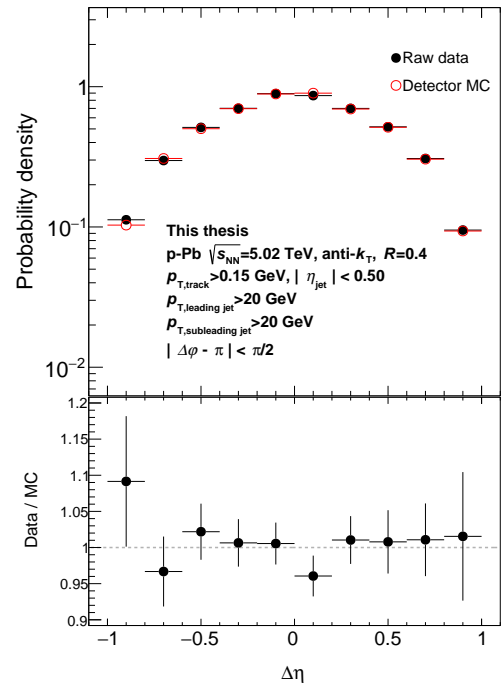
(a)  $\Delta\phi$  for the pp.(b)  $\Delta\phi$  for the p-Pb.(c)  $\Delta\eta$  for the pp.(d)  $\Delta\eta$  for the p-Pb.

FIGURE B.2 Shape comparisons between raw data and detector MC.

## APPENDIX C LIST OF MONTE CARLO GENERATOR SETTINGS

### APPENDIX C.1 AMPT settings

AMPT was run with default settings that come with the package, except for the following:

```
5500 ! EFRM (sqrt(S_NN) in GeV if FRAME is CMS)
208  ! IAP (projectile A number)
82   ! IZP (projectile Z number)
208  ! IAT (target A number)
82   ! IZT (target Z number)
0.30 ! PARJ(41) parameter a in Lund symmetric splitting function
1    ! Flag for random orientation of reaction plane
```

### APPENDIX C.2 Pythia settings

The default run with normal PDF.

```
Random:setSeed = on
Beams:idA = 2212
Beams:idB = 2212
Beams:eCM = 5020.
HardQCD:all = on
PhaseSpace:mHatMin = 0.0
PhaseSpace:mHatMax = -1.0
ParticleDecays:limitTau0 = On
ParticleDecays:tau0Max = 10.0
Tune:pp = 14
```

The run with nPDF used the same settings except

```
Beams:frameType = 2
Beams:eA = 4000.
Beams:eB = 1576.9231
PDF:useHardNPFB = on
PDF:nPDFSetB = 3
PDF:nPDFBeamB = 100822080
```

### APPENDIX C.3 POWHEG-BOX settings

The default run with normal PDF.

```

ih1 1
ih2 1
ebeam1 2510d0
ebeam2 2510d0
bornktmin 1d0
bornsuppfact 90d0
lhans1 14600
lhans2 14600
use-old-grid 1
use-old-ubound 1
ncall1 20000
itmx1 5
ncall2 20000
itmx2 5
foldcsi 5
foldy 5
foldphi 2
nubound 500000
withnegweights 0
doublefsr 1
par_diexp 4
par_dijexp 4
par_2gsupp 4

```

**The run with nPDF used the same settings except**

```

lhans2 904400
QCDLambda5 0.25

```

**In addition, Pythia, which was used for the showering process, was initialized with the following settings**

```

Next:numberShowLHA = 1
Next:numberShowInfo = 1
Next:numberShowProcess = 1
Next:numberShowEvent = 1
Main:timesAllowErrors = 10
Init:showChangedSettings = on
Init:showChangedParticleData = off
Beams:frametype = 4
Beams:LHEF = pwgevents.lhe
POWHEG:nFinal = 2
PartonLevel:MPI = on
111:mayDecay = on
310:mayDecay = off
3122:mayDecay = off
3112:mayDecay = off

```

```
3212:mayDecay = off
3222:mayDecay = off
3312:mayDecay = off
3322:mayDecay = off
3334:mayDecay = off
POWHEG:veto = 1
POWHEG:vetoCount = 10000
POWHEG:pThard = 2
POWHEG:pTemt = 0
POWHEG:emitted = 0
POWHEG:pTdef = 1
POWHEG:MPIveto = 0
POWHEG:QEDveto = 2
Tune:preferLHAPDF = 2
Tune:pp = 5
PDF:pSet = 9
Random:setSeed = on
SpaceShower:pTmaxMatch = 2
TimeShower:pTmaxMatch = 2
```

Furthermore, in the main Pythia C++ program, the PowhegHooks was used.

```
Pythia8::PowhegHooks *powhegHooks = NULL;
powhegHooks = new Pythia8::PowhegHooks();
pythia8->setUserHooksPtr(powhegHooks);
```

## BIBLIOGRAPHY

- [1] Matteo Cacciari, Gavin P. Salam, and Gregory Soyez. “FastJet User Manual”. In: *Eur.Phys.J. C* 72 (2012), p. 1896. DOI: 10.1140/epjc/s10052-012-1896-2. arXiv: 1111.6097 [hep-ph].
- [2] Kari J. Eskola et al. “EPPS21: a global QCD analysis of nuclear PDFs”. In: *Eur. Phys. J. C* 82.5 (2022), p. 413. DOI: 10.1140/epjc/s10052-022-10359-0. arXiv: 2112.12462 [hep-ph].
- [3] Particle Data Group collaboration. “Review of Particle Physics”. In: *PTEP* 2022 (2022), p. 083C01. DOI: 10.1093/ptep/ptac097.
- [4] Frank Wilczek. “Quantum field theory”. In: *Rev. Mod. Phys.* 71 (1999), S85–S95. DOI: 10.1103/RevModPhys.71.S85. arXiv: hep-th/9803075.
- [5] R. P. Feynman. “Mathematical formulation of the quantum theory of electromagnetic interaction”. In: *Phys. Rev.* 80 (1950). Ed. by L. M. Brown, pp. 440–457. DOI: 10.1103/PhysRev.80.440.
- [6] R. Harris. *Nonclassical Physics: Beyond Newton’s View*. Addison Wesley Longman, 1998. ISBN: 9780201834369.
- [7] Wojciech Florkowski. *Phenomenology of Ultra-Relativistic Heavy-Ion Collisions*. Mar. 2010. ISBN: 978-981-4280-66-2.
- [8] M.E. Peskin and D.V. Schroeder. *An Introduction To Quantum Field Theory*. Frontiers in Physics. Avalon Publishing, 1995. ISBN: 9780813345437.
- [9] Rajan Gupta. “Introduction to lattice QCD: Course”. In: *Les Houches Summer School in Theoretical Physics, Session 68: Probing the Standard Model of Particle Interactions*. July 1997, pp. 83–219. arXiv: hep-lat/9807028.
- [10] Claudia Ratti. “Lattice QCD and heavy ion collisions: a review of recent progress”. In: *Rept. Prog. Phys.* 81.8 (2018), p. 084301. DOI: 10.1088/1361-6633/aabb97. arXiv: 1804.07810 [hep-lat].
- [11] K. J. Eskola and H. Honkanen. “A Perturbative QCD analysis of charged particle distributions in hadronic and nuclear collisions”. In: *Nucl. Phys. A* 713 (2003), pp. 167–187. DOI: 10.1016/S0375-9474(02)01304-0. arXiv: hep-ph/0205048.
- [12] Szabolcs Borsanyi et al. “QCD Crossover at Finite Chemical Potential from Lattice Simulations”. In: *Phys. Rev. Lett.* 125.5 (2020), p. 052001. DOI: 10.1103/PhysRevLett.125.052001. arXiv: 2002.02821 [hep-lat].
- [13] Fernando Antonio Flor, Gabrielle Olinger, and Rene Bellwied. “Flavour and Energy Dependence of Chemical Freeze-out Temperatures in Relativistic Heavy Ion Collisions from RHIC-BES to LHC Energies”. In: *Phys. Lett. B* 814 (2021), p. 136098. DOI: 10.1016/j.physletb.2021.136098. arXiv: 2009.14781 [nucl-ex].

- [14] Anton Andronic et al. “Decoding the phase structure of QCD via particle production at high energy”. In: *Nature* 561.7723 (2018), pp. 321–330. DOI: 10.1038/s41586-018-0491-6. arXiv: 1710.09425 [nucl-th].
- [15] J. Cleymans et al. “Comparison of chemical freeze-out criteria in heavy-ion collisions”. In: *Phys. Rev. C* 73 (2006), p. 034905. DOI: 10.1103/PhysRevC.73.034905. arXiv: hep-ph/0511094.
- [16] A. Andronic, P. Braun-Munzinger, and J. Stachel. “Hadron production in central nucleus-nucleus collisions at chemical freeze-out”. In: *Nucl. Phys. A* 772 (2006), pp. 167–199. DOI: 10.1016/j.nuclphysa.2006.03.012. arXiv: nucl-th/0511071.
- [17] “The ALICE experiment - A journey through QCD”. In: (Nov. 2022). arXiv: 2211.04384 [nucl-ex].
- [18] F. Karsch, E. Laermann, and A. Peikert. “The Pressure in two flavor, (2+1)-flavor and three flavor QCD”. In: *Phys. Lett. B* 478 (2000), pp. 447–455. DOI: 10.1016/S0370-2693(00)00292-6. arXiv: hep-lat/0002003.
- [19] H. U. Bengtsson and G. Ingelman. “The Lund Monte Carlo for High  $p_T$  Physics”. In: *Comput. Phys. Commun.* 34 (1985), p. 251. DOI: 10.1016/0010-4655(85)90003-7.
- [20] Szabolcs Borsanyi. “Thermodynamics of the QCD transition from lattice”. In: *Nucl. Phys. A* 904-905 (2013). Ed. by Thomas Ullrich, Bolek Wyslouch, and John W. Harris, pp. 270c–277c. DOI: 10.1016/j.nuclphysa.2013.01.072. arXiv: 1210.6901 [hep-lat].
- [21] Pasi Huovinen and Pter Petreczky. “QCD Equation of State and Hadron Resonance Gas”. In: *Nucl. Phys. A* 837 (2010), pp. 26–53. DOI: 10.1016/j.nuclphysa.2010.02.015. arXiv: 0912.2541 [hep-ph].
- [22] Y. Aoki et al. “The Order of the quantum chromodynamics transition predicted by the standard model of particle physics”. In: *Nature* 443 (2006), pp. 675–678. DOI: 10.1038/nature05120. arXiv: hep-lat/0611014.
- [23] Eemeli Annala et al. “Evidence for quark-matter cores in massive neutron stars”. In: *Nature Phys.* 16.9 (2020), pp. 907–910. DOI: 10.1038/s41567-020-0914-9. arXiv: 1903.09121 [astro-ph.HE].
- [24] Reinhard Stock. “Relativistic nucleus nucleus collisions: From the BEVALAC to RHIC.” In: *J. Phys. G* 30 (2004). Ed. by Hans Georg Ritter and Xin-Nian Wang, S633–S648. DOI: 10.1088/0954-3899/30/8/001. arXiv: nucl-ex/0405007.
- [25] A. M. Baldin and I. N. Semenyushkin. “Twenty years of the synchrotron of the JINR High-Energy Physics Laboratory.” In: *Soviet Atomic Energy* 43 (1977), pp. 1146–1147. DOI: 10.1007/bf01117960.
- [26] R.A. Beth and C. Lasky. “The Brookhaven Alternating Gradient Synchrotron”. In: *Science* 128.3336 (1958), pp. 1393–1401. DOI: 10.1126/science.128.3336.1393.



- [27] NA50 collaboration. "Evidence for deconfinement of quarks and gluons from the  $J/\psi$  suppression pattern measured in Pb + Pb collisions at the CERN SPS". In: *Phys. Lett. B* 477 (2000), pp. 28–36. DOI: 10.1016/S0370-2693(00)00237-9.
- [28] NA44 collaboration. "Collective expansion in high-energy heavy ion collisions". In: *Phys. Rev. Lett.* 78 (1997), pp. 2080–2083. DOI: 10.1103/PhysRevLett.78.2080.
- [29] NA49 collaboration. "Hadron production in nuclear collisions from the NA49 experiment at 158-GeV/c/A". In: *Nucl. Phys. A* 661 (1999). Ed. by L. Riccati, M. Maserà, and E. Vercellin, pp. 45–54. DOI: 10.1016/S0375-9474(99)85007-6.
- [30] WA97 collaboration. "Strangeness enhancement at mid-rapidity in Pb Pb collisions at 158-A-GeV/c". In: *Phys. Lett. B* 449 (1999), pp. 401–406. DOI: 10.1016/S0370-2693(99)00140-9.
- [31] M. Harrison, T. Ludlam, and S. Ozaki. *RHIC project overview*. Mar. 2003. DOI: 10.1016/S0168-9002(02)01937-x. URL: [https://doi.org/10.1016/S0168-9002\(02\)01937-x](https://doi.org/10.1016/S0168-9002(02)01937-x).
- [32] O. S. Brüning et al. *LHC Design Report*. CERN Yellow Reports: Monographs. Geneva: CERN, 2004. DOI: 10.5170/CERN-2004-003-V-1. URL: <https://cds.cern.ch/record/782076>.
- [33] STEPHEN MYERS. "THE LARGE HADRON COLLIDER 2008–2013". In: *International Journal of Modern Physics A* 28.25 (2013), p. 1330035. DOI: 10.1142/S0217751X13300354.
- [34] "LEP Design Report: Vol.2. The LEP Main Ring". In: (June 1984). CERN-LEP-84-01.
- [35] ALICE collaboration. "Centrality determination of Pb-Pb collisions at  $\sqrt{s_{NN}} = 2.76$  TeV with ALICE". In: *Phys.Rev.* C88.4 (2013), p. 044909. DOI: 10.1103/PhysRevC.88.044909. arXiv: 1301.4361 [nucl-ex].
- [36] ATLAS collaboration. "Measurement of the pseudorapidity and transverse momentum dependence of the elliptic flow of charged particles in lead-lead collisions at  $\sqrt{s_{NN}} = 2.76$  TeV with the ATLAS detector". In: *Phys. Lett. B* 707 (2012), pp. 330–348. DOI: 10.1016/j.physletb.2011.12.056. arXiv: 1108.6018 [hep-ex].
- [37] CMS collaboration. "Measurement of the pseudorapidity and centrality dependence of the transverse energy density in PbPb collisions at  $\sqrt{s_{NN}} = 2.76$  TeV". In: *Phys. Rev. Lett.* 109 (2012), p. 152303. DOI: 10.1103/PhysRevLett.109.152303. arXiv: 1205.2488 [nucl-ex].
- [38] STAR collaboration. "Inclusive charged hadron elliptic flow in Au + Au collisions at  $\sqrt{s_{NN}} = 7.7 - 39$  GeV". In: *Phys. Rev. C* 86 (2012), p. 054908. DOI: 10.1103/PhysRevC.86.054908. arXiv: 1206.5528 [nucl-ex].
- [39] ALICE collaboration. "The ALICE experiment at the CERN LHC". In: *JINST* 3 (2008), S08002. DOI: 10.1088/1748-0221/3/08/S08002.

- [40] Michael L. Miller et al. “Glauber modeling in high energy nuclear collisions”. In: *Ann. Rev. Nucl. Part. Sci.* 57 (2007), pp. 205–243. DOI: 10.1146/annurev.nucl.57.090506.123020. arXiv: nucl-ex/0701025.
- [41] Roger D. Woods and David S. Saxon. “Diffuse Surface Optical Model for Nucleon-Nuclei Scattering”. In: *Phys. Rev.* 95 (2 July 1954), pp. 577–578. DOI: 10.1103/PhysRev.95.577. URL: <https://link.aps.org/doi/10.1103/PhysRev.95.577>.
- [42] J. Scott Moreland, Jonah E. Bernhard, and Steffen A. Bass. “Alternative ansatz to wounded nucleon and binary collision scaling in high-energy nuclear collisions”. In: *Phys. Rev. C* 92.1 (2015), p. 011901. DOI: 10.1103/PhysRevC.92.011901. arXiv: 1412.4708 [nucl-th].
- [43] Bjoern Schenke, Prithwish Tribedy, and Raju Venugopalan. “Fluctuating Glasma initial conditions and flow in heavy ion collisions”. In: *Phys. Rev. Lett.* 108 (2012), p. 252301. DOI: 10.1103/PhysRevLett.108.252301. arXiv: 1202.6646 [nucl-th].
- [44] K. J. Eskola et al. “Scaling of transverse energies and multiplicities with atomic number and energy in ultrarelativistic nuclear collisions”. In: *Nucl. Phys. B* 570 (2000), pp. 379–389. DOI: 10.1016/S0550-3213(99)00720-8. arXiv: hep-ph/9909456.
- [45] H. Niemi, K. J. Eskola, and R. Paatelainen. “Event-by-event fluctuations in a perturbative QCD + saturation + hydrodynamics model: Determining QCD matter shear viscosity in ultrarelativistic heavy-ion collisions”. In: *Phys. Rev. C* 93.2 (2016), p. 024907. DOI: 10.1103/PhysRevC.93.024907. arXiv: 1505.02677 [hep-ph].
- [46] Jean-Yves Ollitrault. “Anisotropy as a signature of transverse collective flow”. In: *Phys. Rev. D* 46 (1992), pp. 229–245. DOI: 10.1103/PhysRevD.46.229.
- [47] Ulrich Heinz and Raimond Snellings. “Collective flow and viscosity in relativistic heavy-ion collisions”. In: *Ann. Rev. Nucl. Part. Sci.* 63 (2013), pp. 123–151. DOI: 10.1146/annurev-nucl-102212-170540. arXiv: 1301.2826 [nucl-th].
- [48] Francesco Becattini and R. Fries. “The QCD confinement transition: Hadron formation”. In: *Landolt-Bornstein* 23 (2010). Ed. by R. Stock, p. 208. DOI: 10.1007/978-3-642-01539-7\_8. arXiv: 0907.1031 [nucl-th].
- [49] P. Danielewicz and M. Gyulassy. “Dissipative Phenomena in Quark Gluon Plasmas”. In: *Phys. Rev. D* 31 (1985), pp. 53–62. DOI: 10.1103/PhysRevD.31.53.
- [50] P. Kovtun, Dan T. Son, and Andrei O. Starinets. “Viscosity in strongly interacting quantum field theories from black hole physics”. In: *Phys. Rev. Lett.* 94 (2005), p. 111601. DOI: 10.1103/PhysRevLett.94.111601. arXiv: hep-th/0405231.

- [51] Laszlo P. Csernai, Joseph. I. Kapusta, and Larry D. McLerran. “On the Strongly-Interacting Low-Viscosity Matter Created in Relativistic Nuclear Collisions”. In: *Phys. Rev. Lett.* 97 (2006), p. 152303. DOI: 10.1103/PhysRevLett.97.152303. arXiv: nucl-th/0604032.
- [52] Bjorn Schenke, Sangyong Jeon, and Charles Gale. “Higher flow harmonics from (3+1)D event-by-event viscous hydrodynamics”. In: *Phys. Rev. C* 85 (2012), p. 024901. DOI: 10.1103/PhysRevC.85.024901. arXiv: 1109.6289 [hep-ph].
- [53] PHENIX collaboration. “Measurements of Higher-Order Flow Harmonics in Au+Au Collisions at  $\sqrt{s_{NN}} = 200$  GeV”. In: *Phys. Rev. Lett.* 107 (2011), p. 252301. DOI: 10.1103/PhysRevLett.107.252301. arXiv: 1105.3928 [nucl-ex].
- [54] ALICE collaboration. “Production of charged pions, kaons, and (anti-)protons in Pb-Pb and inelastic  $pp$  collisions at  $\sqrt{s_{NN}} = 5.02$  TeV”. In: *Phys. Rev. C* 101.4 (2020), p. 044907. DOI: 10.1103/PhysRevC.101.044907. arXiv: 1910.07678 [nucl-ex].
- [55] ALICE collaboration. “ $K^*(892)^0$  and  $\phi(1020)$  meson production at high transverse momentum in  $pp$  and Pb-Pb collisions at  $\sqrt{s_{NN}} = 2.76$  TeV”. In: *Phys. Rev. C* 95.6 (2017), p. 064606. DOI: 10.1103/PhysRevC.95.064606. arXiv: 1702.00555 [nucl-ex].
- [56] ALICE collaboration. “Production of  $K^*(892)^0$  and  $\phi(1020)$  in  $pp$  and Pb-Pb collisions at  $\sqrt{s_{NN}} = 5.02$  TeV”. In: *Phys. Rev. C* 106.3 (2022), p. 034907. DOI: 10.1103/PhysRevC.106.034907. arXiv: 2106.13113 [nucl-ex].
- [57] CMS collaboration. “The production of isolated photons in PbPb and  $pp$  collisions at  $\sqrt{s_{NN}} = 5.02$  TeV”. In: *JHEP* 07 (2020), p. 116. DOI: 10.1007/JHEP07(2020)116. arXiv: 2003.12797 [hep-ex].
- [58] ALICE collaboration. “Measurement of charged jet suppression in Pb-Pb collisions at  $\sqrt{s_{NN}} = 2.76$  TeV”. In: *JHEP* 1403 (2014), p. 013. DOI: 10.1007/JHEP03(2014)013. arXiv: 1311.0633 [nucl-ex].
- [59] J. D. Bjorken. “Energy Loss of Energetic Partons in Quark - Gluon Plasma: Possible Extinction of High  $p(t)$  Jets in Hadron - Hadron Collisions”. In: (Aug. 1982). FERMILAB-PUB-82-059-THY, FERMILAB-PUB-82-059-T.
- [60] V. V. Lebedev and Andrei V. Smilga. “On anomalous damping in quark - gluon plasma”. In: *Phys. Lett. B* 253 (1991), pp. 231–236. DOI: 10.1016/0370-2693(91)91389-D.
- [61] V. V. Lebedev and Andrei V. Smilga. “Anomalous damping in plasma”. In: *Physica A* 181 (1992), pp. 187–220.
- [62] Markus H. Thoma and Miklos Gyulassy. “Quark Damping and Energy Loss in the High Temperature QCD”. In: *Nucl. Phys. B* 351 (1991), pp. 491–506. DOI: 10.1016/S0550-3213(05)80031-8.

- [63] Eric Braaten and Markus H. Thoma. “Energy loss of a heavy fermion in a hot plasma”. In: *Phys. Rev. D* 44 (1991), pp. 1298–1310. DOI: 10.1103/PhysRevD.44.1298.
- [64] C. P. Burgess and A. L. Marini. “The Damping of energetic gluons and quarks in high temperature QCD”. In: *Phys. Rev. D* 45 (1992), pp. 17–20. DOI: 10.1103/PhysRevD.45.R17. arXiv: hep-th/9109051.
- [65] T. Altherr, E. Petitgirard, and T. del Rio Gaztelurrutia. “Damping rate of a moving fermion”. In: *Phys. Rev. D* 47 (1993), pp. 703–710. DOI: 10.1103/PhysRevD.47.703.
- [66] David d’Enterria. “Jet quenching”. In: *Landolt-Bornstein* 23 (2010), p. 471. DOI: 10.1007/978-3-642-01539-7\_16. arXiv: 0902.2011 [nucl-ex].
- [67] Guang-You Qin and Berndt Muller. “Explanation of Di-jet asymmetry in Pb+Pb collisions at the Large Hadron Collider”. In: *Phys. Rev. Lett.* 106 (2011). [Erratum: *Phys.Rev.Lett.* 108, 189904 (2012)], p. 162302. DOI: 10.1103/PhysRevLett.106.162302. arXiv: 1012.5280 [hep-ph].
- [68] Jorge Casalderrey-Solana et al. “Angular Structure of Jet Quenching Within a Hybrid Strong/Weak Coupling Model”. In: *JHEP* 03 (2017), p. 135. DOI: 10.1007/JHEP03(2017)135. arXiv: 1609.05842 [hep-ph].
- [69] R. B. Neufeld and Ivan Vitev. “Parton showers as sources of energy-momentum deposition in the QGP and their implication for shockwave formation at RHIC and at the LHC”. In: *Phys. Rev. C* 86 (2012), p. 024905. DOI: 10.1103/PhysRevC.86.024905. arXiv: 1105.2067 [hep-ph].
- [70] ALICE collaboration. “Transverse momentum spectra and nuclear modification factors of charged particles in pp, p-Pb and Pb-Pb collisions at the LHC”. In: *JHEP* 11 (2018), p. 013. DOI: 10.1007/JHEP11(2018)013. arXiv: 1802.09145 [nucl-ex].
- [71] CMS collaboration. “Nuclear Effects on the Transverse Momentum Spectra of Charged Particles in pPb Collisions at  $\sqrt{s_{NN}} = 5.02$  TeV”. In: *Eur. Phys. J. C* 75.5 (2015), p. 237. DOI: 10.1140/epjc/s10052-015-3435-4. arXiv: 1502.05387 [nucl-ex].
- [72] CMS collaboration. “Charged-particle nuclear modification factors in PbPb and pPb collisions at  $\sqrt{s_{NN}} = 5.02$  TeV”. In: *JHEP* 04 (2017), p. 039. DOI: 10.1007/JHEP04(2017)039. arXiv: 1611.01664 [nucl-ex].
- [73] PHENIX collaboration. “Jet properties from dihadron correlations in  $p^+p$  collisions at  $\sqrt{s} = 200$ -GeV”. In: *Phys. Rev. D* 74 (2006), p. 072002. DOI: 10.1103/PhysRevD.74.072002. arXiv: hep-ex/0605039.
- [74] CERN-Columbia-Oxford-Rockefeller, CCOR collaboration. “A Measurement of the Transverse Momenta of Partons, and of Jet Fragmentation as a Function of  $\sqrt{s}$  in  $pp$  Collisions”. In: *Phys. Lett. B* 97 (1980), pp. 163–168. DOI: 10.1016/0370-2693(80)90572-9.

- [75] M. H. Thoma. “Damping rate of a hard photon in a relativistic plasma”. In: *Phys. Rev. D* 51 (1995), pp. 862–865. DOI: 10.1103/PhysRevD.51.862. arXiv: hep-ph/9405309 [hep-ph].
- [76] ALICE collaboration. “First measurement of coherent  $\rho^0$  photoproduction in ultra-peripheral Xe–Xe collisions at  $\sqrt{s_{NN}}=5.44$  TeV”. In: *Phys. Lett. B* 820 (2021), p. 136481. DOI: 10.1016/j.physletb.2021.136481. arXiv: 2101.02581 [nucl-ex].
- [77] ALICE collaboration. “Production of pions, kaons, (anti-)protons and  $\phi$  mesons in Xe–Xe collisions at  $\sqrt{s_{NN}} = 5.44$  TeV”. In: *Eur. Phys. J. C* 81.7 (2021), p. 584. DOI: 10.1140/epjc/s10052-021-09304-4. arXiv: 2101.03100 [nucl-ex].
- [78] ALICE collaboration. “Inclusive heavy-flavour production at central and forward rapidity in Xe–Xe collisions at  $\sqrt{s_{NN}}=5.44$  TeV”. In: *Phys. Lett. B* 819 (2021), p. 136437. DOI: 10.1016/j.physletb.2021.136437. arXiv: 2011.06970 [nucl-ex].
- [79] ALICE collaboration. “Inclusive  $J/\psi$  production in Xe–Xe collisions at  $\sqrt{s_{NN}} = 5.44$  TeV”. In: *Phys. Lett. B* 785 (2018), pp. 419–428. DOI: 10.1016/j.physletb.2018.08.047. arXiv: 1805.04383 [nucl-ex].
- [80] ALICE collaboration. “Anisotropic flow in Xe–Xe collisions at  $\sqrt{s_{NN}} = 5.44$  TeV”. In: *Phys. Lett. B* 784 (2018), pp. 82–95. DOI: 10.1016/j.physletb.2018.06.059. arXiv: 1805.01832 [nucl-ex].
- [81] ALICE collaboration. “Transverse momentum spectra and nuclear modification factors of charged particles in Xe–Xe collisions at  $\sqrt{s_{NN}} = 5.44$  TeV”. In: *Phys. Lett. B* 788 (2019), pp. 166–179. DOI: 10.1016/j.physletb.2018.10.052. arXiv: 1805.04399 [nucl-ex].
- [82] ALICE collaboration. “Centrality and pseudorapidity dependence of the charged-particle multiplicity density in Xe–Xe collisions at  $\sqrt{s_{NN}} = 5.44$  TeV”. In: *Phys. Lett. B* 790 (2019), pp. 35–48. DOI: 10.1016/j.physletb.2018.12.048. arXiv: 1805.04432 [nucl-ex].
- [83] ALICE collaboration. “Anisotropic flow of identified hadrons in Xe–Xe collisions at  $\sqrt{s_{NN}} = 5.44$  TeV”. In: *JHEP* 10 (2021), p. 152. DOI: 10.1007/JHEP10(2021)152. arXiv: 2107.10592 [nucl-ex].
- [84] ALICE collaboration. “Long-range angular correlations on the near and away side in  $p$ -Pb collisions at  $\sqrt{s_{NN}} = 5.02$  TeV”. In: *Phys. Lett. B* 719 (2013), pp. 29–41. DOI: 10.1016/j.physletb.2013.01.012. arXiv: 1212.2001 [nucl-ex].
- [85] CMS collaboration. “Observation of Long-Range Near-Side Angular Correlations in Proton–Proton Collisions at the LHC”. In: *JHEP* 09 (2010), p. 091. DOI: 10.1007/JHEP09(2010)091. arXiv: 1009.4122 [hep-ex].

- [86] ATLAS collaboration. “Observation of Long-Range Elliptic Azimuthal Anisotropies in  $\sqrt{s} = 13$  and 2.76 TeV  $pp$  Collisions with the ATLAS Detector”. In: *Phys. Rev. Lett.* 116.17 (2016), p. 172301. DOI: 10.1103/PhysRevLett.116.172301. arXiv: 1509.04776 [hep-ex].
- [87] K. Kovarik et al. “nCTEQ15 - Global analysis of nuclear parton distributions with uncertainties in the CTEQ framework”. In: *Phys. Rev. D* 93.8 (2016), p. 085037. DOI: 10.1103/PhysRevD.93.085037. arXiv: 1509.00792 [hep-ph].
- [88] Rabah Abdul Khalek et al. “nNNPDF2.0: quark flavor separation in nuclei from LHC data”. In: *JHEP* 09 (2020), p. 183. DOI: 10.1007/JHEP09(2020)183. arXiv: 2006.14629 [hep-ph].
- [89] Larry D. McLerran. “The Color glass condensate and small  $x$  physics: Four lectures”. In: *Lect. Notes Phys.* 583 (2002). Ed. by Willibald Plessas and L. Mathelitsch, pp. 291–334. DOI: 10.1007/3-540-45792-5\_8. arXiv: hep-ph/0104285.
- [90] Alberto Accardi et al. “Hard probes in heavy ion collisions at the lhc: pdfs, shadowing and pa collisions”. In: *3rd Workshop on Hard Probes in Heavy Ion Collisions: 3rd Plenary Meeting*. Oct. 2004. arXiv: hep-ph/0308248.
- [91] “Charged-hadron production in  $pp$ ,  $p+Pb$ ,  $Pb+Pb$ , and  $Xe+Xe$  collisions at  $\sqrt{s_{NN}} = 5$  TeV with the ATLAS detector at the LHC”. In: (Nov. 2022). arXiv: 2211.15257 [hep-ex].
- [92] CMS collaboration. “Search for Resonances in the Dijet Mass Spectrum from 7 TeV  $pp$  Collisions at CMS”. In: *Phys. Lett. B* 704 (2011), pp. 123–142. DOI: 10.1016/j.physletb.2011.09.015. arXiv: 1107.4771 [hep-ex].
- [93] ATLAS collaboration. “Search for New Physics in Dijet Mass and Angular Distributions in  $pp$  Collisions at  $\sqrt{s} = 7$  TeV Measured with the ATLAS Detector”. In: *New J. Phys.* 13 (2011), p. 053044. DOI: 10.1088/1367-2630/13/5/053044. arXiv: 1103.3864 [hep-ex].
- [94] ATLAS collaboration. “Observation of a Centrality-Dependent Dijet Asymmetry in Lead-Lead Collisions at  $\sqrt{s_{NN}} = 2.77$  TeV with the ATLAS Detector at the LHC”. In: *Phys. Rev. Lett.* 105 (2010), p. 252303. DOI: 10.1103/PhysRevLett.105.252303. arXiv: 1011.6182 [hep-ex].
- [95] CMS collaboration. “Studies of dijet transverse momentum balance and pseudorapidity distributions in  $pPb$  collisions at  $\sqrt{s_{NN}} = 5.02$  TeV”. In: *Eur. Phys. J. C* 74.7 (2014), p. 2951. DOI: 10.1140/epjc/s10052-014-2951-y. arXiv: 1401.4433 [nucl-ex].
- [96] ATLAS collaboration. “Measurements of the suppression and correlations of dijets in  $Pb+Pb$  collisions at  $s_{NN}=5.02$  TeV”. In: *Phys. Rev. C* 107.5 (2023), p. 054908. DOI: 10.1103/PhysRevC.107.054908. arXiv: 2205.00682 [nucl-ex].
- [97] Thorsten Renk and K. Eskola. “Prospects of medium tomography using back-to-back hadron correlations”. In: *Phys. Rev. C* 75 (2007), p. 054910. DOI: 10.1103/PhysRevC.75.054910. arXiv: hep-ph/0610059 [hep-ph].

- [98] STAR collaboration. “Evidence from d + Au measurements for final state suppression of high p(T) hadrons in Au+Au collisions at RHIC”. In: *Phys. Rev. Lett.* 91 (2003), p. 072304. DOI: 10.1103/PhysRevLett.91.072304. arXiv: nucl-ex/0306024 [nucl-ex].
- [99] B.R. Martin and G. Shaw. *Particle Physics*. Manchester Physics Series. Wiley, 1998. ISBN: 9780471972853. URL: <https://books.google.fi/books?id=T4fDQgAACAAJ>.
- [100] Christian Bierlich et al. “A comprehensive guide to the physics and usage of PYTHIA 8.3”. In: *SciPost Phys. Codebases* (2022), p. 8. DOI: 10.21468/SciPostPhysCodeb.8. arXiv: 2203.11601 [hep-ph].
- [101] ALICE collaboration. “Measurement of inelastic, single- and double-diffraction cross sections in proton–proton collisions at the LHC with ALICE”. In: *Eur. Phys. J. C* 73.6 (2013), p. 2456. DOI: 10.1140/epjc/s10052-013-2456-0. arXiv: 1208.4968 [hep-ex].
- [102] Torbjorn Sjostrand, Stephen Mrenna, and Peter Z. Skands. “PYTHIA 6.4 Physics and Manual”. In: *JHEP* 05 (2006), p. 026. DOI: 10.1088/1126-6708/2006/05/026. arXiv: hep-ph/0603175.
- [103] R. Engel, J. Ranft, and S. Roesler. “Hard diffraction in hadron-hadron interactions and in photoproduction”. In: *Phys. Rev. D* 52 (3 Aug. 1995), pp. 1459–1468. DOI: 10.1103/PhysRevD.52.1459. URL: <https://link.aps.org/doi/10.1103/PhysRevD.52.1459>.
- [104] Tie-Jiun Hou et al. “New CTEQ global analysis of quantum chromodynamics with high-precision data from the LHC”. In: *Phys. Rev. D* 103.1 (2021), p. 014013. DOI: 10.1103/PhysRevD.103.014013. arXiv: 1912.10053 [hep-ph].
- [105] Guang-You Qin and Xin-Nian Wang. “Jet quenching in high-energy heavy-ion collisions”. In: *Int. J. Mod. Phys. E* 24.11 (2015). Ed. by Xin-Nian Wang, p. 1530014. DOI: 10.1142/S0218301315300143. arXiv: 1511.00790 [hep-ph].
- [106] J. F. Owens, E. Reya, and M. Gluck. “Detailed Quantum Chromodynamic Predictions for High p(T) Processes”. In: *Phys. Rev. D* 18 (1978), p. 1501. DOI: 10.1103/PhysRevD.18.1501.
- [107] H1, ZEUS collaboration. “Combination of measurements of inclusive deep inelastic  $e^\pm p$  scattering cross sections and QCD analysis of HERA data”. In: *Eur. Phys. J. C* 75.12 (2015), p. 580. DOI: 10.1140/epjc/s10052-015-3710-4. arXiv: 1506.06042 [hep-ex].
- [108] NNPDF collaboration. “Parton distributions from high-precision collider data”. In: *Eur. Phys. J. C* 77.10 (2017), p. 663. DOI: 10.1140/epjc/s10052-017-5199-5. arXiv: 1706.00428 [hep-ph].
- [109] Jon Butterworth et al. “PDF4LHC recommendations for LHC Run II”. In: *J. Phys. G* 43 (2016), p. 023001. DOI: 10.1088/0954-3899/43/2/023001. arXiv: 1510.03865 [hep-ph].

- [110] ZEUS, H1 collaboration. “PDF Fits at HERA”. In: *PoS EPS-HEP2011* (2011), p. 320. DOI: 10.22323/1.134.0320. arXiv: 1112.2107 [hep-ph].
- [111] Bernd A. Kniehl, G. Kramer, and B. Potter. “Fragmentation functions for pions, kaons, and protons at next-to-leading order”. In: *Nucl. Phys. B* 582 (2000), pp. 514–536. DOI: 10.1016/S0550-3213(00)00303-5. arXiv: hep-ph/0010289.
- [112] J. Binnewies, Bernd A. Kniehl, and G. Kramer. “Pion and kaon production in  $e^+e^-$  and  $e^+p$  collisions at next-to-leading order”. In: *Phys. Rev. D* 52 (1995), pp. 4947–4960. DOI: 10.1103/PhysRevD.52.4947. arXiv: hep-ph/9503464.
- [113] ATLAS collaboration. “Measurement of the jet fragmentation function and transverse profile in proton-proton collisions at a center-of-mass energy of 7 TeV with the ATLAS detector”. In: *Eur. Phys. J. C* 71 (2011), p. 1795. DOI: 10.1140/epjc/s10052-011-1795-y. arXiv: 1109.5816 [hep-ex].
- [114] K. J. Eskola et al. “The Fragility of high-p(T) hadron spectra as a hard probe”. In: *Nucl. Phys. A* 747 (2005), pp. 511–529. DOI: 10.1016/j.nuclphysa.2004.09.070. arXiv: hep-ph/0406319.
- [115] Alberto Accardi. “Space-time evolution of hadronization”. In: *Eur. Phys. J. C* 49 (2007). Ed. by F. Antinori et al., pp. 347–353. DOI: 10.1140/epjc/s10052-006-0055-z. arXiv: nucl-th/0609010.
- [116] R. Baier. “Jet quenching”. In: *Nucl. Phys. A* 715 (2003). Ed. by H. Gutbrod, J. Aichelin, and K. Werner, pp. 209–218. DOI: 10.1016/S0375-9474(02)01429-X. arXiv: hep-ph/0209038.
- [117] Miklos Gyulassy and Michael Plumer. “Jet Quenching in Dense Matter”. In: *Phys. Lett. B* 243 (1990), pp. 432–438. DOI: 10.1016/0370-2693(90)91409-5.
- [118] M. Harrison, T. Ludlam, and S. Ozaki. “RHIC project overview”. In: *Nucl. Instrum. Meth. A* 499 (2003), pp. 235–244. DOI: 10.1016/S0168-9002(02)01937-X.
- [119] PHENIX collaboration. “Study of  $\phi$ -meson production in  $p+Al$ ,  $p+Au$ ,  $d+Au$ , and  $^3He+Au$  collisions at  $\sqrt{s_{NN}} = 200$  GeV”. In: *Phys. Rev. C* 106.1 (2022), p. 014908. DOI: 10.1103/PhysRevC.106.014908. arXiv: 2203.06087 [nucl-ex].
- [120] H. Hahn et al. “The RHIC design overview”. In: *Nucl. Instrum. Meth. A* 499 (2003), pp. 245–263. DOI: 10.1016/S0168-9002(02)01938-1.
- [121] BRAHMS collaboration. “The BRAHMS experiment at RHIC”. In: *Nucl. Instrum. Meth. A* 499 (2003), pp. 437–468. DOI: 10.1016/S0168-9002(02)01949-6.
- [122] PHENIX collaboration. “PHENIX detector overview”. In: *Nucl. Instrum. Meth. A* 499 (2003), pp. 469–479. DOI: 10.1016/S0168-9002(02)01950-2.



- [123] PHOBOS collaboration. "The PHOBOS detector at RHIC". In: *Nucl. Instrum. Meth. A* 499 (2003), pp. 603–623. DOI: 10.1016/S0168-9002(02)01959-9.
- [124] STAR collaboration. "STAR detector overview". In: *Nucl. Instrum. Meth. A* 499 (2003), pp. 624–632. DOI: 10.1016/S0168-9002(02)01960-5.
- [125] PHENIX collaboration. "Formation of dense partonic matter in relativistic nucleus-nucleus collisions at RHIC: Experimental evaluation by the PHENIX collaboration". In: *Nucl. Phys. A* 757 (2005), pp. 184–283. DOI: 10.1016/j.nuclphysa.2005.03.086. arXiv: nucl-ex/0410003.
- [126] BRAHMS collaboration. "Quark gluon plasma and color glass condensate at RHIC? The Perspective from the BRAHMS experiment". In: *Nucl. Phys. A* 757 (2005), pp. 1–27. DOI: 10.1016/j.nuclphysa.2005.02.130. arXiv: nucl-ex/0410020.
- [127] PHOBOS collaboration. "The PHOBOS perspective on discoveries at RHIC". In: *Nucl. Phys. A* 757 (2005), pp. 28–101. DOI: 10.1016/j.nuclphysa.2005.03.084. arXiv: nucl-ex/0410022.
- [128] STAR collaboration. "Experimental and theoretical challenges in the search for the quark gluon plasma: The STAR Collaboration's critical assessment of the evidence from RHIC collisions". In: *Nucl. Phys. A* 757 (2005), pp. 102–183. DOI: 10.1016/j.nuclphysa.2005.03.085. arXiv: nucl-ex/0501009.
- [129] STAR collaboration. "STAR upgrade program and future physics". In: *J. Phys. Conf. Ser.* 535 (2014), p. 012022. DOI: 10.1088/1742-6596/535/1/012022.
- [130] C. Aidala et al. "sPHENIX: An Upgrade Concept from the PHENIX Collaboration". In: (July 2012). arXiv: 1207.6378 [nucl-ex].
- [131] Jürgen Schukraft. "A dedicated heavy ion experiment at the LHC: Expression of interest". In: (1992). Conference : Towards the LHC experimental programme : General Meeting on LHC Physics and Detectors, Evian-les-Bains, France, 5 - 8 Mar 1992. URL: <https://cds.cern.ch/record/247463>.
- [132] ATLAS collaboration. "The ATLAS Experiment at the CERN Large Hadron Collider". In: *JINST* 3 (2008), S08003. DOI: 10.1088/1748-0221/3/08/S08003.
- [133] CMS collaboration. "The CMS Experiment at the CERN LHC". In: *JINST* 3 (2008), S08004. DOI: 10.1088/1748-0221/3/08/S08004.
- [134] LHCb collaboration. "The LHCb Detector at the LHC". In: *JINST* 3 (2008), S08005. DOI: 10.1088/1748-0221/3/08/S08005.
- [135] Arpad Horvath. Free to use under CC BY-SA 2.5 license. URL: [https://commons.wikimedia.org/wiki/Large\\_Hadron\\_Collider#/media/File:LHC.svg](https://commons.wikimedia.org/wiki/Large_Hadron_Collider#/media/File:LHC.svg).

- [136] ATLAS collaboration. “Centrality and rapidity dependence of inclusive jet production in  $\sqrt{s_{NN}} = 5.02$  TeV proton-lead collisions with the ATLAS detector”. In: *Phys. Lett. B* 748 (2015), pp. 392–413. DOI: 10.1016/j.physletb.2015.07.023. arXiv: 1412.4092 [hep-ex].
- [137] Zi-Wei Lin and Liang Zheng. “Further developments of a multi-phase transport model for relativistic nuclear collisions”. In: *Nucl. Sci. Tech.* 32.10 (2021), p. 113. DOI: 10.1007/s41365-021-00944-5. arXiv: 2110.02989 [nucl-th].
- [138] Stefano Frixione, Paolo Nason, and Carlo Oleari. “Matching NLO QCD computations with Parton Shower simulations: the POWHEG method”. In: *JHEP* 11 (2007), p. 070. DOI: 10.1088/1126-6708/2007/11/070. arXiv: 0709.2092 [hep-ph].
- [139] Simone Alioli et al. “A general framework for implementing NLO calculations in shower Monte Carlo programs: the POWHEG BOX”. In: *JHEP* 06 (2010), p. 043. DOI: 10.1007/JHEP06(2010)043. arXiv: 1002.2581 [hep-ph].
- [140] Korinna C. Zapp. “JEWEL 2.0.0: directions for use”. In: *Eur. Phys. J. C* 74.2 (2014), p. 2762. DOI: 10.1140/epjc/s10052-014-2762-1. arXiv: 1311.0048 [hep-ph].
- [141] Bo Andersson, G. Gustafson, and B. Soderberg. “A General Model for Jet Fragmentation”. In: *Z. Phys. C* 20 (1983), p. 317. DOI: 10.1007/BF01407824.
- [142] Torbjörn Sjöstrand. “Jet fragmentation of multiparton configurations in a string framework”. In: *Nuclear Physics B* 248.2 (1984), pp. 469–502. ISSN: 0550-3213. DOI: 10.1016/0550-3213(84)90607-2. URL: <https://www.sciencedirect.com/science/article/pii/0550321384906072>.
- [143] Antonio Ortiz Velasquez et al. “Color Reconnection and Flowlike Patterns in  $pp$  Collisions”. In: *Phys. Rev. Lett.* 111.4 (2013), p. 042001. DOI: 10.1103/PhysRevLett.111.042001. arXiv: 1303.6326 [hep-ph].
- [144] Christian Bierlich and Jesper Roy Christiansen. “Effects of color reconnection on hadron flavor observables”. In: *Phys. Rev. D* 92.9 (2015), p. 094010. DOI: 10.1103/PhysRevD.92.094010. arXiv: 1507.02091 [hep-ph].
- [145] Torbjörn Sjöstrand and Marius Uthm. “A Framework for Hadronic Rescattering in  $pp$  Collisions”. In: *Eur. Phys. J. C* 80.10 (2020), p. 907. DOI: 10.1140/epjc/s10052-020-8399-3. arXiv: 2005.05658 [hep-ph].
- [146] Peter Skands, Stefano Carrazza, and Juan Rojo. “Tuning PYTHIA 8.1: the Monash 2013 Tune”. In: *Eur. Phys. J. C* 74.8 (2014), p. 3024. DOI: 10.1140/epjc/s10052-014-3024-y. arXiv: 1404.5630 [hep-ph].
- [147] Zi-Wei Lin et al. “A Multi-phase transport model for relativistic heavy ion collisions”. In: *Phys. Rev. C* 72 (2005), p. 064901. DOI: 10.1103/PhysRevC.72.064901. arXiv: nucl-th/0411110.
- [148] Xin-Nian Wang and Miklos Gyulassy. “HIJING: A Monte Carlo model for multiple jet production in  $pp$ ,  $pA$  and  $AA$  collisions”. In: *Phys. Rev. D* 44 (1991), pp. 3501–3516. DOI: 10.1103/PhysRevD.44.3501.

- [149] Miklos Gyulassy and Xin-Nian Wang. “HIJING 1.0: A Monte Carlo program for parton and particle production in high-energy hadronic and nuclear collisions”. In: *Comput. Phys. Commun.* 83 (1994), p. 307. DOI: 10.1016/0010-4655(94)90057-4. arXiv: nucl-th/9502021.
- [150] Bin Zhang. “ZPC 1.0.1: A Parton cascade for ultrarelativistic heavy ion collisions”. In: *Comput. Phys. Commun.* 109 (1998), pp. 193–206. DOI: 10.1016/S0010-4655(98)00010-1. arXiv: nucl-th/9709009.
- [151] Yuncun He and Zi-Wei Lin. “Improved Quark Coalescence for a Multi-Phase Transport Model”. In: *Phys. Rev. C* 96.1 (2017), p. 014910. DOI: 10.1103/PhysRevC.96.014910. arXiv: 1703.02673 [nucl-th].
- [152] Zi-wei Lin and C. M. Ko. “Partonic effects on the elliptic flow at RHIC”. In: *Phys. Rev. C* 65 (2002), p. 034904. DOI: 10.1103/PhysRevC.65.034904. arXiv: nucl-th/0108039.
- [153] René Brun et al. “GEANT Detector Description and Simulation Tool”. In: (1994). DOI: 10.17181/CERN.MUHF.DMJ1.
- [154] GEANT4 collaboration. “GEANT4—a simulation toolkit”. In: *Nucl. Instrum. Meth. A* 506 (2003), pp. 250–303. DOI: 10.1016/S0168-9002(03)01368-8.
- [155] “Stopping powers and ranges for protons and alpha particles”. In: (May 1993). URL: <https://www.osti.gov/biblio/139791>.
- [156] Donald E. Groom, Nikolai V. Mokhov, and Sergei I. Striganov. “Muon stopping power and range tables 10-MeV to 100-TeV”. In: *Atom. Data Nucl. Data Tabl.* 78 (2001), pp. 183–356. DOI: 10.1006/adnd.2001.0861.
- [157] ALICE collaboration. “Definition of the ALICE Coordinate System and Basic Rules for Sub-detector Components Numbering”. In: (2003). URL: [https://alice-servotech.web.cern.ch/HELP\\_DCDB-SVT/Help\\_Files/ALICE-INT-2003-038.pdf](https://alice-servotech.web.cern.ch/HELP_DCDB-SVT/Help_Files/ALICE-INT-2003-038.pdf).
- [158] J. Alme et al. “The ALICE TPC, a large 3-dimensional tracking device with fast readout for ultra-high multiplicity events”. In: *Nucl. Instrum. Meth. A* 622 (2010), pp. 316–367. DOI: 10.1016/j.nima.2010.04.042. arXiv: 1001.1950 [physics.ins-det].
- [159] ALICE collaboration. *ALICE time projection chamber: Technical Design Report*. Technical design report. ALICE. Geneva: CERN, 2000. URL: <https://cds.cern.ch/record/451098>.
- [160] “ALICE upgrades during the LHC Long Shutdown 2”. In: (Feb. 2023). arXiv: 2302.01238 [physics.ins-det].
- [161] ALICE collaboration. “Charmonium and  $e^+e^-$  pair photoproduction at mid-rapidity in ultra-peripheral Pb-Pb collisions at  $\sqrt{s_{NN}}=2.76$  TeV”. In: *Eur. Phys. J. C* 73.11 (2013), p. 2617. DOI: 10.1140/epjc/s10052-013-2617-1. arXiv: 1305.1467 [nucl-ex].
- [162] ALICE collaboration. “Coherent  $J/\psi$  photoproduction in ultra-peripheral Pb-Pb collisions at  $\sqrt{s_{NN}} = 2.76$  TeV”. In: *Phys. Lett. B* 718 (2013), pp. 1273–1283. DOI: 10.1016/j.physletb.2012.11.059. arXiv: 1209.3715 [nucl-ex].

- [163] ALICE collaboration. “Coherent  $J/\psi$  photoproduction at forward rapidity in ultra-peripheral Pb-Pb collisions at  $\sqrt{s_{NN}} = 5.02$  TeV”. In: *Phys. Lett. B* 798 (2019), p. 134926. DOI: 10.1016/j.physletb.2019.134926. arXiv: 1904.06272 [nucl-ex].
- [164] ALICE collaboration. “Coherent  $J/\psi$  and  $\psi'$  photoproduction at midrapidity in ultra-peripheral Pb-Pb collisions at  $\sqrt{s_{NN}} = 5.02$  TeV”. In: *Eur. Phys. J. C* 81.8 (2021), p. 712. DOI: 10.1140/epjc/s10052-021-09437-6. arXiv: 2101.04577 [nucl-ex].
- [165] ALICE collaboration. “First measurement of the  $|t|$ -dependence of coherent  $J/\psi$  photonuclear production”. In: *Phys. Lett. B* 817 (2021), p. 136280. DOI: 10.1016/j.physletb.2021.136280. arXiv: 2101.04623 [nucl-ex].
- [166] ALICE collaboration. “Exclusive  $J/\psi$  photoproduction off protons in ultra-peripheral p-Pb collisions at  $\sqrt{s_{NN}} = 5.02$  TeV”. In: *Phys. Rev. Lett.* 113.23 (2014), p. 232504. DOI: 10.1103/PhysRevLett.113.232504. arXiv: 1406.7819 [nucl-ex].
- [167] ALICE collaboration. “Energy dependence of exclusive  $J/\psi$  photoproduction off protons in ultra-peripheral p-Pb collisions at  $\sqrt{s_{NN}} = 5.02$  TeV”. In: *Eur. Phys. J. C* 79.5 (2019), p. 402. DOI: 10.1140/epjc/s10052-019-6816-2. arXiv: 1809.03235 [nucl-ex].
- [168] J Allen et al. *ALICE DCal: An Addendum to the EMCal Technical Design Report Di-Jet and Hadron-Jet correlation measurements in ALICE*. Tech. rep. CERN-LHCC-2010-011, ALICE-TDR-14-add-1. 2010. URL: <https://cds.cern.ch/record/1272952>.
- [169] ALICE collaboration. “New ALICE detectors for Run 3 and 4 at the CERN LHC”. In: *Nucl. Instrum. Meth. A* 958 (2020). Ed. by Manfred Krammer et al., p. 162116. DOI: 10.1016/j.nima.2019.04.070.
- [170] F. Sauli. “GEM: A new concept for electron amplification in gas detectors”. In: *Nuclear Instruments and Methods in Physics Research Section A: Accelerators, Spectrometers, Detectors and Associated Equipment* 386.2 (1997), pp. 531–534. ISSN: 0168-9002. DOI: 10.1016/S0168-9002(96)01172-2. URL: <https://www.sciencedirect.com/science/article/pii/S0168900296011722>.
- [171] ALICE TPC collaboration. “The upgrade of the ALICE TPC with GEMs and continuous readout”. In: *JINST* 16.03 (2021), P03022. DOI: 10.1088/1748-0221/16/03/P03022. arXiv: 2012.09518 [physics.ins-det].
- [172] ALICE TPC collaboration. “Ion backflow studies for the ALICE TPC upgrade with GEMs”. In: *JINST* 9 (2014), p. C04025. DOI: 10.1088/1748-0221/9/04/C04025.
- [173] ALICE collaboration. “Technical Design Report for the Upgrade of the ALICE Inner Tracking System”. In: *J. Phys. G* 41 (2014), p. 087002. DOI: 10.1088/0954-3899/41/8/087002.

- [174] *Technical Design Report for the Muon Forward Tracker*. Tech. rep. CERN-LHCC-2015-001, ALICE-TDR-018. 2015. URL: <https://cds.cern.ch/record/1981898>.
- [175] M. Slupecki. “The Fast Interaction Trigger for the ALICE Upgrade”. PhD thesis. University of Jyväskylä, 2020. ISBN: 978-951-39-8186-0.
- [176] “Upgrade of the ALICE Readout & Trigger System”. In: (2013). Ed. by P. Antonioli, A. Kluge, and W. Riegler. CERN-LHCC-2013-019, ALICE-TDR-015.
- [177] ALICE collaboration. “New Fast Interaction Trigger for ALICE”. In: *Nucl. Instrum. Meth.* A845 (2017), pp. 463–466. DOI: 10.1016/j.nima.2016.06.029.
- [178] ALICE collaboration. “The Forward Diffractive Detector for ALICE”. In: *PoS LHCP2020* (2021). Ed. by Bruno Mansoulie et al., p. 221. DOI: 10.22323/1.382.0221.
- [179] ALICE collaboration. “Azimuthal anisotropy of charged jet production in  $\sqrt{s_{NN}} = 2.76$  TeV Pb-Pb collisions”. In: *Phys. Lett. B* 753 (2016), pp. 511–525. DOI: 10.1016/j.physletb.2015.12.047. arXiv: 1509.07334 [nucl-ex].
- [180] ALICE collaboration. “Jet-hadron correlations measured relative to the second order event plane in Pb-Pb collisions at  $\sqrt{s_{NN}} = 2.76$  TeV”. In: *Phys. Rev. C* 101.6 (2020), p. 064901. DOI: 10.1103/PhysRevC.101.064901. arXiv: 1910.14398 [nucl-ex].
- [181] Sergei A. Voloshin, Arthur M. Poskanzer, and Raimond Snellings. “Collective phenomena in non-central nuclear collisions”. In: *Landolt-Bornstein* 23 (2010), pp. 293–333. DOI: 10.1007/978-3-642-01539-7\_10. arXiv: 0809.2949 [nucl-ex].
- [182] S. Voloshin and Y. Zhang. “Flow study in relativistic nuclear collisions by Fourier expansion of Azimuthal particle distributions”. In: *Z. Phys. C* 70 (1996), pp. 665–672. DOI: 10.1007/s002880050141. arXiv: hep-ph/9407282 [hep-ph].
- [183] ATLAS collaboration. “Measurement of the azimuthal anisotropy for charged particle production in  $\sqrt{s_{NN}} = 2.76$  TeV lead-lead collisions with the ATLAS detector”. In: *Phys. Rev. C* 86 (2012), p. 014907. DOI: 10.1103/PhysRevC.86.014907. arXiv: 1203.3087 [hep-ex].
- [184] E877 collaboration. “Proton and pion production relative to the reaction plane in Au + Au collisions at AGS energies”. In: *Phys. Rev. C* 56 (1997), pp. 3254–3264. DOI: 10.1103/PhysRevC.56.3254. arXiv: nucl-ex/9707002.
- [185] H. Niemi et al. “Event-by-event distributions of azimuthal asymmetries in ultrarelativistic heavy-ion collisions”. In: *Phys. Rev. C* 87 (5 May 2013), p. 054901. DOI: 10.1103/PhysRevC.87.054901. URL: <https://link.aps.org/doi/10.1103/PhysRevC.87.054901>.
- [186] ALICE collaboration. “Higher harmonic non-linear flow modes of charged hadrons in Pb-Pb collisions at  $\sqrt{s_{NN}} = 5.02$  TeV”. In: *JHEP* 05 (2020), p. 085. DOI: 10.1007/JHEP05(2020)085. arXiv: 2002.00633 [nucl-ex].

- [187] Ilya Selyuzhenkov and Sergei Voloshin. “Effects of non-uniform acceptance in anisotropic flow measurement”. In: *Phys. Rev. C* 77 (2008), p. 034904. DOI: 10.1103/PhysRevC.77.034904. arXiv: 0707.4672 [nucl-th].
- [188] A. M. Poskanzer and S. A. Voloshin. “Methods for analyzing anisotropic flow in relativistic nuclear collisions”. In: *Physical Review C* 58.3 (Sept. 1998), pp. 1671–1678. ISSN: 1089-490X. DOI: 10.1103/physrevc.58.1671. URL: <http://dx.doi.org/10.1103/PhysRevC.58.1671>.
- [189] Jean-Yves Ollitrault. “On the measurement of azimuthal anisotropies in nucleus-nucleus collisions”. In: (Nov. 1997). arXiv: nucl-ex/9711003.
- [190] A. Jeffrey and H.H. Dai. *Handbook of Mathematical Formulas and Integrals*. Elsevier Science, 2008. ISBN: 9780123742889.
- [191] ALICE collaboration. “Centrality dependence of the pseudorapidity density distribution for charged particles in Pb-Pb collisions at  $\sqrt{s_{NN}} = 5.02$  TeV”. In: *Phys. Lett. B* 772 (2017), pp. 567–577. DOI: 10.1016/j.physletb.2017.07.017. arXiv: 1612.08966 [nucl-ex].
- [192] ALICE collaboration. “Energy dependence and fluctuations of anisotropic flow in Pb-Pb collisions at  $\sqrt{s_{NN}} = 5.02$  and 2.76 TeV”. In: *JHEP* 07 (2018), p. 103. DOI: 10.1007/JHEP07(2018)103. arXiv: 1804.02944 [nucl-ex].
- [193] ALICE collaboration. “Performance of the ALICE VZERO system”. In: *JINST* 8 (2013), P10016. DOI: 10.1088/1748-0221/8/10/P10016. arXiv: 1306.3130 [nucl-ex].
- [194] Zi-Wei Lin et al. *A Multi-Phase Transport (AMPT) model*. Version v1.26t9b-v2.26t9b. Dec. 2018. URL: <https://myweb.ecu.edu/linz/ampt/>.
- [195] Zi-Wei Lin. “Evolution of transverse flow and effective temperatures in the parton phase from a multi-phase transport model”. In: *Phys. Rev. C* 90.1 (2014), p. 014904. DOI: 10.1103/PhysRevC.90.014904. arXiv: 1403.6321 [nucl-th].
- [196] Constantin Loizides, Jason Kamin, and David d’Enterria. “Improved Monte Carlo Glauber predictions at present and future nuclear colliders”. In: *Phys. Rev. C* 97.5 (2018). [Erratum: *Phys.Rev.C* 99, 019901 (2019)], p. 054910. DOI: 10.1103/PhysRevC.97.054910. arXiv: 1710.07098 [nucl-ex].
- [197] ATLAS collaboration. “Measurement of the centrality and pseudorapidity dependence of the integrated elliptic flow in lead-lead collisions at  $\sqrt{s_{NN}} = 2.76$  TeV with the ATLAS detector”. In: *Eur. Phys. J. C* 74.8 (2014), p. 2982. DOI: 10.1140/epjc/s10052-014-2982-4. arXiv: 1405.3936 [hep-ex].
- [198] CMS collaboration. “Pseudorapidity and transverse momentum dependence of flow harmonics in pPb and PbPb collisions”. In: *Phys. Rev. C* 98.4 (2018), p. 044902. DOI: 10.1103/PhysRevC.98.044902. arXiv: 1710.07864 [nucl-ex].

- [199] PHOBOS collaboration. “Centrality and pseudorapidity dependence of elliptic flow for charged hadrons in Au+Au collisions at  $\sqrt{s_{NN}} = 200$ -GeV”. In: *Phys. Rev. C* 72 (2005), p. 051901. DOI: 10.1103/PhysRevC.72.051901. arXiv: nucl-ex/0407012.
- [200] Particle Data Group collaboration. “Review of Particle Physics”. In: *Chin. Phys. C* 40.10 (2016), p. 100001. DOI: 10.1088/1674-1137/40/10/100001.
- [201] ALICE collaboration. “Centrality dependence of charged jet production in p–Pb collisions at  $\sqrt{s_{NN}} = 5.02$  TeV”. In: *Eur. Phys. J. C* 76.5 (2016), p. 271. DOI: 10.1140/epjc/s10052-016-4107-8. arXiv: 1603.03402 [nucl-ex].
- [202] LHCb collaboration. “Measurement of the Nuclear Modification Factor and Prompt Charged Particle Production in  $p - Pb$  and  $pp$  Collisions at  $\sqrt{s_{NN}} = 5$  TeV”. In: *Phys. Rev. Lett.* 128.14 (2022), p. 142004. DOI: 10.1103/PhysRevLett.128.142004. arXiv: 2108.13115 [hep-ex].
- [203] ALICE collaboration. “Performance of the ALICE Experiment at the CERN LHC”. In: *International J. Mod. Phys. A* 29 (2014), p. 1430044. DOI: 10.1142/S0217751X14300440. arXiv: 1402.4476 [nucl-ex].
- [204] S. van der Meer. “Calibration of the Effective Beam Height in the ISR”. In: (1968). CERN-ISR-PO-68-31.
- [205] “ALICE 2017 luminosity determination for pp collisions at  $\sqrt{s} = 5$  TeV”. In: (Nov. 2018). URL: <https://cds.cern.ch/record/2648933>.
- [206] ALICE collaboration. “Measurement of visible cross sections in proton-lead collisions at  $\sqrt{s_{NN}} = 5.02$  TeV in van der Meer scans with the ALICE detector”. In: *JINST* 9.11 (2014), P11003. DOI: 10.1088/1748-0221/9/11/P11003. arXiv: 1405.1849 [nucl-ex].
- [207] J. Alme et al. “The ALICE TPC, a large 3-dimensional tracking device with fast readout for ultra-high multiplicity events”. In: *Nuclear Instruments and Methods in Physics Research Section A: Accelerators, Spectrometers, Detectors and Associated Equipment* 622.1 (Oct. 2010), pp. 316–367. DOI: 10.1016/j.nima.2010.04.042. URL: <https://doi.org/10.1016%2Fj.nima.2010.04.042>.
- [208] Antonin Maire. “Track reconstruction principle in ALICE for LHC run I and run II. Principes de reconstruction de traces dans ALICE pour les runs I et II du LHC”. General Photo. 2011. URL: <https://cds.cern.ch/record/1984041>.
- [209] R. Fruhwirth. “Application of Kalman filtering to track and vertex fitting”. In: *Nucl. Instrum. Meth. A* 262 (1987), pp. 444–450. DOI: 10.1016/0168-9002(87)90887-4.
- [210] Matteo Cacciari, Gavin P. Salam, and Gregory Soyez. “The Anti-k(t) jet clustering algorithm”. In: *JHEP* 04 (2008), p. 063. DOI: 10.1088/1126-6708/2008/04/063. arXiv: 0802.1189 [hep-ph].
- [211] Stephen D. Ellis and Davison E. Soper. “Successive combination jet algorithm for hadron collisions”. In: *Phys. Rev. D* 48 (1993), pp. 3160–3166. DOI: 10.1103/PhysRevD.48.3160. arXiv: hep-ph/9305266.

- [212] M. Wobisch and T. Wengler. “Hadronization corrections to jet cross-sections in deep inelastic scattering”. In: *Workshop on Monte Carlo Generators for HERA Physics (Plenary Starting Meeting)*. Apr. 1998, pp. 270–279. arXiv: hep-ph/9907280.
- [213] ALICE collaboration. “First measurement of jet mass in Pb–Pb and p–Pb collisions at the LHC”. In: *Phys. Lett. B* 776 (2018), pp. 249–264. DOI: 10.1016/j.physletb.2017.11.044. arXiv: 1702.00804 [nucl-ex].
- [214] Matteo Cacciari and Gavin P. Salam. “Pileup subtraction using jet areas”. In: *Phys. Lett. B* 659 (2008), pp. 119–126. DOI: 10.1016/j.physletb.2007.09.077. arXiv: 0707.1378 [hep-ph].
- [215] Matteo Cacciari, Gavin P. Salam, and Sebastian Sapeta. “On the characterisation of the underlying event”. In: *JHEP* 04 (2010), p. 065. DOI: 10.1007/JHEP04(2010)065. arXiv: 0912.4926 [hep-ph].
- [216] CMS collaboration. “Measurement of the Underlying Event Activity in  $pp$  Collisions at  $\sqrt{s} = 0.9$  and 7 TeV with the Novel Jet-Area/Median Approach”. In: *JHEP* 08 (2012), p. 130. DOI: 10.1007/JHEP08(2012)130. arXiv: 1207.2392 [hep-ex].
- [217] TOTEM collaboration. “The TOTEM experiment at the CERN Large Hadron Collider”. In: *JINST* 3 (2008), S08007. DOI: 10.1088/1748-0221/3/08/S08007.
- [218] “CMS-TOTEM feasibility studies for single diffractive Z, W, Jpsi and central exclusive dijet production in pp collisions at 13 TeV”. In: (2014). CMS-PAS-FSQ-14-001. URL: <https://cds.cern.ch/record/1954682/files/FSQ-14-001-pas.pdf>.
- [219] ALICE collaboration. “Measurement of charged jet production cross sections and nuclear modification in p–Pb collisions at  $\sqrt{s_{NN}} = 5.02$  TeV”. In: *Phys. Lett. B* 749 (2015), pp. 68–81. DOI: 10.1016/j.physletb.2015.07.054. arXiv: 1503.00681 [nucl-ex].
- [220] ALICE collaboration. “Measurements of inclusive jet spectra in pp and central Pb–Pb collisions at  $\sqrt{s_{NN}} = 5.02$  TeV”. In: *Phys. Rev. C* 101.3 (2020), p. 034911. DOI: 10.1103/PhysRevC.101.034911. arXiv: 1909.09718 [nucl-ex].
- [221] G. D’Agostini. “A multidimensional unfolding method based on Bayes’ theorem”. In: *Nucl. Instrum. Meth.* A362.2 (1995), pp. 487–498. ISSN: 0168-9002. DOI: 10.1016/0168-9002(95)00274-X. URL: <http://www.sciencedirect.com/science/article/pii/016890029500274X>.
- [222] Andreas Hocker and Vakhtang Kartvelishvili. “SVD approach to data unfolding”. In: *Nucl. Instrum. Meth.* A372 (1996), pp. 469–481. DOI: 10.1016/0168-9002(95)01478-0. arXiv: hep-ph/9509307 [hep-ph].



- [223] Tim Adye. “Unfolding algorithms and tests using RooUnfold”. In: *Proceedings, PHYSTAT 2011 Workshop on Statistical Issues Related to Discovery Claims in Search Experiments and Unfolding, CERN, Geneva, Switzerland 17-20 January 2011*. CERN. Geneva: CERN, 2011, pp. 313–318. DOI: 10.5170/CERN-2011-006.313. arXiv: 1105.1160 [physics.data-an]. URL: <https://inspirehep.net/record/898599/files/arXiv:1105.1160.pdf>.
- [224] Kerstin Tackmann and Andreas Hoecker. “SVD-based unfolding: implementation and experience”. In: *PHYSTAT 2011*. CERN, 2011, pp. 276–279. DOI: 10.5170/CERN-2011-006.276. arXiv: 1112.2226 [physics.data-an].
- [225] D.C. Lay. *Linear Algebra and Its Applications*. World student series. Pearson / Addison-Wesley, 2006. ISBN: 9780321314857. URL: <https://books.google.fi/books?id=vo92ygAACAAJ>.
- [226] Charles L. Lawson and Richard J. Hanson. *Solving Least Squares Problems*. Society for Industrial and Applied Mathematics, 1995. DOI: 10.1137/1.9781611971217.
- [227] ALICE collaboration. “Measurement of charged jet cross section in pp collisions at  $\sqrt{s} = 5.02$  TeV”. In: (2019). arXiv: 1905.02536 [nucl-ex].
- [228] J.R. Taylor. *Introduction To Error Analysis: The Study of Uncertainties in Physical Measurements*. ASMSU/Spartans.4.Spartans Textbook. University Science Books, 1997. ISBN: 9780935702750.
- [229] ALICE collaboration. *AliPhysics*. Version VO\_ALICE@AliPhysics::vAN-20230315\_O2-1. Mar. 2023. URL: <https://github.com/alishw/AliPhysics>.
- [230] “Measurement of inclusive and leading subjet fragmentation in pp and Pb-Pb collisions at  $\sqrt{s_{NN}} = 5.02$  TeV”. In: (Apr. 2022). arXiv: 2204.10270 [nucl-ex].
- [231] Rene Brun and Fons Rademakers. “ROOT — An object oriented data analysis framework”. In: *Nuclear Instruments and Methods in Physics Research Section A: Accelerators, Spectrometers, Detectors and Associated Equipment* 389.1 (1997). New Computing Techniques in Physics Research V, pp. 81–86. ISSN: 0168-9002. DOI: 10.1016/S0168-9002(97)00048-X. URL: <https://www.sciencedirect.com/science/article/pii/S016890029700048X>.
- [232] *Proceedings of the 1974 CERN School of Computing: Godøysund, Norway 11 - 24 Aug 1974. 3rd CERN School of Computing*. CERN. Geneva: CERN, 1974. DOI: 10.5170/CERN-1974-023. URL: <https://cds.cern.ch/record/186223>.
- [233] ALICE collaboration. “Azimuthal correlations of prompt D mesons with charged particles in pp and p-Pb collisions at  $\sqrt{s_{NN}} = 5.02$  TeV”. In: *Eur. Phys. J. C* 80.10 (2020), p. 979. DOI: 10.1140/epjc/s10052-020-8118-0. arXiv: 1910.14403 [nucl-ex].
- [234] ALICE collaboration. “Measurement of inclusive charged-particle b-jet production in pp and p-Pb collisions at  $\sqrt{s_{NN}} = 5.02$  TeV”. In: *JHEP* 01 (2022), p. 178. DOI: 10.1007/JHEP01(2022)178. arXiv: 2110.06104 [nucl-ex].

- [235] Kari J. Eskola et al. “EPPS16: Nuclear parton distributions with LHC data”. In: *Eur. Phys. J. C* 77.3 (2017), p. 163. DOI: 10.1140/epjc/s10052-017-4725-9. arXiv: 1612.05741 [hep-ph].
- [236] ATLAS collaboration. “Transverse momentum, rapidity, and centrality dependence of inclusive charged-particle production in  $\sqrt{s_{NN}} = 5.02$  TeV  $p + \text{Pb}$  collisions measured by the ATLAS experiment”. In: *Phys. Lett. B* 763 (2016), pp. 313–336. DOI: 10.1016/j.physletb.2016.10.053. arXiv: 1605.06436 [hep-ex].
- [237] Oskari Saarimäki. ALICE preliminary result produced for Quark Matter 2022 conference. Accessed 7th of June 2023. URL: <https://alice-figure.web.cern.ch/node/21921>.
- [238] ALICE collaboration. “Long- and short-range correlations and their event-scale dependence in high-multiplicity pp collisions at  $\sqrt{s} = 13$  TeV”. In: *JHEP* 05 (2021), p. 290. DOI: 10.1007/JHEP05(2021)290. arXiv: 2101.03110 [nucl-ex].